

AD-A078 162

UNITED TECHNOLOGIES RESEARCH CENTER EAST HARTFORD CONN
MODELING OF THE HOT ISOSTATIC PRESSING PROCESS.(U)
SEP 79 B N CASSENTI , K J CHEVERTON

F/6 13/8

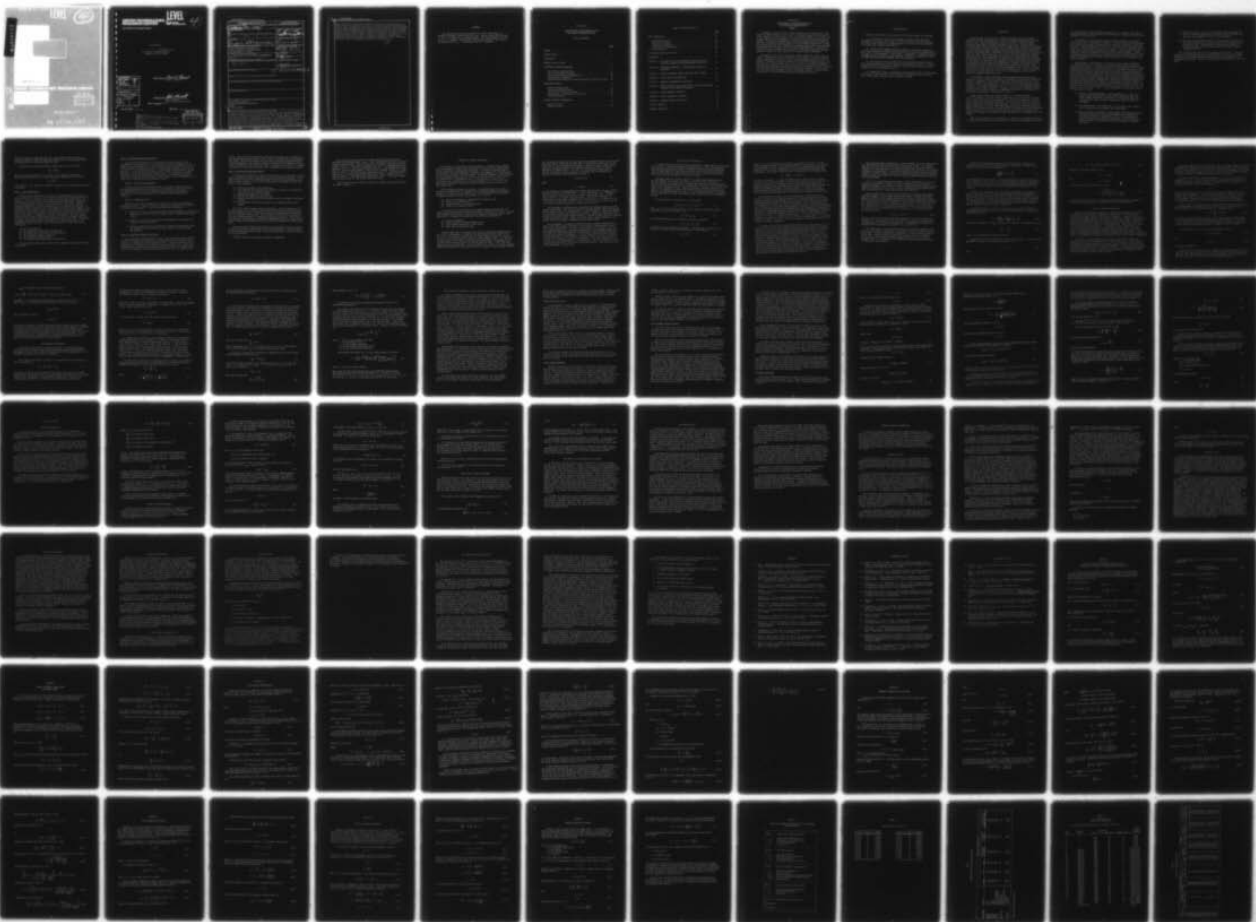
F49620-78-C-0090

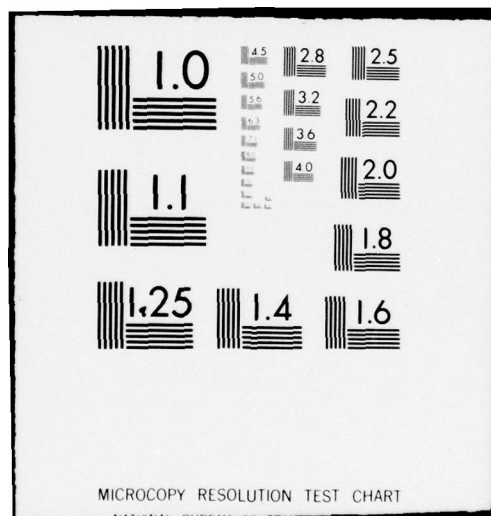
UNCLASSIFIED

AFOSR-TR-79-1236

NL

1 OF 2
ADA
078162





UNITED TECHNOLOGIES RESEARCH CENTER

East Hartford, Connecticut 06108



4

R79-944374-7

Modeling of the
Hot Isostatic Pressing Process
Contract F49620-78-C-0090

Accession For	
NTIS GRA&I	<input checked="" type="checkbox"/>
DDC TAB	<input type="checkbox"/>
Unannounced	<input type="checkbox"/>
Justification	
By _____	
Distribution/	
Availability Codes	
Dist.	Avail and/or special
A	

REPORTED BY Brice N. Cassenti
Brice N. Cassenti

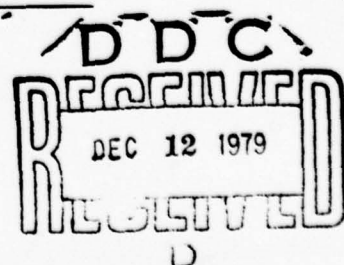
APPROVED BY John S. Kendall
John S. Kendall
Chief, Engineering Analysis

DATE September 1979

NO. OF PAGES _____

COPY NO. _____

AIR FORCE OFFICE OF SCIENTIFIC RESEARCH (AFSC)
NOTICE OF TRANSMITTAL TO DDC
This technical report has been reviewed and is
approved for public release IAW AFR 190-12 (7b).
Distribution is unlimited.
A. D. BLOSE
Technical Information Officer



UNCLASSIFIED


SECURITY CLASSIFICATION OF THIS PAGE (When Data Entered)

REPORT DOCUMENTATION PAGE		READ INSTRUCTIONS BEFORE COMPLETING FORM
1. REPORT NUMBER 18 AFOSR-TR-79-1236	2. GOVT ACCESSION NO.	3. RECIPIENT'S CATALOG NUMBER
4. TITLE (and Subtitle) MODELING OF THE HOT ISOSTATIC PRESSING PROCESS	5. TYPE OF REPORT & PERIOD COVERED 9 INTERIM Rept. 15 Jul 78 - 14 Jul 79	
6. AUTHOR(s) BRICE N. CASSENTI K.J. Cheverton	8. CONTRACT OR GRANT NUMBER(s) 15 F49620-78-C-0090	
9. PERFORMING ORGANIZATION NAME AND ADDRESS UNITED TECHNOLOGIES CORPORATION UNITED TECHNOLOGIES RESEARCH CENTER EAST HARTFORD, CT 06108	10. PROGRAM ELEMENT, PROJECT, TASK AREA & WORK UNIT NUMBERS 16 2307B2 17 B2 61102F	
11. CONTROLLING OFFICE NAME AND ADDRESS AIR FORCE OFFICE OF SCIENTIFIC RESEARCH/NA BLDG 410 BOLLING AIR FORCE BASE, D C 20332	12. REPORT DATE 11 Sep 79	
14. MONITORING AGENCY NAME & ADDRESS (if different from Controlling Office) 12 133 409 252	13. NUMBER OF PAGES 129	
15. SECURITY CLASS. (of this report) UNCLASSIFIED		15a. DECLASSIFICATION/DOWNGRADING SCHEDULE
16. DISTRIBUTION STATEMENT (of this Report) 14 4TRC/R79-944374-7 Approved for public release; distribution unlimited.		
17. DISTRIBUTION STATEMENT (of the abstract entered in Block 20, if different from Report)		
18. SUPPLEMENTARY NOTES		
19. KEY WORDS (Continue on reverse side if necessary and identify by block number) HOT ISOSTATIC PRESSING NONVOLUME PRESERVING PLASTICITY CREEP FINITE ELEMENTS		
20. ABSTRACT (Continue on reverse side if necessary and identify by block number) This report describes the first year of progress of a two year investigation to develop a modeling strategy to predict the final shape of components manufactured by the Hot Isostatic Pressing(HIP) process. When a powder metal is subjected to the high pressures at high temperatures there is a permanent reduction in the macroscopic volume by approximately 30 percent. The volume reduction, which is not included in classical creep and plasticity theories, necessitates the modification of the classical theories. The major part of this report concerns the development of a constitutive model for powder metals. A model for powder		

UNCLASSIFIED

SECURITY CLASSIFICATION OF THIS PAGE(When Data Entered)

metals subjected to an external hydrostatic pressure has been developed and compares well with experimental results. The exact form of the theory depends on the results of mechanical tests presently being performed. The constitutive model is being incorporated into the MARC Analysis Research Corporation (MARC) nonlinear finite element computer program and experiments analyzes using the modified code will be performed to verify the accuracy of the theory. Once the theory has been verified it will be applied to the HIP of a disk where a sensitivity study will determine an efficient modeling strategy. The results and future plans of the program are discussed in detail.



UNCLASSIFIED

FOREWORD

The interim report has been prepared for the Air Force Office of Scientific Research, United States Air Force, Contract F49620-78-C-0090 with Lt. Col. J. D. Morgan as the program monitor. The program manager for UTRC is Mr. A. F. Greiner. The principal investigators during the first year of the program were Dr. K. J. Cheverton and Dr. B. N. Cassenti. ✓

R79-944374-7

Interim Report on the Modeling of the
Hot Isostatic Pressing Process

TABLE OF CONTENTS

	<u>Page</u>
SUMMARY	1
INTERIM RESULTS	2
INTRODUCTION.	3
PROGRAM PLAN AND STATUS	6
CONSTITUTIVE THEORY DEVELOPMENT	12
Yield Surface Considerations.	14
Choice of Hardening Parameters.	16
Large Strain Flow Rule Considerations	21
Time Dependent Deformation.	22
Microstructural Modeling to Develop Macroscopic Constitutive Laws .	26
CODE MODIFICATIONS.	36
General Considerations.	36
Plastic Iteration Procedure	37
Time Effects Iteration Procedure.	40
Code Selection, Installation, and Testing	41
Code Modifications.	42
MATERIAL PROPERTY DETERMINATION	44
Partial HIP Tests	44
Mechanical Tests.	47

TABLE OF CONTENTS (Cont'd)

	<u>Page</u>
MODEL VERIFICATION.	49
Verification Criteria	49
Spherical Inclusions.	50
Cylindrical Inclusions.	51
Yield Surface Considerations.	51
Thermal Effects	52
HIP PROCESS SENSITIVITY STUDIES	54
REFERENCES.	57
APPENDIX A - THE FORM OF THE FINITE ELEMENT STIFFNESS MATRIX FOR PLASTICITY THEORIES WITH NONASSOCIATED FLOWS RULES . . .	60
APPENDIX B - VOLUMETRIC COMPRESSION IN MOHR-COULOMB THEORIES OF PLASTICITY	62
APPENDIX C - PLASTIC VOLUMETRIC STRAIN UNDER PURE SHEAR STRESS. . . .	64
APPENDIX D - YIELD SURFACE CONSIDERATIONS	66
APPENDIX E - HARDENING PARAMETERS AND FLOW RULE	72
APPENDIX F - ELASTIC-PLASTIC SMALL STRAIN MODULI FOR VOLUME PRESERVING PLASTICITY WITH ISOTROPIC HARDENING.	77
APPENDIX G - RIGID SPHERICAL INCLUSIONS	79
APPENDIX H - RIGID CYLINDRICAL INCLUSIONS	81
APPENDIX I - THERMAL CONDUCTIVITY EFFECTS	83
TABLES 1 THROUGH 6.	85
FIGURES 1 THROUGH 35.	91

R79-944374-7

Interim Report on the Modeling of the
Hot Isostatic Pressing Process

SUMMARY

A program to develop a finite element methodology for predicting the final shape of components manufactured by the Hot Isostatic Pressing (HIP) process is being conducted for the Air Force Office of Scientific Research. The major task in the program is the development of a constitutive model for compacting metal powders. The constitutive model must extend the classical plasticity and creep theories to include the large decrease in volume resulting from the HIP process. The constitutive model will be added to an existing finite element code and parameters required by the model will be determined experimentally. The modified code will be used to predict the results of a verification experiment and then applied to predict the final shape of hot isostatic pressed components.

During the first year of the program, several significant results were obtained. Plasticity and creep theories have been extended to include volumetric plastic deformations in order to satisfy the requirements applicable to the HIP process. The MARC code has been selected to do the finite element modeling, and initial tests of MARC indicate that it can be applied to HIP process modeling. Partially dense specimens have been fabricated for the mechanical tests and analytical expressions relating final density to pressure, temperature and time for a HIP cycle are in good agreement with the experimental results. Initial results indicate there is little volume change during compression testing.

INTERIM RESULTS

During the first year of the program, the following results were obtained:

(1) A constitutive theory which includes the large volume reductions, approximately 30 percent, that result from the HIP process, has been developed. The theory extends classical, volume preserving, plasticity and creep theories, to include large volumetric deformations.

(2) Several finite element codes were examined to assess their ability to model the HIP process. The MARC code was selected for use in the program based on the results of the assessment. Initial work to incorporate a constitutive theory for powder metal compaction has been completed. Results of an analytical test of the MARC code large strain capability were also successful.

(3) Partially dense test specimens have been fabricated from MERL 76 and their density measured for various pressures, temperatures and times. Analytical expressions have been developed to predict the partial density and are in good agreement with the experimental results.

(4) Compression, tension and mechanical creep specimens have been fabricated from partially dense material. Initial results indicate that there is little or no volume change occurring during compression testing.

INTRODUCTION

The technology for fabrication of nickel base superalloy turbine engine components by powder metallurgy (PM) methods has advanced rapidly during the past five (5) years. The strong emphasis on PM is the result of advanced engine technology requirements for higher performance alloys which are more difficult to process (cast, forge) and hence, result in higher costs. Advanced PM technology for the production of near net shapes in superalloys offers the two-fold advantage of producing complex engine components from the most advanced alloys without the need for either castability or workability in the alloy and doing so at significantly lower cost than current technology. An Air Force Materials Laboratory's program, described in Ref. 1 has demonstrated the viability of the Hot Isostatic Pressing (HIP) process for the production of a complex turbine disk-shaft to near net shape at significant cost reduction when compared with the current method of production. For nickel-base turbine disks, with integral bolt flanges, over 60 percent of the final component cost is incurred in metal removal operations. Further, nearly 20 percent of the part cost is involved in procurement of raw material, as little as 10 percent of which ends up in the finished machined part. Thus, by improving the buy to fly ratio from 10 to 1 to 5 to 1, it is possible to save nearly 40 percent on component fabrication costs.

A substantial economic advantage for powder metallurgy materials can be achieved by direct hot isostatic pressing of components to near finished dimensions. The HIP of components to near finished dimensions would minimize the cost of machining, and save critical materials. The concept of HIP complex near-net shapes is simple. As is shown schematically in Figs. 1 and 2, a mold having the required configuration is filled with powder. The mold or container, is outgassed, sealed, placed in a HIP facility, raised to a temperature of over 2000 F and subjected to an external gas pressure of approximately 15,000 psi.

During the HIP process the volume occupied by the powder decreases by 30 to 35 percent. The rate of powder compaction occurs as a result of surface tension forces and plastic deformation and is a function of temperature and pressure. Ideally this shrinkage is isotropic, so that the final shape is a uniformly reduced replica of the initial container shape. In practice, the final shape can depart substantially from that ideal shape depending upon the techniques practiced. Because of this distortion and a current absence of systematically derived analytical tools to predict it, the full benefit of the HIP process has not been realized. Rather, HIP containers are fabricated larger than necessary to accommodate this distortion.

Many factors contribute to HIP distortion. Some arise from imperfect execution of steps in the HIP process such as nonuniform filling of the container, thin spots

in container material and incomplete outgassing of the container. The present discussion assumes a perfect fabrication process and is concerned with distortions intrinsic to the HIP process.

To determine the load transferred from the HIP container to the powder a constitutive model of the powder is required. This model should include irreversible compression and shear strength growth as functions of pressure, temperature and time. Volume reductions of 30 percent to 35 percent imply changes in linear dimensions of the container in excess of 10 percent. This in turn implies that the powder and container both experience large strains and displacements. Present research is based on an empirical approach and does not fully address these issues. To adequately model the HIP process a large-strain finite element analysis code possessing experimentally verified constitutive models for the container and the powder is needed.

The objective of this program is to develop a finite element methodology for predicting final size and shape of hot isostatically pressed axisymmetric powder metal structures. A constitutive model for the compaction of metal powders during the HIP process is being constructed and an experimental program is being executed to provide data for and testing of this model. An existing nonlinear finite element code which models both container and powder deformations during the HIP operation is also being modified. This code will be verified by comparing its predictions with the results obtained from both specially designed HIP experiments and from the previous HIP of turbine disks. Constitutive theory development for the container material does not form part of this technical program. Rather the container will be modeled using standard elastic-plastic and creep theories. The material properties for the container material have been developed under separate funding, and are described in Ref. 2. More specifically, the program consists of the following five tasks:

- (1) Constitutive Model Development - The development of a finite strain elastic-plastic-creep model of metal powders compacting under the action of high temperature and pressure. The plasticity and creep theories will be used to predict irreversible volume shrinkage for the powder.
- (2) Code Modifications - The modification of an existing finite element code to incorporate the developed constitutive model.
- (3) Material Property Determination - Metal powder filled glass containers have been subjected to HIP and powder densification determined as a function of pressure, temperature and time. Test specimens are being fabricated from the samples and mechanical tests are presently being performed to determine the stress-strain behavior of partial HIP powders.

- (4) Verification Study - A partial HIP experiment will be designed and executed. The experiment will be simulated using the modified code and the results compared with those of the experiments.
- (5) HIP Process Sensitivities Studies - A disk previously subjected to HIP will be selected and the associated HIP process simulated using the modified code. The sensitivity of predicted shrinkage to the analysis procedure will be determined and an efficient analysis methodology defined.

The following section discusses the program plan and status. The major portion of the first year of work has been devoted to the first three tasks. The results of the investigation in these three areas are presented in the following three sections. The next two sections are a discussion of the future plans.

PROGRAM PLAN AND STATUS

The objective of this program is to develop a finite element methodology for predicting the final size and shape of hot isostatically pressed axisymmetric powder metal structures. There are five main tasks, each of which is discussed in detail below.

Task 1: Constitutive Model Development

In this task a constitutive model which characterizes densification and deformation of metal powders during the HIP process must be developed. The model will be developed through the execution of the following subtasks.

Task 1.1 Yield Surface Determination

A yield surface for compacting metal powders must be developed. Existing yield surface functions have been compared on the basis of their ability to model experimental data. It is expected that a closed smooth yield surface which is quadratic in stress will be selected. More general forms of the yield surface functions are not considered necessary since limited experimental data will be developed and employed in the evaluation of candidate yield surfaces. The yield surface

$$\beta^2 \left(\frac{I_1}{3} \right)^2 + J_2 = \sigma_o^2 / 3$$

is currently preferred. If required, this yield surface will be adjusted to admit unequal yielding in tension and compression by assigning different values to β for tension and compression. The parameters in the yield surface will be evaluated by fitting the function to results obtained from both the partial HIP experiments and the mechanical tests.

If the above equation is selected to represent the yield surface, β and σ_o will be functions of void volume fraction, plastic work, temperature and time.

Task 1.2.1 Deformation dependent hardening

Hardening will be characterized by powder void volume fraction and plastic work performed. Hardening parameters can be characterized as a function of HIP pressure and temperature by measuring the volume reduction of partial HIP test specimens. A large strain, finite element, elastic-plastic analysis of a microstructural model has been performed to assess the usefulness of finite element idealizations of such microstructural compaction process models. Pressure versus volume shrinkage curves have been obtained from the finite element analyses and compared with partial HIP experiments. Yielding of a partially compacted powder in

hydrostatic compression have been assumed to follow experimentally derived pressure versus densification curves. The influence of volume shrinkage on yield stress in shear will be determined from the mechanical tests.

Task 1.2.2 Time dependent hardening

The time dependent hardening of the yield surface will be determined from the mechanical testing of specimens fabricated from partially densified HIP powder. For example, if $\bar{\sigma}$ is a specimen yield strength in uniaxial tension, then for the yield surface assumed in Task 1.1

$$\sigma_o = \bar{\sigma} \sqrt{(1 + \beta^2/3)}$$

The time dependence of σ_o will be determined from the mechanical tests of specimens fabricated from partial HIP samples.

Task 1.3 Flow Rule Development

A HIP process large strain elastic-plastic flow theory must be developed to relate increments of stress and strain. An associated flow rule based on the yield surface developed in Tasks 1.1 and 1.2 has been used. The flow rule relates the Jaumann rate of Cauchy stress to the symmetric part of the velocity gradient.

Since the dominant deformation mode in the HIP process is volume shrinkage, it is possible that rotations and deviatoric strains will be small. To explore this possibility, the flow rule will be reformulated assuming that terms which are quadratic in deviatoric strains and rotations are negligible.

Task 1.4 Creep Effects

A constitutive theory encompassing creep effects will be developed and employed to evaluate the hypothesis that the dominant HIP process deformation mechanism is plastic flow.

Creep deformation has been separated into volumetric and deviatoric components and laws for the components developed. The volumetric creep have been assumed to follow a Norton-Bailey power law model of the form

$$D_{kk}^c = -Ap^m t^n$$

where D_{kk}^c is volumetric creep shrinkage rate. p and t are HIP pressure and time and A , m and n are the usual temperature dependent, power law parameters. A time hardening model will be used to interpolate between known experimental data. The results of the partial HIP tests have been used to assign numerical values to A , m and n . Although the HIP tests are not carried out at uniform temperature and

pressure, volumetric creep shrinkage rate can be computed from the results of fabricating partially dense HIP specimens subjected to the same maximum temperature and pressure for different lengths of times.

The deviatoric creep strains will be modeled using a law of the form

$$\hat{D}_{ij}^c = \frac{3}{2} \frac{\hat{D}^c}{\bar{\sigma}} S_{ij}$$

where the terms are defined in the section on Time Dependent Deformation. To develop material properties for this creep model a uniaxial law of the form

$$\hat{D}^c = B \bar{\sigma}^k t^m$$

will be assumed. The temperature dependent constants can be evaluated from uniaxial creep data.

Task 2: Code Modifications

The HIP process constitutive theory must be incorporated into an existing finite element code. Level H-4 of the MARC nonlinear finite element code is being employed. Level H-4 provides large strain finite element elastic-plastic and creep analysis capability using an updated Lagrangian formulation. Capabilities of the code which can be used in this program are (1) large strain, updated Lagrangian formulation, (2) elastic-plastic and creep constitutive theories, (3) nonlinear boundary conditions, and (4) axisymmetric solid and shell elements. The axisymmetric solid elements will be used to model the powder and the shell elements will be used to model the container. The MARC code is constructed such that the constitutive theory is independent of element formulations. Thus, the element library in MARC will not require modification. The MARC code already possesses the capability to model the gap between the powder and the container. The updated Lagrangian formulation provides the framework for computing all terms in the incremental stiffness matrices. Thus, the only portions of MARC that must be modified are:

- (1) The yield function
- (2) The incremental stress-strain calculations
- (3) The pseudo force load vector for creep analyses
- (4) The incremental strain calculations
- (5) The plasticity hardening rules
- (6) The routines which print stresses and strains.

The code modifications can be verified by the analysis of simple one element test problems.

Task 3: Material Property Determination

The constitutive parameters will be evaluated through a series of HIP experiments and mechanical tests. Specifically the shape and expansion of the powder yield surface and the creep law parameters will be determined as functions of HIP pressure, temperature and time. The experimental program consists of two subtasks. In the first subtask samples of metal powder are subjected to partial HIP cycles. In the second subtask mechanical tests are performed on specimens fabricated from partially dense HIP powder samples. The experimental program uses only one type and initial density of metal powder: that corresponding to the powder used in the HIP disk to be modeled in Task 5.

Task 3.1 Partial HIP Experiments

A matrix of partial HIP experiments must be executed to determine plastic and creep volumetric strains as functions of HIP pressure, temperature and time. The experimental samples were cylindrical powder filled glass containers. Several HIP cycles were considered and the resulting powder densification measured.

Task 3.2 Mechanical Tests

Mechanical tests must be conducted to determine the plasticity parameters identified in Task 1. Partially dense HIP samples were removed from the furnace and machined into specimens. Three types of tests can be performed:

- (1) Compression tests are being performed at the HIP temperature to identify one point on the yield surface and to examine plastic, hardening and elastic response.
- (2) Tension tests are being performed at HIP temperature to determine the symmetry of the yield surface.
- (3) Uniaxial creep tests will be performed at selected fixed uniaxial loads and temperatures to determine the creep response of partially dense HIP specimens.

Task 4: Constitutive Theory Verification

The constitutive model developed in Task 1 must be experimentally validated. Tests will be designed and conducted to investigate regions of the theory not explored by the mechanical tests performed in Task 3. This investigation will be accomplished by designing and considering several candidate tests. Two of these candidate tests include spherical and cylindrical inclusions in a powder metal. Each of the candidate tests will be modeled numerically using the modified code of

Task 2. The results of the numerical modeling will be examined to determine the most appropriate candidate test or tests. Several specimens will be manufactured and tested. Only glass containers are used since they have negligible strength at HIP temperatures. The time each specimen is maintained at temperature will be varied to demonstrate the effects of creep. The results of the tests, for example, the density as a function of position, will be compared to the numerical results.

Task 5: HIP Process Sensitivity Study

A study must be conducted to assess the sensitivity of the HIP process constitutive and numerical models to parameter values and numerical techniques. A HIP geometry will be selected for which documented initial and final dimensions exist. Finite element analyses of the selected geometry will be performed to assess the affects of the following:

- (1) Inclusion of powder creep deformations
- (2) The assumption that rotations and deviatoric strains in the powder are small relative to volumetric strains
- (3) Temperature gradients in the powder
- (4) Gaps between powder and container walls
- (5) Pressure temperature and time increments sizes and increment convergence criteria
- (6) The frequency with which coordinates of the deforming geometry are updated.

Two finite element breakups should be generated. The first breakup will be relatively simple but sufficient to model overall container and powder response. Local deformations caused by container corners and container-powder interactions can not be included in this model. Only variables (2) and (4) of the previous list are strongly dependent on container and powder interactions. The effects of the remaining variables will be investigated independently using the simple finite element breakup and recommendations for the efficient modeling of the HIP process made.

The second finite element breakup should be more detailed and will be used to investigate interactions between the powder and the container. The contributions of large rotations and shear strains to final predicted shape of the HIP container will be investigated.

In Table 1 each of the tasks and subtasks are summarized.

The first year of work under this contract has been devoted to Task 1: Constitutive Model Development; Task 2: Code Modifications and Task 3: Material Properties Determination. More specifically the following Tasks have been completed: Task 1.1: Yield Surface Determination, Task 1.2: Deformation and Time Hardening, Task 1.3: Flow Rule Development, Task 2.1: Code Familiarization and Task 3.1: Partial HIP Experiments. Work has been initiated on Task 1.4: Creep Effects, Task 2.2: Numerical Strategy Definition, Task 2.3: Code Modifications, and Task 3.2.1: Elevated Temperature Compression Testing. Work has not yet begun on Task 2.4: Code Modification Verification, Task 4: Constitutive Theory Verification and Task 5: HIP Process Sensitivity Study.

The following sections describe in detail the results and plans for each of the Tasks 1 through 5.

CONSTITUTIVE THEORY DEVELOPMENT

Hot isostatic pressing (HIP) of metal powders is a complex process wherein the loose aggregate of metal powder particles is compacted into a coherent mass by the application of temperature and pressure. To achieve a specific shape a glass or metal container resembling the shape of the component to be manufactured is fabricated and filled with metal powder. The filled container is first vibrated to increase powder bulk density and is then evacuated and sealed. After heating in a preheat oven at approximately 2000 F, the container is transferred to a HIP furnace and is subjected to a pressure-temperature cycle. For nickel base superalloys temperature and pressure typically range up to 2200 F and 15,000 psi, respectively.

The HIP process performs two functions: (1) densification of the loose powder metal aggregate and (2) endowment of the densified powder with mechanical strength. The process by which this occurs can be described microstructurally as passing through the several stages (Refs. 3, 4, and 5):

- (1) Particle rearrangement, fragmentation and plastic flow
- (2) Formation of isolated pores
- (3) Sphericalization of the isolated pores
- (4) Closure of the spherical pores

Driving forces for these stages are the applied external HIP pressure and particle surface free energy of which the former is typically much larger. Although the mechanisms which are active during these stages of the process are not fully understood, it is generally accepted that the principle mechanisms are

- (1) Plastic deformation
- (2) Volume diffusion or Nabarro-Herring creep
- (3) Grain boundary diffusion or Coble creep
- (4) Power law or dislocation creep

Recently Ashby (Ref. 6) developed the concept of deformation mechanism maps as a tool for delineating (1) regions in stress-temperature space where one or more of these mechanisms dominates and (2) regions where more than one mechanism is active. These maps have been applied by several authors (Refs. 3, 4, and 7) to the HIP process in an attempt to identify active mechanisms. The geometric model on which these studies are based is a hollow spherical shell of inner and outer radius R_1 and R_2 , respectively. The inner radius, R_1 , is that of a typical isolated spherical pore and R_2 is such that the density of the metal shell material averaged

over the shell and pore equals the macroscopically measured density of the partially densified powder. Wilkinson and Ashby (Ref. 3) using Torre's model (Ref. 8) and Green (Ref. 9) have considered the shrinkage of perfectly plastic hollow spheres subject to an external pressure as a means of gauging the effect of plastic deformation on densification. If p and σ_y are the applied external pressure and the at temperature yield strength of the powder, then the residual void fraction after plastic deformation will be equal to

$$v = \exp(-3p/2\sigma_y) \quad (1)$$

where

$$v = \rho_v / \rho_{\text{solid}} \quad (2)$$

ρ_v is the density of the aggregate after plastic densification, and ρ_{solid} is the density of the fully compacted powder. At high temperatures (e.g., 2000 deg F) and 15,000 psi HIP pressure can be up to three times greater than σ_y in which case v , from Eq. (1) is less than one percent. Although this analysis is appropriate for only powder aggregates with isolated pores (i.e., powders in the final state of compaction) it does indicate the possibility that much of the compaction process can be characterized using plasticity theory.

Two approaches to modeling powder deformation and strength growth in the HIP process are possible. The first is based on continuum mechanics principles wherein microstructural effects are averaged over the powder aggregate. The second approach is to consider microstructural processes explicitly. Since the objective of this program is to predict overall powder response in the HIP process, the latter approach is not sufficient by itself. Rather, it may be used to aid development of continuum constitutive models by supplementing experimental work.

The development of continuum constitutive models requires consideration of large strain effects since the initial void fraction is approximately 30 percent. This in turn implies that a 30 percent volume reduction is necessary to obtain full powder densification. Both time independent and time dependent models must be considered, though based upon the above equations, time independent plasticity effects can be expected to dominate. A finite strain plasticity theory requires: (1) specification of a yield surface to delineate regions of elastic and plastic response, (2) a hardening rule for the expansion of this yield surface and (3) a flow rule for relating stress and strain increments. This flow rule must be formulated using large strain, stress and strain rate measures. Time effects require the specification of a creep law.

Yield Surface Considerations

In this section yield surface concepts pertinent to powder metals are discussed. Since, a priori, powder metals might be thought similar to soil like materials, soil mechanics yield surface theory is reviewed and the shortcomings identified. Next the requirements for compacting powder metal yield surfaces are discussed and previously published yield surfaces are reviewed. Last, the yield surface forms to be used are presented, and discussed in detail.

The metal powder is initially packed as a cohesionless granular material. The HIP container is evacuated, brought to a moderately high temperature and maintained at this temperature. Although some sintering by surface diffusion may occur at this point, the rates will generally be low, due to the initially small contact area between particles. Since the material is granular with no fluid phase, it is reasonable to expect that the Mohr-Coulomb type yield surfaces from soil and rock mechanics might be relevant to the incipient deformation. Figure 3 shows a cross section of the linear Mohr-Coulomb yield surface for a cohesionless material.

The yield surface is defined by the yield function

$$f(\sigma_{ij}) = \beta I_1 + \sqrt{J_2} - \sigma_o/\sqrt{3} = 0 \quad (3)$$

where I_1 is the first stress invariant or three times the mean Cauchy stress $\sigma_{kk}/3$ and σ_o is the yield stress. Also

$$J_2 = 1/2 S_{ij} S_{ij} \quad (4)$$

is the second invariant of the deviatoric stress S_{ij} defined by

$$S_{ij} = \sigma_{ij} - I_1 \delta_{ij}/3 \quad (5)$$

δ_{ij} being the usual Kronecker delta symbol. Note that when β is zero Eq. (3) reduces to the usual yield surface definition of metal plasticity

$$J_2 = \sigma_o^2/3 \quad (6)$$

In Eq. (3), it is assumed that the material is isotropic and flows at a Mises equivalent shear stress which is linearly dependent on mean stress. The linearity of this dependence is not a necessary feature of such pressure-sensitive yield conditions, but is rather a mathematical convenience generally consistent with observations. More general relations, such as the parabolic Mohr-Coulomb model,

$$J_2 + \beta \frac{\sigma_0}{\sqrt{3}} I_1 - \sigma_0^2 / \sqrt{3} = 0 \quad (7)$$

can also be considered. For Mohr-Coulomb materials, admissible stress states are those on or within the region to the left of the yield surface curve (see Fig. 3). Within this region, the frictional forces between particles are sufficient to suppress large macroscopic deformations due to particle rearrangement; further, the macroscopic response is taken to be linear elastic. Of course, the elastic moduli governing deformation within this region are not those of the material matrix, but are suitably reduced due to the presence of interparticle void space.

At some fixed mean stress, as J_2 is increased to its yield value, the frictional forces can no longer prevent particles from sliding over each other. Permanent macroscopic shape changes then occur as particles ride over one another and establish new contacts with adjacent particles. For soil like materials it is experimentally observed that this new configuration is not as densely packed as the initial state, and some volume increase is observed. This particle rearrangement occurs rapidly enough that the deformation can be idealized as instantaneous plasticity. An important feature of plastic deformation accommodated by frictional processes is illustrated schematically in Fig. 3. That is, the plastic strain vector, E^p in Fig. 3, is generally nonassociative: it is not expressible as the gradient with respect to stress, N in Fig. 3, of the yield function. A consequence of such non-normal flow rules is that the incremental stress-strain matrix is non-symmetric as shown in Appendix A.

In summary, the effect of standard Mohr-Coulomb type yield surface is to (1) close the yield surface in principal stress space along the positive hydrostatic direction and (2) to predict volumetric plastic expansion as shown in Appendix B. While this is clearly a proper material limitation to impose for soils, it is a limitation which is not encountered during the HIP process. This is because material points experience a monotonic increase in hydrostatic pressure, corresponding to leftward movement along the I_1 axis in Fig. 3, followed by a period of constant pressure, and then depressurization. For such a load history, Mohr-Coulomb theory predicts no inelastic volume change. But, in fact, inelastic behavior is macroscopically observed as pressure is increased. A new mechanism of plastic deformation takes place due to dislocation motion within the particles. That dislocation motion should occur within the particles is not surprising, since the micro-stress distribution within particles is highly nonuniform due to uneven traction distributions at interparticle contacts.

Once particles begin to deform due to contact loading, it can be expected that many additional deformation mechanisms may be operative as well. For example, some particles may break free of the restraining frictional forces and reorient themselves, but when averaged over volumes containing many particles, the macroscopic deformation corresponding to a macroscopic hydrostatic pressure would be a uniform volumetric decrease. Indeed, any deviatoric deformation arising from a spherically symmetric stress state would be in conflict with the presumed macroscopic isotropy of the metal powder.

Thus, to use a Mohr-Coulomb type theory to model the HIP process, the yield surface must be modified to admit (1) yield in compression and (2) permanent volumetric shrinkage. This can be achieved by closing the yield surface along the negative hydrostatic axis as in Fig. 4. Such an approach has been adopted by Suh (Ref. 10) starting from a linear Mohr-Coulomb yield condition.

Another approach is to postulate the definition of a yield surface based on heuristic arguments. Since powder particle orientation is random, the powder aggregate should initially respond isotropically. Thus the yield function must also be an isotropic function and depend on only the stress through its invariants. Also, yielding must occur under hydrostatic pressure and that the yield function must approach that of a metal as densification progresses. Since invariant I_1 is a linear multiple of the hydrostatic component of stress, and yield surfaces for metals are usually defined in terms of invariant J_2 , a convenient form for the yield surface is

$$f = f(I_1, J_2, h_\alpha) = 0 \quad (8)$$

Further, since all first and second order invariants of stress are expressible in terms of I_1 , and J_2 and the third invariants of σ_{ij} and s_{ij} have no physical interpretation, Eq. (8) appears quite general. The parameters h_α depend on the deformations, and represent, for example, β and σ_0 in Eq. (3).

The yield surface in stress space should also be initially closed and then tend to an open ended cylinder about the hydrostatic axis as the powder compacts and sinters. Yielding in hydrostatic compression is clearly needed to model the HIP process. Further yielding in hydrostatic tension is also to be expected since a partial HIP specimen resembles a metal with voids and, as shown by Needleman (Ref. 11), hydrostatic yield dependence permits macroscopic modeling of void growth and coalescence.

Assume that a HIP powder metal has the same response in tension as in compression, and that the yield surface has no sharp corners. A simple yield function satisfying the above assumptions is

$$\beta^2 \left(\frac{I_1}{3} \right)^2 + J_2 = \frac{\sigma_0^2}{3} \quad (9)$$

A yield function of the form of Eq. (9) has previously been proposed by Green in Ref. 9, Shima and Oyani in Ref. 12, and Kuhn and Downey in Ref. 13. Equation (9) is an ellipse in $I_1, \sqrt{J_2}$ space (Fig. 5), with deformation dependent parameters β and σ_0 . The yield surface is plotted in principal stress space with σ_3 zero in Fig. 6.

Note that as β approaches zero, the Mises yield condition is recovered. In Fig. 3, yield surface Eq. (9) has been plotted with the linear and parabolic Mohr-Coulomb yield surfaces for the case of β equal to one. It should be noted that Eq. (9) predicts a closed yield surface which is smooth where it intersects the hydrostatic axis. Also assuming small strains and an associated flow rule, Eq. (9) implies that, unlike Mohr-Coulomb theories pure shear stress induces no plastic volumetric change, as shown in Appendix C.

A large strain theory of plasticity based on Eq. (9) can be developed by decomposing the symmetric part of the velocity gradient tensor, D_{ij} into elastic and plastic parts, or

$$D_{ij} = \frac{1}{2} \left(\frac{\partial v_i}{\partial x_j} + \frac{\partial v_j}{\partial x_i} \right) = D_{ij}^e + D_{ij}^p \quad (10)$$

The plastic deformation rate D_{ij}^p is assumed to be given by an associated flow rule

$$D_{ij}^p = \dot{\lambda} \frac{\partial f}{\partial \sigma_{ij}} \quad (11)$$

where $\dot{\lambda}$ is a scalar function greater than zero.

Equations (8) and (11) can be used to solve for the scalar $\dot{\lambda}$. Assume that the parameters h_α depend on the deformation measures η_α , or

$$h_\alpha = h_\alpha(\eta_\alpha) \quad (12)$$

then

$$\dot{\lambda} = -[\dot{\sigma}_{ij} \partial f / \partial \sigma_{ij}] / [k_{\beta} (\partial f / \partial h_{\alpha}) (\partial h_{\alpha} / \partial \eta_{\beta})] \quad (13)$$

where the η_{β} have been chosen so that

$$\dot{\eta}_{\beta} = \dot{\lambda} k_{\beta} (\sigma_{ij}) \quad (14)$$

and

$$(\dot{}) = \partial() / \partial t$$

For the particular yield function in Eq. (9)

$$\dot{\lambda} = - \frac{\frac{2}{9} \beta^2 I_1 \dot{I}_1 + \dot{J}_2}{\frac{2}{9} \beta I_1^2 \frac{\partial \beta}{\partial \eta_{\alpha}} k_{\alpha} - \frac{2}{3} \sigma_0 \frac{\partial \sigma_0}{\partial \eta_{\alpha}} k_{\alpha}} \quad (15)$$

A complete discussion of the yield surface considerations appears in Appendix D. The choice of the parameters η_{α} is described in the following section.

Choice of Hardening Parameters

In this section, strain hardening of a compacting metal powder is discussed and parameters to characterize hardening are identified. This is necessary to complete the specification of the plastic deformation. Initially, the yield surface of the powder aggregate will be small. During the compaction and sintering process yield strength will grow and the yield surface will expand. Compaction alone will cause growth of the yield surface along only the I_1 axis (Fig. 5) with a theoretical limit corresponding to full densification. Yield stress in shear will be less affected by compaction. Additionally, yield strength will grow in all directions of stress space with increased sintering time. Thus, there exists a time dependent hardening phenomenon unique to powder metallurgy. Since plastic deformations are assumed to occur instantaneously, time enters the plasticity theory as a parameter defining yield surface size at the time of plastic deformation.

The process of strain-hardening in triaxial pressure will primarily be a geometric effect on the microscopic scale. There could also be a contribution to the apparent macroscopic hardening due to real strain hardening of the particles as they experience large plastic shearing deformations. Such an effect could raise the effective yield strength $\bar{\sigma}$ of the metal particles. The separate contributions of matrix hardening and void reduction can be determined from systematic experiments using different initial volume fractions.

Initially, powder particles contact each other at isolated points. As pressure is applied, the contact areas and the powder stiffness increase. The macroscopic result is strain hardening of the powder due to macroscopic shrinkage. In the limit the powder is completely compacted and the response to further pressure increments is elastic dilation; the plastic bulk modulus has become infinite.

An obvious choice for a deformation measure, η_1 , is the void volume fraction defined in Eq. (2). The void volume fraction is a measure of the macroscopic shrinkage and should reflect an increase in stiffness due to an increase in contact area between the individual particles, or

$$\eta_1 = v \quad (16a)$$

The void volume fraction does not represent any permanent changes that occur during plastic deformation. If as in classical plasticity theory the effective plastic strain defined in Eq. (D.13) is used this would not represent all of the permanent deformations since volume changes would not be represented. A third deformation measure, the plastic volume change would then be required.

Rather than use the permanent volume change and the effective plastic strain as two independent deformation measures, a single measure, the plastic work, would be sufficient to represent both effects. Therefore choose

$$\eta_2 = W^P = \int_0^t \sigma_{ij} D_{ij}^P dt \quad (16b)$$

In classical volume preserving plasticity theory using either the plastic work or the effective plastic strain produces exactly the same result. The plastic work, or equivalently the inelastic energy dissipation has been used previously to describe nonlinear material response, for example, in Refs. 14 and 15.

The quantities k_α , Eq. (14) can now be determined from η_α as

$$k_1 \approx \frac{2}{3} (1-v) \sigma_0^2 \quad (17a)$$

and

$$k_2 = \frac{2}{3} \sigma_0^2 \quad (17b)$$

as shown in Appendix E.

Parks, Ref. 16, has pointed out an interesting connection between the plastic work, the void volume fraction, and the effective plastic strain in the solid material. Note that the rate of work done macroscopically on the entire specimen must equal the rate of work done on the solid powder particles, or

$$\int_V \dot{W}^P dv = \int_V s_{ij}^{solid} d_{ij}^{p,solid} dv_{solid} \quad (18)$$

where $d_{ij} = D_{ij} - 1/3 D_{kk} \sigma_{ij}$

Equation (18) can be equivalently written as

$$\dot{W}^P = (1-v) \bar{\sigma}_{solid}^P \bar{\epsilon}_{solid}^P \quad (19)$$

where

$\bar{\sigma}_{solid}$ is the equivalent tensile stress in the solid material, and
 $\bar{\epsilon}_{solid}^P$ is the equivalent tensile strain in the solid material.

If the stress-strain relationship for the solid material (i.e., $\bar{\sigma}_{solid}$ vs. $\bar{\epsilon}_{solid}^P$) is known then the plastic work can be determined as a function of void volume fraction and equivalent plastic strain in the solid material.

It is now possible to describe the symmetric part of the velocity gradient tensor in terms of the stress rate, for small strains, using Hooke's Law for the elastic response and Eq. (11) for the plastic response as

$$\dot{\sigma}_{kl} = C_{ijkl}^{e-p} D_{ij} \quad (20)$$

where

$$C_{ijkl}^{e-p} = \frac{1}{E} \left[(1+v) \delta_{ik} \delta_{jl} - v \delta_{ij} \delta_{kl} \right] - \frac{1}{H} \left[\frac{2}{9} \beta^2 \sigma_{kk} \delta_{ij} + S_{ij} \right] \left[\frac{2}{9} \beta^2 \delta_{kl} + S_{kl} \right] \quad (21)$$

$$H = \frac{2}{9} \beta I_1^2 \left[\frac{2}{3} (1-v) \beta^2 I_1 \frac{\partial \beta}{\partial v} + \frac{2}{3} \sigma_o^2 \frac{\partial \beta}{\partial W^P} \right] - \frac{2}{3} \sigma_o \left[\frac{2}{3} (1-v) \beta^2 I_1 \frac{\partial \sigma_o}{\partial v} + \frac{2}{3} \sigma_o^2 \frac{\partial \sigma_o}{\partial W^P} \right] \quad (22)$$

E = Young's modulus

v = Poisson's ratio

and

$$D_{ij} = C_{ijkl}^{e-p} \dot{\sigma}_{kl}$$

Large Strain Flow Rule Considerations

The macroscopic deformations during HIP can be large with volume reductions approaching 30 percent. Consequently, a rigorous finite deformation formulation of the process is required. It should be noted that a finite deformation analysis need be employed only if a material point undergoes a large volume change or if a material line element undergoes a large orientation change. In the present case, it may be expected that only the former effect is sufficiently large to mandate the finite deformation analysis. However, the possibility of large rotations will be included in the following discussion.

Two approaches to problems involving finite deformation are: (1) refer all continuum variables to a fixed initial reference configuration, or (2) continuously update the reference configuration to the current (most recent) configuration. The finite element implementation of these methods for large plastic deformation has been discussed by Hibbitt, Marcal and Rice (Ref. 17) and McMeeking and Rice (Ref. 18). The updated Lagrangian formulation of McMeeking and Rice, though fully equivalent to that of Hibbitt et al., is superior. The updated Lagrangian formulation is computationally simpler, there are fewer terms in the stiffness matrix computation and the yield condition is simpler to express.

Following McMeeking and Rice, note that, with the current deformed state as the reference configuration, all stress measures coincide: $\sigma_{ij} = S_{ij} = \tau_{ij} = t_{ij}$ where the stresses are, respectively, Cauchy (true), second Piola-Kirchhoff, Kirchhoff, and first Piola-Kirchhoff stress measures. However, the rates associated with these stress measures do not coincide. A stress rate which is useful for expressing large deformation constitutive laws is the Jaumann, or co-rotational rate (Ref. 19). The Jaumann rate of Cauchy stress is

$$\overset{\nabla}{\sigma}_{ij} = \dot{\sigma}_{ij} - \sigma_{ip} \Omega_{pj} + \Omega_{ip} \sigma_{pj} \quad (23)$$

where $\dot{\sigma}_{ij}$ is the material time rate of Cauchy stress σ_{ij} and

$$\Omega_{ij} = \frac{1}{2} (\partial v_i / \partial x_j - \partial v_j / \partial x_i)$$

The constitutive law of interest is of the form

$$\overset{\nabla}{\sigma}_{ij} = L_{ijkl} D_{kl} \quad (24)$$

where L denotes the rate moduli, D_{ij} is the symmetric part of the velocity gradient tensor.

L_{ijkl} is developed in Ref. 20 for large strains as

$$L_{ijkl} = L_{ijkl}^{e-p} - \frac{1}{2} \left[\delta_{ik} \sigma_{jl} + \delta_{jk} \sigma_{il} + \delta_{il} \sigma_{jk} + \delta_{jl} \sigma_{ik} \right] + \sigma_{ij} \delta_{kl} \quad (25)$$

and L_{ijkl}^{e-p} is the small strain elastic-plastic stiffness in Eq. (20). The tensor L_{ijkl} is not symmetric due to the presence of the last term, or

$$L_{ijkl} \neq L_{klij}$$

For a hydrostatic pressure

$$\sigma_{ij} = P \delta_{ij} \quad (26)$$

the tensor is symmetric and since this should be the primary part of the loading during the HIP process, the last term should produce a nearly symmetric stiffness. It therefore has been decided to separate the last term into symmetric and unsymmetric parts, and add the symmetric part to the stiffness matrix and transfer the unsymmetric part of the loading side of the governing equations. In the resulting analysis, the unsymmetric part resulting from one load step will be applied as an incremental load on the next load step.

Time Dependent Deformation

In the HIP process two time effects are present: the strength growth of the metal powder as bonds between contacting particles grow and time dependent deformation as voids shrink. Powder strength growth has been modeled as the time dependent expansion of the plastic yield surface.

In the small strain theory of metals it is assumed that the total strain ϵ_{ij} can be represented as

$$\epsilon_{ij} = \epsilon_{ij}^e + \epsilon_{ij}^p + \epsilon_{ij}^c \quad (27)$$

where ϵ_{ij}^e , ϵ_{ij}^p and ϵ_{ij}^c are the elastic, plastic and creep parts of the strain, respectively. The elastic strain is time independent and recoverable, the plastic strain is time independent and irrecoverable, and the creep strain is time dependent and irrecoverable. Typically, creep deformations in metals are

significant when absolute temperatures are greater than one half of metal melting point. Also, creep deformations are volume preserving. Creep laws for constant uniaxial stress are usually expressed as

$$\dot{\epsilon}^c = f(\sigma, t, T) \quad (28)$$

where $\dot{\epsilon}^c = d\epsilon^c/dt$ is the rate of uniaxial creep strain and σ , t and T are uniaxial stress, time and temperature, respectively. An example of Eq. (28) is the Norton - Bailey power law (Ref. 21):

$$\dot{\epsilon}^c = A(T)\sigma^m t^k \quad (29)$$

If the creep rate is steady the creep strains can be written as

$$\epsilon^c = B(T)\sigma^n \quad (30)$$

where A , B , K , m and n are determined by fitting the function to experimental creep strain data. Experimental data is usually in the form of creep strain as a function of time for a fixed stress and temperature.

To compute creep strains for a time dependent stress state interpolation between experimental data is necessary. The simplest interpolation scheme is time hardening which is illustrated graphically in Fig. 7. Assume that Eq. (29) holds for constant uniaxial stress. Then from Fig. 7, creep strain rate equals $A\sigma_1^m t^n$ for a stress σ_1 and time between t_0 and t_1 . At time t_1 , time hardening assumes that $\dot{\epsilon}^c$ instantaneously becomes $A\sigma_2^m t^n$, and is thereafter given by $A\sigma_2^m t^n$. Thus a time hardening assumption implies that creep strain rate depends only on present stress and so is insensitive to previous stress history. Time hardening, while not borne out by experiments, does give a lower bound estimate to creep strain and is simple to implement in a computer code.

To obtain creep strain rates for multiaxial stress states it is customary to generalize uniaxial creep laws in a manner analogous to the derivation of the Prandtl-Reuss equations of classical plasticity (Ref. 21) giving

$$\dot{\epsilon}_{ij}^c = \frac{3}{2} \frac{\dot{\epsilon}^c}{\bar{\sigma}} S_{ij} \quad (31)$$

where

$$\dot{\epsilon}^c = \sqrt{\frac{2}{3} \dot{\epsilon}_{ij}^c \dot{\epsilon}_{ij}^c}, \quad \bar{\sigma} = \sqrt{\frac{3}{2} S_{ij} S_{ij}} \quad (32)$$

are the equivalent creep strain rate and equivalent stress, respectively, and are assumed related according to

$$\dot{\bar{\epsilon}}^c = f(\bar{\sigma}, t, T) \quad (33)$$

In the HIP process temperatures are between 80 and 90 percent of the powder metal melting point. Therefore, creep deformation is possible as voids in the compacting powder shrink. However, it is difficult to observe such creep in a HIP test because of the time necessary to pressurize and depressurize the HIP facility. Standard HIP practice utilizes a monotonic increase in pressure and temperature over a period which may be as long as an hour, followed by a two or three hour hold at pressure and temperature. In the partial HIP experiments specimens differing only by the time they are maintained at temperature and pressure have been fabricated. Time dependent volumetric shrinkage can be computed by comparing the amount of densification. Thus a volumetric creep strain law can be experimentally derived. A possible expression for this law is

$$D_{kk}^c = -A P^m t^k \quad (34)$$

while for a steady creep

$$D_{kk}^c = B P^n$$

which is analogous to Eq. (29). Here D_{kk}^c is the trace of the creep component of the velocity gradient D_{ij} , p is the HIP pressure and t , time.

To derive a creep law for the deviatoric component \hat{D}_{ij}^c of the creep strain velocity gradient a law of the form

$$\hat{D}_{ij}^c = \Lambda \partial f / \partial S_{ij} \quad (35)$$

is postulated where, parallel to the small strain theory, f is the yield function for the compacting metal powder. If the yield function of Eq. (29) is used, Eq. (35) reduces to

$$\hat{D}_{ij}^c = \Lambda S_{ij}$$

This may be rewritten as

$$D_{ij}^c = \frac{3}{2} \frac{\hat{D}^c}{\bar{\sigma}} S_{ij} \quad (36)$$

where analogous to Eq. (31)

$$\bar{\hat{D}}^c = \frac{\sqrt{2}}{3} \hat{D}_{ij}^c \hat{D}_{ij}^c \quad , \quad \bar{\sigma} = \frac{\sqrt{3}}{2} S_{ij} S_{ij} \quad (37)$$

To complete this creep law a relationship between $\bar{\hat{D}}^c$ and $\bar{\sigma}$ must be determined experimentally.

The dominant creep mechanism can be determined by examining creep deformation maps presented by Ashby in Ref. 6. The map for nickel is the most appropriate map since nickel based superalloys are being modeled. The creep deformation map, from Ref. 6, for nickel is reproduced in Fig. 8 with experimental points outlining the partial HIP experiments with MERL 76. The major creep mechanism for HIP operating conditions appears to be dislocation creep if it is assumed that the pressure is approximately equal to the tensile stress. Steady state dislocation creep is generally described by Eq. (30) with the temperature dependent function represented by an activation energy. Equation (30) can be rewritten as

$$\dot{\epsilon}_{\text{creep}} = \frac{1}{t_0} e^{\frac{-T_0}{T}} \left(\frac{\sigma}{\sigma_0} \right)^N \quad (38)$$

where $\dot{\epsilon}_{\text{creep}}$ is the uniaxial creep rate,
 σ is the uniaxial stress
 T is the absolute temperature
 σ_0 can be assigned an arbitrary value
 t_0 , T_0 and N are material constants

From Wilkinson and Ashby, Ref. 22, the relative density is given by

$$\dot{\rho} = k \left[\frac{1}{t_0} e^{\frac{-T_0}{T}} \right] \left[\frac{k}{N} \left(\frac{P}{\sigma_0} \right) \right]^N \left\{ \frac{\rho(1-\rho)}{[1-(1-\rho)^{1/N}]^N} \right\} \quad (39)$$

where $\rho = 1-v$ is the relative density.

and k is $\frac{3}{2}$ for final densification and 2 for intermediate densification. The relative density after plastic deformation, ρ_0 , is used as the initial condition in Eq. (39) and is calculated using the equations (53), (54), and (55). The constants t_0 , T_0 and N are determined from partial HIP experiments.

Microstructural Modeling to Develop Macroscopic Constitutive Laws

In general, experimental difficulties associated with instrumentation and facility capabilities preclude experimental determination of all material properties needed in the constitutive theory. For example, it will not be possible to probe the entire yield surface of a partially dense HIP powder. Thus, analytical and numerical microstructural models of the HIP process are needed to augment the understanding of the constitutive theory. This section reviews previous analysis of metal microstructural effects and discusses additional analyses performed to further define the constitutive theory.

Voids in plastically deforming metals have been modeled by several authors. Gurson (Ref. 13) has developed approximate yield surfaces for materials with microscopic voids. The principal interest in Gurson's studies was in assessing ductile fracture of polycrystalline materials containing voids or impurities which nucleate holes that microscopically grow and coalesce into a macroscopic fracture event. For porous metals, Green (Ref. 9) has assumed a yield function of the form of Eq. 9, and has evaluated the dependence of β and σ_0 on void volume ratio by modeling an isolated spherical void in a metal matrix under external hydrostatic pressure. Finite element elastic-plastic modeling of the growth of voids contained within unit cells of homogeneous material has been performed by Needleman (Ref. 11). Mullins, et al. (Ref. 24), have performed a small strain, finite element, elastic-plastic, hardening analysis of a spherical pore under remote hydrostatic pressure and have obtained results similar to Green for void shrinkage as a function of pressure. The previous analyses considered isolated voids.

Time dependent microstructural effects have been less extensively modeled. Many authors (Refs. 3-7, 25 and 26) have postulated the presence of microstructural creep mechanisms in both HIP and pressureless sintering but no definitive conclusions on the importance of these mechanisms have been reached. The most systematic approach to understanding microstructural mechanisms has been the deformation maps of Ashby (Ref. 6) discussed earlier. However, Ashby's work was directed toward determining when different mechanisms are active rather than quantifying the effect of these mechanisms on powder densification. Finite element modeling of void growth caused by steady-state creep deformation has been modeled by Burke (Ref. 27). In Burke's analysis steady-state creep was assumed, the geometry was a uniformly spaced distribution of spherical voids corresponding to a void fraction of 5 percent, and the loading was remote uniaxial tension.

The above plastic and creep analyses were concerned only with imbedded voids, but during the HIP process the initial response of the powder metal, when it is the weakest, contributes significantly to final deformations.

Models based on imbedded voids will be accurate in the final stages of densification but do not correctly represent the initial stages of densification. During the initial stages models based on the contact between spherical particles should be more accurate.

Compacting Spheres Model

An understanding of powder compaction when subjected to a uniform external pressure was formulated by considering the metal powder to be a regular array of equal size contacting spheres. A finite element model for the response of a typical sphere was arrived at by considering one spherical particle with a typical diameter. The powder was modeled as a regular array of hexagonally close packed MERL76 spheres with a diameter of 0.003 in., as shown in Fig. 9a. Actually, the MERL76 powder particles are randomly packed and range in diameter from 0.001 in. to 0.007 in. As a uniform external pressure is applied to the close packed spheres of Fig. 9a, flat contact surfaces will form centered about points of initial contact. Each of the spheres will deform to fill the adjacent void space in an identical manner. When all of void space is filled (i.e., the powder is fully compacted), each of the powder particles will be a regular twelve sided polyhedron as shown in Fig. 9b.

In the actual finite element model of the compacting spheres, the entire sphere need not be modeled. Each of the 12 contact surfaces deform in exactly the same manner, and therefore only one of the 12 five-sided pyramids shown in Fig. 10 and centered about the initial contact point, P, needs to be modeled. Each of these five sided pyramids can be divided, in several ways, into identically deforming solids. The simplest of these is a division into 5 identical four sided pyramids as shown in Fig. 10. The pyramid OPFBG shown in Fig. 10 is the geometry modeled in the finite element analysis.

The compaction process was modeled by moving the plane PKLM, in Fig. 11, along the line OP. Points on the spherical surface PFCG were free to move until they were contacted by the plane PQRS after which time they were constrained to move in the plane.

Finite Element Modeling

The model break up, material properties and loading used in the finite element analysis are described in this section. In Fig. 12 is shown an 11 element 94 node finite element model of the spherically capped pyramid OPFBG shown in Fig. 10. The model was developed using the standard three dimensional twenty-node brick element of the MARC nonlinear finite element code. Element sizes were smaller around the initial contact point, P, in order to track growth of the plastic zone size as a function of contact area size. Presently, material properties for MERL76 near HIP temperatures are not available, and therefore the properties of IN100, an alloy similar to MERL76, were used. At 2000 F IN100

exhibits a tensile yield stress of 15,000 psi, a Young's modulus of 20×10^6 psi and Poisson's ratio of 0.3.

Symmetry boundary conditions were applied to the four plane surfaces connecting the sphere center to the spherical surface. The symmetry conditions on the above four planes require that the motion of the node at the center of the sphere be completely suppressed. Symmetry boundary conditions were applied to the plane OPC shown in Fig. 14 in order to reduce the number of active degrees of freedom.

The loading condition consisted of prescribed displacements on the spherical surface PKLM of Fig. 11. As node P of Fig. 12 was moved incrementally toward the sphere center, the changing z coordinates of nodes on the sphere surface were monitored. When the z-coordinates of one of the nodes equalled that of at P in Fig. 12, the node was subsequently constrained to move in the z direction with the same displacement increments as the node at P.

Finite Element Analysis Results

The finite element analysis was terminated after sixty-six displacement increments because of large computed oscillations in reaction forces on the contact area and erratic stress behavior in the plastic zone. At the end of the analysis, the plastic zone extended over 80 percent of the model geometry and the circular contact area had a radius of 4.134×10^{-4} inches.

From the finite element results the powder apparent density was computed as a function of the externally applied pressure and the results are shown in Fig. 13. The effective external pressure P_{eff} was defined as the net force acting on the contact area divided by the area of the quadrilateral PKLM in Fig. 11. The powder density was computed using the volume OPKLM of Fig. 11, from which the density was determined.

The oscillations in the pressure in Fig. 13 and in the stresses were attributed in part to attempts by the finite element code to satisfy the plastic incompressibility constraint inside the plastic zone. Additionally, the three dimensional finite element break up employed a weighted mesh which was fine around the initial contact point P in Fig. 11 and became increasingly coarse away from P. Thus, independent of increment size, as the analysis progressed, contact area growth modeling became coarser. Also, as the analysis progressed, the displacement boundary condition increments were increased resulting in larger powder density changes per increment. In the later stages of the analyses, the sphere surface just ahead of the contact area became increasingly distorted and the powder density change, occurring between two successive surface nodes becoming part of the contact area, increased. Thus, the oscillations shown in Fig. 13 were also attributed to the analysis becoming coarser as the degree of geometric and material nonlinearity increased.

In previous work at the Research Center, an axisymmetric analysis of compacting 1.0 in. radius spheres was performed. The geometry analyzed is shown in Fig. 14 where O was the sphere center, P was the initial interparticle contact point, OP was the symmetry axis and cone OPV was the initial effective volume occupied by model geometry OPU. Effective applied pressure and powder volume were defined in a manner analogous to the three dimensional analysis and the initial density was 78 percent of full density. As in the three dimensional analysis, motion normal to line OV was suppressed. The node at O was fixed, and the model was loaded by applying incremental displacement boundary conditions to nodes on the surface UP so that the surface around node P was flattened. A Young's modulus, Poisson's ratio and yield stress were taken from Astroloy data at 1600 F as 23×10^6 psi, 0.3 and 80,000 psi, respectively. The analysis was performed in seven increments and effective applied pressure as a function of powder density is plotted in Fig. 13. As with the three dimensional model the analysis was terminated before full density was attained because of numerical instabilities.

In the axisymmetric analysis a uniform finite element break up was used permitting a smoother model of contact area growth. As a consequence, the resulting pressure versus density curve, Fig. 13, is smoother than for the three dimensional analysis. However, the axisymmetric analysis failed to converge after reaching 94 percent of full density and, as with the three dimensional analysis, stresses in the contact zone were erratic. The large jump in pressure over the last converged increment casts doubt on the results of the last increment.

The three dimensional and axisymmetric analyses differed considerably in computer time. On the UTRC UNIVAC 1110 computer, each of the sixty-six increments in the three dimensional analysis ran from 3 to 12 min. The increment time fluctuated because the number of iterations needed for the solution of an increment to converge varied between one and four. In comparison, the entire axisymmetric analysis ran in approximately 4 min.

A possible solution to the numerical instabilities in the three dimensional and axisymmetric analyses is to use a coarse mesh around the initial contact point P, and to then refine the mesh along the contact surface at points removed from point P. Initially, the contact area would be coarsely modeled when effective applied pressure, plastic zone size, plastic constraint and sphere surface distortion are small and as the analysis progresses contact area growth, position and shape would be modeled with increasing fidelity.

Discussion of Results

The finite element predictions were compared with results from elastic and plastic theories of contact (Refs. 20-31). When substantial plasticity is present, the pressure distribution over the contact surface is approximately uniform and is given by

$$P = C\sigma_y \quad (40)$$

where σ_y is the material yield stress, and $C \approx 2.75$

$$C \approx 2.75 \quad (41)$$

Equation (40) can be used to determine the initial stages of plastic densification. Consider the axisymmetric model of compacting spheres as shown in Fig. 15. The contact area is initially the point P and grows as the compaction process proceeds. When the actual contact area has radius a the effective contact area A_{eff} is the circle QW given by

$$A_{eff} = \pi h^2 \tan^2 \theta \quad (42)$$

and the effective powder volume, V_{eff} , is the cone OQW. The total load on the contact surface is assumed to be, from Refs. 3 and 4,

$$N = \pi C a^2 \sigma_y$$

whence from

$$a^2 = R^2 - h^2$$

$$(P_{eff}/\sigma_y) = N/(A_{eff}\sigma_y) = C [(R^2/h^2) - 1]/\tan^2 \theta \quad (43)$$

But if ρ_i and V_i are, respectively, initial powder relative density and effective volume and ρ is the powder relative density when the contact area radius is a , then from the conservation of mass

$$\rho_i V_i = \rho V_{eff} \quad (44)$$

Further, since the length of OP is R

$$(V_i/V_{eff}) = (R^3/h^3) \quad (45)$$

whence, from Eqs. (44) and (45)

$$(R/h)^2 = (\rho/\rho_i)^{2/3}$$

and Eq. (43) becomes

$$(P_{eff}/\sigma_y) = C [(\rho/\rho_i)^{2/3} - 1]/\tan^2 \theta \quad (46)$$

From Fig. 14 it can be seen that the initial relative density can be determined from the half angle, θ , as

$$\rho_i = \frac{2\cos^2 \theta}{1+\cos \theta}$$

The above equation can be inverted to yield

$$\cos \theta = \frac{\rho_i}{4} + \sqrt{\left(\frac{\rho_i}{2}\right)\left(\frac{1 + \rho_i}{8}\right)} \quad (47)$$

For the axisymmetric analysis of Fig. 14

$$\rho_i = 0.780$$

For the three dimensional analysis of Fig. 12

$$\rho_i = 0.755$$

The above equations imply that for the three dimensional compacting spheres analysis the effective applied pressure is given by

$$(P/\sigma_y) \approx 6.25 [(\rho/0.7557)^{2/3} - 1] \quad (48)$$

and for the axisymmetric analysis

$$(P/\sigma_y) = 7.114 [(\rho/0.78)^{2/3} - 1] \quad (49)$$

Equations (48) and (49) are plotted in Fig. 13 together with the three dimensional and axisymmetric compacting spheres results.

The agreement between Eqs. (48) and (49) and the finite element results is good and indicates that Eq. (46) may be used to model the early stages of powder densification where interparticle void space is connected.

From Eqs. (48) and (49), the external pressure necessary to fully densify the powder is $1.26 \sigma_y$. However, Eqs. (48) and (49) are derived from consideration

of only a single contact area between two spheres. In the early part of powder densification, each interparticle contact area can be considered in isolation, but as compaction proceeds neighboring contact regions in the same sphere will interact and it is expected that then Eqs. (48) and (49) will no longer hold.

In the final stages of powder densification ($\rho > 0.95$), the powder is almost a continuous mass with isolated pores. Green (Ref. 9) or Eq. (1) has modeled the contraction of an isolated pore in a perfectly plastic medium and has shown that

$$(P/\sigma_y) = -2 \ln [(1 - \rho) / 3] \quad (50)$$

which is also plotted in Fig. 13.

Equation (46) is valid only in the initial stages of densification, while Eq. (50) is valid only in the final stages of densification.

Each of these equations can be inverted to yield

$$\rho = \rho_i \left[P \frac{\tan^2 \theta}{C\sigma_y} + 1 \right]^{3/2} \quad (51)$$

during initial densification, and

$$\rho = 1 - e^{-\frac{3P}{2\sigma_y}} \quad (52)$$

during final densification.

The finite element models of compacting spheres indicate that the slope, $d\rho/dP$, of Eq. (51) is accurate for densities near the initial density and that the approach to Eq. (52) is relatively slow. Therefore, it is only necessary to require that the slope and initial density be given by Eq. (51) and that Eq. (52) is approached asymptotically for large pressures. These requirements can be satisfied by taking

$$\rho = 1 - \left(\frac{\frac{P}{\sigma_y} + P_1}{\frac{P}{\sigma_y} + P_2} \right) e^{-\frac{3P}{2\sigma_y}} \quad (53)$$

where P_1 and P_2 are constants determined by specifying the slope and density when the pressure vanishes, or from Eq. (51).

$$P_1 = (1 - \rho_i) P_2 \quad (54)$$

$$P_2 = \frac{2\rho_i}{3 \left[1 - \rho_i \left(1 + \frac{\tan^2 \theta}{C} \right) \right]} \quad (55)$$

Note that as long as $C \geq 2$ (and $0 \leq P_1 \leq 1$) that $P_2 \geq 0$ and that

$$\frac{P}{\sigma_y} + P_2 \geq 0$$

for all values of the pressure P .

Equation (53) is plotted for both the axisymmetric model initial density and the three dimensional model initial density in Fig. 13. In the section on partial HIP experiments, Eq. (53) is compared to experimental results with good agreement.

The plastic work and current void volume fraction are being used as parameters for the mechanical response of partially densified powder metals. The plastic work, void volume fraction path during a HIP cycle, where the powder metal is subjected to a pure hydrostatic pressure, can be found from

$$\dot{W}^P = \sigma_{ij} D_{ij}^P \quad (56)$$

where W^P is the plastic work
 σ_{ij} is the Cauchy Stress
 $D_{ij}^P = 1/2 (V_{i,j} + V_{j,i})$
 $V_{i,j}$ is the velocity gradient, and
 $(\dot{}) = d()/dt$

For a hydrostatic pressure

$$\sigma_{ij} = -P \delta_{ij} \quad (57)$$

and

$$\dot{W}^P = -P D_{kk}^P \quad (58)$$

From Appendix E, Eq. (E.23)

$$D_{kk}^P \approx \frac{\dot{v}}{1-v}$$

where v is the void volume fraction

Then Eq. (58) becomes

$$\dot{W}^P = \frac{-P\dot{v}}{1-v} \quad (59)$$

or

$$W^P = - \int_{v_i}^{v_f} \frac{P(v)dv}{1-v} \quad (60)$$

which is the plastic work performed between void volume fractions v_i and v_f , where

v_i is the initial void volume fraction, and
 v_f is the final void volume fraction.

A relation describing external pressure and void volume fraction must be derived, since Eq. (53) is difficult to invert. Recall that the finite element analyses indicate that the relation describing pressure as a function of void volume fraction approaches Eq. (52) as the void volume fraction approaches zero, and that for values of the volume void fraction near its initial value that the slope given by Eq. (51) is accurate. An expression of the form

$$\frac{P}{\sigma_y} = \frac{2}{3} \left[-\ln\left(\frac{v}{v_i}\right) - \left(1 - \frac{v}{v_i}\right)^2 \ln v_i + a \left(\frac{v}{v_i}\right) \left(1 - \frac{v}{v_i}\right) \right] \quad (61)$$

satisfies all of these requirements

when

$$a = \frac{C v_i}{(1-v_i) \tan^2 \theta} - 1 \quad (62)$$

Figure 16 demonstrates the agreement between Eqs. (53) and (61). In the section on experimental results, it will be demonstrated that both expressions fall well within the experimental error.

Equation (61) can now be substituted into Eq. (60) to find the plastic work as

$$\begin{aligned} \frac{W^p}{\sigma_y} = & \frac{2}{3} \left[f(1-v_f) - f(1-v_i) \right] + \eta_0 \ln \left(\frac{1-v_f}{1-v_i} \right) \\ & + \frac{\eta_2}{v_i^2} \left[\ln \left(\frac{1-v_f}{1-v_i} \right) - (v_i - v_f) - \frac{1}{2} (v_i^2 - v_f^2) \right] + \frac{\eta_1}{v_i} \left[\ln \left(\frac{1-v_f}{1-v_i} \right) - (v_i - v_f) \right] \end{aligned} \quad (63)$$

where

$$\eta_2 = a - \ln v_i$$

$$\eta_1 = a + 2 \ln v_i$$

$$\eta_0 = -\ln v_i$$

$$f(x) = \sum_{k=1}^{\infty} \frac{x^k}{k^2}$$

The function $f(x)$ is presented in Table 2.

In general the effects of plasticity and creep will be separated in order to describe the material properties. A yield function of the form of Eq. (9) is presently preferred. Two deformation measures, the void volume fraction and the plastic work, will be used to represent the dependence of the parameters in the yield function. Under these assumptions the small strain elastic-plastic stress-strain law is given by Eqs. (20), (21) and (22). The effects of large strains, using the Cauchy stress, are included in Eq. (25). A nonsymmetric stiffness matrix will result and the nonsymmetric terms will be transferred to the loading side of the equilibrium equations. The effects of creep will be divided into two parts, volumetric and deviatoric. A power law creep model will be assumed.

As a result of the three dimensional and axisymmetric finite element analysis it is concluded that (1) the axisymmetric and the three dimensional analysis predict the same pressure versus density result and (2) accurate finite element modeling of the initial elastic-plastic response and the final stages of completion is numerically difficult. It is recommended that in any future analysis a weighted finite element mesh be employed which is coarser around the initial contact point and becomes finer at points close to the sphere surface but removed from the initial contact point. Based on the finite element model of compacting spheres expressions, Eqs. (53) and (62), relating void volume fraction, or relative density, and pressure, for a powder metal subjected to pure hydrostatic compression have been derived. In addition, the plastic work done while the powder metal is subjected to a pure hydrostatic pressure has been derived.

CODE MODIFICATIONS

General Considerations

A numerical simulation of the constitutive model will be required to utilize the model in the analysis and prediction of HIP processes. The numerical simulation will also be employed in both the formulation and evaluation of the constitutive model.

There are several available finite element codes that have the large strain capability required to model the HIP process. For example, the MARC finite element code (Ref. 3), can be applied to a wide variety of nonlinear solid mechanics problems. However, none of the available codes presently contain a constitutive theory that would adequately model the HIP process.

The necessity for modeling large strains arises from the 30 percent volume reduction typically experienced during the HIP process. A finite strain elastic-plastic constitutive model the the HIP process was formulated in terms of the Jaumann rate of Cauchy stress $\dot{\sigma}_{ij}$ and the symmetric part of the velocity gradient, D_{ij} . Additionally, the simplicity of an updated Lagrangian finite element formulation of the constitutive modeled is preferred. Level H-4 of the MARC nonlinear finite element code uses the McMeeking and Rice (Ref. 18) form of this finite element formulation and permits use of constitutive models of the form Eq. (24). This code will be modified to permit the modeling of the HIP process.

In order to numerically evaluate the response of the material each of the response types will be separated. One common approach in small strain deformations (see Ref. 32) is to divide the strain rate into its elastic, plastic, creep and thermal parts. The total strian rate could then be expressed as:

$$\dot{\epsilon}_{ij} = \dot{\epsilon}_{ij}^{el} + \dot{\epsilon}_{ij}^{pl} + \dot{\epsilon}_{ij}^{cr} + \dot{\epsilon}_{ij}^{th} \quad (64)$$

where $\dot{\epsilon}_{ij}$ is the total strain rate,

$\dot{\epsilon}_{ij}^{el}$ is the elastic strain rate,

$\dot{\epsilon}_{ij}^{pl}$ is the plastic strain rate,

$\dot{\epsilon}_{ij}^{cr}$ is the creep (or time dependent) strain rate, and

$\dot{\epsilon}_{ij}^{th}$ is the thermal strain rate.

In Fig. 17 the elastic and plastic strain components are presented for a uniaxial stress-strain case. Note that in Fig. 16 a second strain rate decomposition can be considered in place of Eq. 64. For the second possibility, considering just the elastic and plastic components of the strain rate, Eq. (64) would become

$$\dot{\epsilon}_{ij} = \dot{\epsilon}_{ij}^{elpl} + \dot{\epsilon}_{ij}^{elpl} \quad (65)$$

A small strain numerical iterative procedure based on Eq. (65) for the evaluation of the elastic plastic response will be presented in next section. A parallel development based on analogous additive decomposition of the stretching tensor is straightforward.

The finite element code should contain the appropriate element types to describe the deformation of the powder metal during HIP. In the MARC H.4 large strain version, all of the solid and shell elements can be used in an updated Lagrangian formulation, including three, four and eight node isoparametric axisymmetric ring elements.

The following sections will consider in more detail: (1) iteration schemes for the solution of the resulting nonlinear system of equations and (2) the changes to the constitutive portion of the MARC code.

Plastic Iteration Procedure

Consider the case of a small strain elastic-plastic response of a typical structure. Sufficiently large applied loads will result in permanent or plastic deformation. A procedure for calculating the response of the structure undergoing plastic deformation is required. A method analogous to that presented in Ref. 32 will be discussed.

To evaluate the response of the structure, the loading history may be divided into a number of incrementally applied loading steps. Each of these load increments can then be applied sequentially to the structure. An iterative scheme is then required to calculate the response of the structure to each individual load increment.

At the beginning of a new load increment it may be assumed that the strain will change in a manner analogous to the previous increment. As an initial estimate all of the strain change is then assumed to be elastic. The change in the stresses can then be calculated using Hooke's Law or

$$\Delta\sigma_{ij} = C_{ijkl}\Delta\epsilon_{kl} \quad (66)$$

where $\Delta\sigma_{ij}$ is the incremental stress vector

$\Delta\epsilon_{kl}$ is the incremental total strain vector, and

C_{ijkl} is the matrix of elastic constants.

If the resulting total stress is within the yield surface, the matrix of material constants, L_{ijkl} is simply given by

$$L_{ijkl} = C_{ijkl} \quad (67)$$

If the resulting total stress is outside the yield surface weighted material constants and stiffness matrices will have to be calculated. It should be noted at this point that if a load increment is exceedingly large and if there is a sudden change in the type of loading, care must be taken in order to iterate to the correct solution.

If the resulting total stress is outside the yield surface, the fraction of the stress increment that remains elastic must be determined. This corresponds to $\Delta\epsilon_{ij}^{el}$ in Fig. 17. If the yield surface in stress space is considered to be given by

$$f(\sigma_{ij}) = 0,$$

then the appropriate λ in

$$f(\sigma_{ij}^{i-1} + \lambda\Delta\sigma_{ij}) = 0 \quad (68)$$

may be determined where σ_{ij}^{i-1} is the stress tensor from the previous increment. The mean material matrix is calculated from

$$L_{ijkl} = \lambda C_{ijkl} + (1-\lambda) L_{ijkl}^{e-p} \quad (69)$$

where L_{ijkl}^{e-p} is the tensor relating $\dot{\epsilon}_{ij}$ and $\dot{\epsilon}_{kl}$ in Eq. (20).

Once the tensor L_{ijkl} has been determined, standard finite element solutions can be applied to find the incremental changes in the displacements, strains and loads. For example, if the strains are given by

$$\{\Delta \epsilon\} = [\beta] \{\Delta u\} \quad (70)$$

where $\{\Delta u\}$ is the vector of incremental nodal displacements, and $[\beta]$ is the matrix relating the vector of element strains $\{\Delta \epsilon\}$ to the nodal displacements, the stiffness matrix can be found from

$$[K] = \int_V [\beta]^T [D] [\beta] dV. \quad (71)$$

The incremental nodal displacements and strains can be evaluated by solving for Δu in

$$[K] \{\Delta u\} = \{\Delta P\} + \{P-I\} \quad (72)$$

and then applying Eq. (70).

The term ΔP in Eq. (72) is the applied incremental load. The term $\{P-I\}$ is defined as the residual load correction and is added to Eq. (72) to insure the total external loads, $\{P\}$, and the total internal reactions, $\{I\}$, remain balanced over all the load increments. The relation

$$\{P\} - \{I\} = \{0\} \quad (73)$$

where

$$I = \int_V [\beta]^T \{\sigma\} dV \quad (74)$$

continues to hold throughout the loading history.

One iteration cycle is completed each time the stiffness matrix is formed and the resulting equations solved. At the end of each cycle the resulting solution must be tested for convergence. This is accomplished, by considering the ratio

$$r = \frac{\Delta E^N - \Delta E^{N-1}}{\Delta E^N} \quad (75)$$

where ΔE^{N-1} is the change in energy summed over all elements on the previous cycle and ΔE^N is the change for the present cycle.

An accurate solution will usually result if r is maintained less than 0.1 for elastic-plastic problems.

If the solution has satisfied the convergence, the stresses and strains can be updated and a new load increment added. If the solution has not converged then a new guess for the strains, based on the latest cycle, is input and the calculation procedure repeated. When the solution has not converged after a given number of cycles, the program should exit from the load incrementing loop.

Figure 18 is a flow chart illustrating the small strain elastic-plastic iteration procedure.

For finite strain plasticity the stiffness matrix has the additional terms presented in Eq. (25).

Time Effects Iteration Procedure

The metal particles will creep to fill the void space when subjected to high temperature and pressure. The reduction of void space will depend on the time that the powder is subjected to the high temperature, high pressure conditions. The creep strain rate will depend in general on the stress the accumulated creep strain, the temperature and time. To illustrate the incrementing procedure assume that the creep strain rate is normal to the Mises yield surface in stress space, then the creep strain rate is given by Eq. (25).

For a specific time increment the incremental creep strain will be

$$\Delta \epsilon_{ij}^{cr} = \dot{\epsilon}_{ij}^{cr} \Delta t. \quad (76)$$

The incremental displacements are

$$[K] \{\Delta u\} = \{\Delta P\} + \{P-I\} + \{\Delta P^*\} \quad (77)$$

where

$$\{\Delta P^*\} = \int [\beta]^T [C] \{\Delta \epsilon^c\} dV \quad (78)$$

is the pseudo-creep load and $\{\Delta \epsilon^c\}$ is the vector of element creep strain. The strain increment can be calculated from Eq. (70) and the strains, creep strains, stresses and displacements can be updated.

A convergence test on the stresses should be performed. If the algorithm has not converged a shorter time step should be used and the calculations repeated. If the criteria has been satisfied then a new time step can be added.

Note that for the time dependent effects considered the stiffness matrix, generally, has to be assembled and inverted only once with the result used in each subsequent cycle. Figure 19 is a flow chart illustrating the small strain creep iteration procedure.

Code Selection, Installation, and Testing

In addition to the MARC computer code, selected for use in the program, several other codes were examined. Table 3 lists each of the codes considered. The code selected should be able to simulate the response of the powder metal and the container. The response will be assumed to be axisymmetric and therefore axisymmetric continuum and axisymmetric shell elements should be included in the element library. Four of the eight computer programs listed do not contain axisymmetric shell elements and are therefore unsuitable. These four codes are: HONDO, FIPAX, PLANS, and NON-NISA. The HONDO code contains a very general constitutive routine that could be utilized for the non-volume preserving plasticity theory. However, HONDO does dynamic problems only and would be a cost effective approach. Both the ANSYS and ADINA codes do not have the capability to perform large strain calculations and would require extensive modifications. The NEPSAP code can perform large strain calculations but uses a total Lagrangian formulation. For reasons stated previously, an updated Lagrangian formulation is preferred.

The MARC H.4 large strain code was obtained and installed. The initial test case modeled a rigid plastic hardening tensile specimen subjected to a uniaxial stress state. The MARC code successfully simulated the large strain response of the tensile specimen. Figure 20 shows that at displacements as high as 70 percent of the original specimen length the code results were nearly identical to the theoretical values.

Code Modifications

To analyze the powder plastic flow the plasticity theory described previously must be incorporated in the MARC code. The MARC code applies the algorithm of Rice and Tracey, in Ref. 3, in the subroutine THRUS. Therefore, one approach would be to modify THRUS to include nonvolume preserving plasticity. The MARC program also contains user subroutines which the general user writes to incorporate special features of his analytical model. One of these user subroutines, HYPELA, can be used for hypoelastic material properties (i.e., nonlinear elastic material properties). Subroutine HYPELA has for input the initial strain increment, and the stress state from the previous increment. The increment number can be brought in through a COMMON block. A third approach using the user subroutines appropriate to a specialized form of viscoplasticity can also be used.

Incorporating the nonvolume preserving plasticity theory into the MARC code through the user subroutine HYPELA requires writing only the one subroutine while modifications to HTRUS would also require modifications to several connected subroutines. Therefore, the present plan is to try HYPELA and use the problem illustrated in Fig. 20 as a test case. In Appendix F the small strain elastic-plastic stiffness tensor is derived for volume preserving plasticity with isotropic hardening. If the test is successful, then adding the nonvolume preserving plasticity theory to HYPELA is trivial. If the test is unsuccessful, then the subroutine THRUS and its supporting subroutines will have to be modified.

An algorithm for nonvolume preserving plastic analysis analogous to the secant method, presented in Ref. 33, has been developed. A flow chart of the algorithm appears in Fig. 21. The input consists of the latest guess at the strain increment, the stress state from the last increment and the increment number. The first guess at the strain increment is taken to be proportional to the load increment with the proportionality constant determined by the previous load step and strain increment. In subsequent iterations the strain increment is refined by an appropriate algorithm, for example, by Newton's Method, until the load increment is satisfied. The output from the algorithm is the small strain elastic-plastic stiffness tensor (see Eq. (21)).

The first step in the algorithm is to decide whether there were any previous increments. If there were no previous increments, then the elastic-plastic properties must be input as a function of the state variables, and the state variables must be initialized. In this case, the elastic-plastic stiffness tensor is set equal to the elastic stiffness tensor and the routine is exited. If there were previous increments then a decision on whether the increment is a new increment or an iteration on an old increment must be made. If it is a new increment, then the state variables must be updated.

The program then proceeds to calculate the stress state that would result if the strain increment were all elastic. The result is designated stress state two. If stress state two is located within or on the yield surface, the elastic stiffness tensor is the appropriate tensor and the routine is exited. If stress state two is located outside the yield surface, then the strain increment is scaled so that the resulting stress state is on the yield surface. This is designated as stress state one. Rice and Tracey in Ref. 34 took the average of stress states one and two to be the stress state from which the elastic plastic stiffness matrix would be formed.

The average stress state is now scaled to bring it to the yield surface. This scaled value is designated stress state three. Stress state three is used to calculate the plastic stiffness tensor. Adding the weighted plastic stiffness tensor to the elastic stiffness tensor gives the elastic-plastic stiffness tensor. At this point the routine can be exited for classical plasticity theory for the resulting elastic-plastic stiffness tensor results gives a stress increment which will place the updated stress exactly on the yield surface. For the proposed plasticity theory this cannot be shown to be true and the stiffness tensor will have to be iteratively calculated so that it is true.

In addition to the modifications necessary to incorporate the nonvolume preserving plasticity theory a modification to include the nonsymmetric stiffness term of Eq. (25) as previously discussed is necessary.

It has been decided to use the MARC H.4 large strain computer code to simulate the deformations induced during a HIP cycle. Several methods for modifying the code have been identified and an algorithm for generating the material stiffness tensor has been selected. A method for dealing with the non-symmetric stiffness matrix has been selected. Completion of code modifications will allow analysis of the test cases, experiments, and a disk HIP to be performed during the second year of effort.

MATERIAL PROPERTY DETERMINATION

To predict the mechanical response of metal powder subjected to the HIP process it is necessary to know the mechanical properties of the metal during the HIP cycle. These mechanical properties can be obtained by removing test specimens from the HIP facility at various stages in a HIP cycle. The partial HIP samples would represent the powder at various stages for a pressure-temperature history. A complete description of the mechanical properties can then be obtained by postulating yield surfaces, flow rules, hardening laws and creep properties and comparing these predictions to the results of mechanical tests on the partial HIP samples.

Partial HIP Tests

The UTRC HIP facility has been utilized to process powder metals through temperature-pressure-time profiles closely paralleling the procedure used to fabricate full size turbine disks to near net shape. Figure 22 shows a representative temperature-time history detailing the mode of consolidation being used to fabricate full size disks. Two distinct phases of thermal history should be noted.

In the first phase (preheat) the metal powder is preheated for 3 hr at temperatures rising from 1500 F to 2000 F and then held at 2000 F for 8 hr. All of the preheat cycle is done at 1 atm pressure. During the preheat phase some sintering occurs and the powder acquires sufficient strength to be handled. In the second phase, the preheated powder sample is transferred to the HIP unit. During the first hour, the temperature and pressure are raised to 2135 F and 5000 psi, respectively. During the next 1-1/2 hr the pressure continues to rise to the full 15,000 psi. The pressure, 15,000 psi, and temperature, 3125 F, are then maintained for 3 hrs, to complete the densification.

UTRC facilities allow several partial HIP samples to be preheated simultaneously. Since the powder is initially weak a container is required to retain the powder shape for temperatures exceeding 2000 F. Therefore, during the preheat cycle the powder is encapsulated in quartz. During the preheat the density changed from 60 to 65 percent of full density initially to 65 to 70 percent of full density upon completion of the cycle. All specimens were preheated at 2000 F and 1 atm for 12 hr.

After the completion of the preheat cycle the samples have the quartz container removed and a glass container substituted. At HIP temperatures the inside surface of the glass container fuses with the outer powder metal particles and forms a gas tight seal about the powder metal. The glass has no strength or

stiffness. Consequently, a uniform hydrostatic stress is transmitted to the powder metal. The glass container with the preheated or sintered powder metal is next placed in the HIP facility and subjected to a specified temperature, pressure time cycle.

In Fig. 23, a specimen is shown in different stages of a partial HIP cycle. The specimen is shown encapsulated in quartz before the preheat cycle. A sintered or preheated bar is shown in glass before HIP, and a partially densified bar is shown with the end removed for density measurements.

A 100 lb lot of MERL 76 powder, blend 61578, was obtained and samples were subjected to sieve and chemical analyses. A comparison of the results of the blend chemical and sieve analyses with a blend used in other programs showed the two blends to be essentially identical.

The first three partial HIP experiments attempted to find a pressure at 2135 F, the standard MERL 76 HIP temperature, which induced less than full powder densification. MERL 76 powder was encapsulated in stainless steel tubes with 0.75 in. and 0.06 in. external diameter and wall thickness, respectively. After the filled tubes were outgassed to remove air, their ends were crimped and welded shut. The tubes were then sintered in a furnace for 12 hr at 2000 F and allowed to cool to room temperature. Subsequently, each tube was reheated to 1200 F, loaded into the HIP unit which was also at 1200 F, and subjected to a pressure temperature cycle. The pressure-temperature cycle for specimen 3 is shown in Fig. 24. Maximum HIP pressures for specimens 1, 2 and 3 were 5000 psi, 2500 psi and 1000 psi, respectively. Specimen 1 was held at peak pressure for 20 min while specimens 2 and 3 experienced peak pressure for only ten minutes. In all three experiments the powder was completely compacted.

It can be concluded that densification occurs so rapidly at 2135 F that HIP pressure and time cannot be controlled accurately enough to partially densify MERL 76. Therefore, present experiments are directed towards partially densifying powder in the 1600 F to 2000 F temperature range. The results obtained must then be extrapolated to predict densification rates at 2135 F.

Experiments 4, 5 and 6 investigated the short time response of powder to pressure. From these tests, it was observed that between 1600 F and 1800 F little short term densification occurs at 1000 psi. These first six tests indicated that between 1600 F and 2000 F and between 1000 psi and 15,000 psi partially densified specimens would result.

The next set of tests were performed at 1800 F and various pressure, with the maximum temperature and pressure acting for 10 minutes only. These tests were successful in producing partially dense samples. The test regime was expanded to include 1600 F, 1900 F and 2000 F at appropriate pressures and again the time at maximum temperature and pressure was held to 10 min. Finally, a set of

experiments at various times were performed to determine the effects of creep. Table 4 is a listing of each of the partial HIP experiments completed.

Some understanding of the compaction process can be obtained by applying the full density range plastic compaction model, Eq. (53) in Section 2.5. In order to apply the model the yield stress of the powder particle material must be known. This data does not exist and therefore the short time partial HIP data has to be reduced to determine the yield stress. For each of the temperature, 1600 F, 1800 F, and 2000 F, the yield stress was estimated and Eq. 53 was applied to determine the relative density for various applied pressures. Figure 25 presents the results of the calculations and demonstrates good agreement for the yield stresses chosen. In Fig. 26 the resulting yield stress is plotted as a function of temperature. Figure 26 indicates yield stresses that are somewhat low for superalloys. Three facts could account for this: (1) the yield stress for the pre-HIP powder metal is generally lower than for the fully consolidated powder, (2) the strain rate during a partial HIP cycle is relatively slow and therefore produces a somewhat lower effective yield stress, and (3) the creep rates at high temperatures are relatively high producing an apparently lower yield stress.

The effects of creep on the density can be examined by applying Eq. (39), which was derived by Wilkinson and Ashby in Ref. 22. The relative density after plastic deformation, ρ_o , is used as the initial condition in Eq. (39) and is calculated using (51). The relative density before any plastic deformation was taken as

$$\rho_i = 0.70$$

and the condition

$$\rho = \rho_o$$

was applied at

$$t = 10 \text{ min.},$$

which is the minimum time the partial HIP specimens were maintained at maximum temperature and pressure.

An analyses of the densities for the partial HIP experiments performed indicates

$$\begin{aligned} N &\approx 2 \\ t_o &\approx 2 \times 10^{-13} \text{ min} \\ T_o &\approx 73000 \text{ R} \end{aligned}$$

when

$$\sigma_0 = 15 \text{ ksi}$$

In Fig. 27, the calculated relative density is compared to their experimental values with fair agreement.

Photomicrographs of two partially dense HIP rods at 1800 F are shown in Fig. 28. The majority of the particles have remained nearly spherical, while a few particles appear to be severely deformed.

Mechanical Tests

The major objectives of the mechanical tests are to determine the yield surface and to measure the elastic properties of partial HIP metal powders and to examine hardening flow rules, and creep of the partial HIP samples. After the partially dense HIP material is removed from the furnace it must be machined into test specimens. The mechanical tests of these specimens should be performed at the HIP temperature, which is relatively high. The oxidation rates become excessive because of the large surface area due to the voids and the high temperature. Therefore, it is necessary to perform the mechanical tests in an inert environment.

To determine the shape of the yield surface several types of mechanical tests are required. Each type of test produces one point on the yield surface. There is one point on the surface that is known: the hydrostatic pressure of the HIP process. A compression test performed at temperature will provide a second point on the yield surface and will also provide some information on the elastic, hardening and plastic flow of the material. A tension test performed at temperature, when compared to a compression test performed at temperature, will determine the symmetry of the yield surface. In addition, creep tension tests at the HIP temperature will be required to determine accurately the creep properties of the partially dense metal powder. In Fig. 29, a compression, tension and creep specimen of powder metal is illustrated. Two partial HIP bars are required to construct all the test specimens illustrated in Fig. 28. The compression tests are the most important tests to be performed since they produce a hydrostatic pressure which is the predominant loading feature during a HIP cycle. Two deformation measures will be used to characterize the yield surface; the void volume fraction and the plastic (nonrecoverable) work. Therefore, the measurement of the axial length change will not be sufficient to determine the mechanical response and a measurement of the volume will also be required. The final volume of a compression specimen can be measured after a completed test but this does not provide a complete description of the path to the final state.

A method which might be useful for measuring the volumetric deformation during compression testing is being developed by the UTRC Optics and Acoustics Group. The method has been demonstrated in a bench test. The method uses interference patterns from the optically rough surface of a mechanical test specimen, and is referred to as speckle interferometry. Note that in Fig. 40 the compression sample has a roughened surface. The volumetric measurements must be made on the MERL 76 test specimens while they are in a furnace operating at temperatures between 1600 and 2000 F. In addition, at these temperatures, the porous nature of the MERL 76 will provide ample surface area for oxidation to occur, and therefore the specimens must be tested in an oxygen free environment. Speckle interferometry allows for determining the displacements of several points on the sample without actually having to provide extensometry. It is hoped that it will be possible to perform the speckle interferometric measurements during some of the compression and tension tests to characterize the volume changes.

To date eighteen compression tests have been performed. Three of these tests were used to size the compression specimens and determine the test conditions. The remaining tests were all completed in the same manner. Figure 30 illustrates the typical output. The specimens consisted of a right circular cylinder 0.5 in. long by 0.2 in. in diameter. Each specimen was placed in a furnace in an inert gas and brought up to the temperature at which the specimen was hot isostatically pressed. At temperature the specimen was subjected to compression crosshead displacement rate of 0.0025 in./min and the load was recorded. After the load leveled out, the crosshead rate was doubled to 0.005 in./min and after the load again leveled out, the crosshead displacement was fixed and the load recorded as a function of time. The specimen volumes were measured before and after the tests and do not show a significant change in volume but do illustrate a significant change in height and radius. Table 5 summarizes the compression experiments performed and the volume measurements made, while Table 6 presents the average geometry changes.

The test plan also includes about fifteen tension tests, at temperature, for the purpose of determining the symmetry of the yield surface with respect to hydrostatic pressure. About ten creep tests are presently planned for determining the porous material flow rates at high temperatures.

The partial HIP experiments have been completed and analyzed. The analytical expressions derived to describe the final density, Eqs. (29) and (53) are in good agreement with the experimental results. The mechanical test program has been defined and initiated. Some preliminary analyses of the mechanical tests have been completed, and indicate that there is little change in volume after compression testing. A method for measuring the volume change during the mechanical testing is being developed by the UTRC Optics and Acoustics Group.

MODEL VERIFICATION

Verification Criteria

The constitutive theory developed and supported by the mechanical tests of partial HIP samples will be validated through a series of experiments. The validation test results will be correlated with results of the numerical simulation of the experiment. Although a one-dimensional configuration would be the easiest to model and simulate, a two-dimensional axisymmetric validation configuration will provide conditions analogous to those experienced in the actual HIP process.

The validation tests must be designed to avoid duplication of the uniform hydrostatic stress state of the partial HIP tests. The experiments must therefore result in a nonvanishing shear stress within the sintered material. A nonhydrostatic stress state can be achieved with the application of the uniform external pressure if the material has nonhomogenous properties. This may be achieved by imbedding in the metal powder a different material, for example, steel or fully compacted powder spheres or cylinders. Such an experimental configuration will produce a nonhydrostatic stress state and will make use of existing hardware and techniques.

The microscopic examination of the experimental specimen will produce a measure of density as a function of the distance from the center of the inclusions. The density can also be determined by measuring the hardness at a point and then deriving the density from a known hardness-density relationship. The experimentally measured spatial variation in density will then be compared to the results of the numerical simulation. This correlation of the experimental and numerical results will provide a validation of both the constitutive model and the numerical simulation. Two particular configurations have been identified for possible use in the validation tests. One configuration employs spheres and the other cylindrical rods imbedded within the powder.

An additional validation experiment could subject a partially dense bar to uniaxial compression. The bar could then be subjected to second HIP and the density measured. This test would follow a loading path not previously investigated and the final density could be used as a measure of the accuracy or limitations of the theory.

Presently the imbedded sphere or cylinder experiment is preferred and will be discussed in the following sections.

Spherical Inclusions

As an approximation to a spherical inclusion in a partially compacted powder consider the case of a rigid sphere buried in an infinite isotropic elastic solid. The compacting powder will have two elastic parameters, for example, Young's modulus and Poisson's ratio, which will be functions of position and will depend upon the stress history at the particular point in the powder. In turn the stress history will be a function of the loading and the boundary conditions. Appendix G presents the solution for the spatial stress distributions about a rigid sphere imbedded in an isotropic homogeneous elastic solid of infinite extent and subjected to a hydrostatic pressure. Figure 31 presents a plot of the second invariant of the deviatoric stress tensor as a function of position from the center of a 0.5-in. dia sphere. The radial change in the second invariant will result in every radial point exhibiting a different stress history and producing a different final density. Note from Fig. 31 that most of the variation will occur in a distance 0.25 in. from the surface of the sphere. Accurate measurements of density as a function of position would be required to validate the constitutive model with this experiment. The powder metal particle size is on the order of .002 to .007 in., and 0.25 in. variation should be more than sufficient to get an accurate representation of the density.

Figure 32 presents a possible experiment which could fit within the existing furnace. It would have three imbedded solid spheres of 0.5 in. dia, a total length of about 9.0 in. and a radius of 3.0 in. This should provide enough volume for the spheres to be imbedded in a solid of apparent infinite extent. Figure 31 again shows that at a distance of 1.0 in. from the center of the sphere, the effects of the spheres should be negligible.

Initially the spheres will be buried in a very weak powder and it will be necessary to consider the effects of the sphere weight on the powder. A simple calculation (i.e., multiplying the fractional increase in weight density by the diameter of the sphere) shows this effect should produce a stress on the order of 1/30 psi or 1/500 of an atmosphere. This is relatively small compared to the applied pressures.

For partially dense HIP samples reaching temperatures on the order of 1600 F, steel spheres could be used initially. For higher temperatures it might be desirable to use spheres made from the same metal as the compacting powder because of their higher melting point.

Cylindrical Inclusions

Consider the case of a rigid cylindrical rod buried in an infinite homogenous elastic powder in a plane strain situation. The powder itself will have no resultant axial motion near the rod if it is bonded to the rigid rod. Appendix H is a derivation of the response of a rigid cylindrical rod imbedded in a homogenous, isotropic elastic metal powder. Figure 33 presents a plot of the second invariant of the deviatoric stress as a function of position from the center of a 0.5 in. dia rod. The variation with position is a function of the square of the distance from the center of the rod. The maximum value obtained for the second invariant of the deviatoric stress is less for the cylinder than for the sphere. Most of the effects of the cylindrical inclusion will be negligible after a distance of about 0.5 in. from the center of the cylindrical rod.

Figure 34 presents a possible configuration for an experiment that could be performed within the existing furnace. The length would be approximately 9.0 in. with an imbedded 0.5 in. dia cylinder approximately 6.0 in. long. The pressurizing gas would be prevented from entering into the center of the rod by a cap of contained metal powder.

Weight effects are more important for the cylindrical inclusions and are now on the order of 0.6 psi or about 1/20 atm. The effects of the weight should still be negligible when compared to the applied pressures.

The cylindrical inclusion problem in itself is not one-dimensional. At the ends of the rod a two-dimensional stress state exists because of the shear stresses set up between the powder metal and the initially rough rod. The resulting two-dimensional, axisymmetric stress distribution can be analyzed using the modified finite element program.

Note that if the solutions presented in Appendices G and H are extended to elastic spheres and rods, the stress distribution in the powder will depend only on the bulk modulus of the imbedded material. Therefore, if the imbedded material becomes fluid, it would respond in essentially the same manner as the solid material. The pressures that would have to be applied at a sufficiently low rate in order to reduce the shear stresses due to viscosity.

Yield Surface Considerations

Consider the yield function Eq. 9. Figure 35 presents the location of the yield point of the various mechanical tests on the yield surface, and includes the variation of the spherical and cylindrical inclusions near the yield surface. Note that the region in which the validation experiment will lie is near the pure hydrostatic stress state where component manufacturing occurs.

Thermal Effects

Two thermal effects may be of importance in the design of the validation experiment: (1) the thermal coefficient of expansion and (2) the temperature distribution in the test specimen. The inclusions must have a thermal coefficient of expansion that is greater than that of the metal powder in order to retain contact between the inclusion and the powder. This will induce thermal stresses from the temperature increase. The difference in thermal expansion coefficients should, therefore, be kept as small as possible. Completely densified powder metal inclusions are preferred to steel inclusions because the thermal coefficient of expansion of the powder particles is the same as that of the inclusion. The only difference between the powder metal and the solid metal will be due to sintering which tends to bring the powder particles together.

Consideration must also be given to the temperature distribution in the sample test. Consider the case of a solid cylinder subject to a surface temperature that is a linear function of time. The steady temperature difference between the center and outside surface of the cylinder is given by (see Appendix I).

$$\Delta T = \frac{\rho c \dot{T}_0 a^2}{4K} \quad (79)$$

where ΔT is the temperature difference,

ρ is the density,

c is the specific heat,

K is the thermal conductivity,

\dot{T}_0 is the rate of increase of temperature at the outer surface, and

a is the radius of the cylinder.

The specific heat and the density for the case of an Astroloy powder can be determined from the material properties of densified powder. The thermal conductivity of the powder must be reduced from that of the metal since the powder will have only a finite contact area between adjacent particles. We will therefore assume that 1/20 of the total surface area of each powder particle is in contact with adjacent particles, thus reducing the thermal conductivity. This will produce a steady temperature difference of 50 F for a 200 F/hr increase in temperature on the outside surface for the configurations in Figs. 42 and 44. For the partial HIP bars of Fig. 31 the temperature difference is only 12.5 F.

At 1600 F, a 50 F difference in temperature represents a 70 percent decrease in strength. The thermal conductivity of the powder therefore sets limits on the rate that at which the temperature can be increased in the HIP furnace. This initial estimate does not include radiation which would reduce the temperature difference. Therefore a more accurate estimate of the equivalent thermal conductivity is required.

60

HIP PROCESS SENSITIVITY STUDIES

The objective of this task is to develop a finite element methodology for the efficient modeling of shape changes in the HIP process. The task has not yet been initiated and will be completed during the second year of the effort. Thus a methodology for analyzing the HIP process must be established and the most important assumptions in the analysis identified. In this section the finite element analysis of the HIP process is described, variables in the analysis are identified, and the analyses for determining critical parameters and variables are reviewed.

The formulation of a finite element analysis requires the specification of a finite element mesh, material properties, external loads histories and boundary conditions. Additionally, since both material and geometric nonlinearities will be present, the finite element analysis must be incremental. Consequently an incrementing procedure must be established.

The geometry of a HIP configuration consists of a metal container which encapsulates a metal powder. For the applications considered in this program the geometry will be axisymmetric. The container will be modeled with axisymmetric thin shell elements and the powder with axisymmetric ring elements. The MARC code possesses both ring and shell elements. The axisymmetric ring elements are the three node triangular element and the four and eight node isoparametric quadrilateral elements. Thus it is expected that this element will be employed to model the powder. For the thin shell element model of the container a two node axisymmetric membrane and bending element will be used. The axisymmetric solid elements can be generated using the MARC two-dimensional mesh generator. The thin shells must be generated manually.

The container elastic, plastic and creep material properties will be modeled using the finite strain analogs of the classical, incompressible plasticity and creep theories. Thus the container material will be characterized in terms of its uniaxial plastic and creep response at HIP temperatures. These data have been developed separately from the proposed program, in Ref. 2. The powder constitutive model will be the theory developed in the program. Presently the effect of creep deformation, on final shape is unknown. If creep deformations were found to be unimportant, significant savings in the development of powder material properties would accrue. It is also possible that the major plastic deformation is volume shrinkage accompanied by small deviatoric strains and rotations. Should this be the case, then savings in computation costs would be realized through simplification in stress and strain measure computations.

In the HIP process three load types are present; gravity, the externally applied increasing pressure field and temperature loads. All three loads must be modeled. Experimental evidence from the HIP of full scale disks has shown

that gravitational loads produce gross distortion of the HIP containers not adequately supported around their base. The pressure load applied to the internal surface of the container is the principal driving force for powder consolidation. Finally the effects of possible inhomogeneous temperature distributions must be considered since container and powder material properties are temperature dependent. Temperature gradients cause thermal stresses in the powder and the container, as well as inducing inhomogeneous compaction in the powder. Thus the effects of temperature gradients should be investigated.

Displacement boundary conditions must be specified to complete the definition of the HIP configuration to be modeled. The boundary conditions which model the HIP container support are simply no motion in the vertical direction at the container base. The evolving boundary conditions between the container and powder are not presently understood. Initially the powder is free to move relative to the container except on the container lower horizontal surfaces where the powder weight may be assumed to inhibit motion. As the temperature in the container and powder increase, differences in container and powder thermal expansion will result in either (1) a gap between the container sides and top, and the powder or (2) compressive stresses being exerted on the powder by the container. Irrespective of which of these conditions holds, it has been experimentally observed that at the end of the HIP process the container and powder are fused together. If there is an initial gap between the powder and container, the interior surfaces of the container walls and top are initially unsupported. The pressure loads are carried by the container alone causing the container walls to deform before contacting the powder. This nonuniform deformation in the container could contribute to nonuniformities in the final HIP geometry. Thus the closing of any gaps between the powder and container should be modeled using the gap element technology in the MARC code. If the container is always in contact with the powder, an approximation to the container-powder interface would be complete bonding for the entire HIP cycle. Such an approximation can be implemented by specification of multi-point constraints. The presence and size of gaps between the container and powder can be determined from the thermal expansion coefficients of the powder and container materials. Even if gaps are present, the effect of neglecting them should be determined because of the simplification that would occur in the analysis.

After the input data for the HIP analysis have been assembled an incremental analysis will be performed. Thus increment sizes and increment convergence criteria must be established. Increment size is controlled by the rate at which changes in material properties and geometry occur. Typically material properties change faster than the geometry so that it is unnecessary to account for geometry changes at every increment. The frequency with which the deforming geometry should be updated must be determined.

An examination of the sensitivity of HIP finite element analysis will be conducted. Parameters which will be examined include:

1. Inclusion of powder creep deformations
2. The assumption that rotations and deviatoric strains in the powder are small relative to volumetric strains.
3. Temperature gradients in the powder
4. Gaps between powder and container walls
5. Increment size and convergence criteria
6. The frequency with which coordinates of the deforming geometry are updated.

To assess the sensitivity of the HIP process analysis variables a HIP geometry will be selected for which documented initial and final dimensions exist. It is presently expected that a HIP disk from the present Pratt and Whitney Air Force Contract (Ref. 2) will be selected. Two finite element breakups could be generated. The first breakup would be relatively simple, but sufficient to model overall container and powder response. Local deformations caused by container corners and container powder interactions would not be included in this model. Only variables (2) and (4) of the previous list are strongly dependent on container and powder interactions. The effects of the remaining variables will be investigated independently using the simple finite element breakup. Recommendations for inclusions of these variables in the HIP analysis will be made.

The second finite element breakup would be more detailed and will permit investigation of the interactions between the powder and container. The effects of large rotations and shears near container corners will also be investigated with the more detailed model.

REFERENCES

1. Anon: Manufacturing Methods for Superalloy Powder Production and Consolidation (1973). Air Force Contract F33615-73-C-5040.
2. Cheverton, K. J.: Analysis of Container Shape Change During Hot Isostatic Pressing. UTRC Report R79-217590, September, 1979.
3. Wilkinson, D. S. and M. F. Ashby: The Development of Pressure Sintering Maps. Sintering and Catalysis Materials Science Research, Vol. 10, G. C. Kuczynski, Ed., Plenum Press, p. 473-492 (1975).
4. Notis, M. R., R. H. Smoak and V. Krishnamachari: Interpretation of Hot Pressing Kinetics by Densification Mapping Techniques, Ibid., p. 493-507.
5. Ramquist L.: Theories of Hot Pressing, Powder Metallurgy, Vol. 9, No. 17, p. 1-25 (1966).
6. Ashby, M. F.: A first Report on Deformation-Mechanism Maps. Acta Metallurgica, Vol. 20, p. 887-897 (1972).
7. Notis, M. R.: Pressure Sintering and Creep Deformation - A Joint Modeling Approach. Powder Metallurgy International, Vol. 6, No. 2, p. 82-84 (1974).
8. Torre, C.: Berg-Huttermann, Montash, Montan. Hochschule Loeben, Vol. 93 p. 62 (1948).
9. Green, R. J.: A Plasticity Theory for Porous Solids. International Journal for Mechanical Sciences, Vol. 14, p. 215-224 (1972).
10. Suh, N. P.: A Yield Criterion for Plastic, Frictional, Work-Hardening Granular Materials. International Journal of Powder Metallurgy, Vol. 5, p. 69-87 (1969).
11. Needleman, A.: Void Growth in an Elastic Plastic Medium, Journal of Applied Mechanics, Vol. 39, p. 964-970 (1972).
12. Shima, S. and M. Oyane: Plasticity Theory for Porous Metals, International Journal of Mechanical Science, Vol. 18, p. 285-291 (1976).
13. Kuhn, H. A. and C. L. Downey: Deformation Characteristics and Plasticity Theory of Sintered Powder Materials, Internal Journal of Powder Metallurgy, Vol. 7, p. 15-25 (1971).

REFERENCES (Cont'd)

14. Bodner, S. R. and Y. Partom: Constitutive Equations for Elastic-Visco Plastic Strain Hardening Materials. *Journal of Applied Mechanics, Transactions of the ASME*, June 1975, p. 385-389.
15. Corapcioglu, Y. and T. Vaz: Constitutive Equations for Plastic Deformation of Porous Materials. *Powder Technology*, Vol. 21, 1978, p. 269-274.
16. Parks, D. M.: "Finite Deformation Plasticity Formulation for Compacting Metal Powders". Communication to B. N. Cassenti, dated March 25, 1979.
17. Hibbett, H. D., P. V. Marcal and J. R. Rice: A Finite Element Formulation for Problems of Large Strain and Large Displacement, *International Journal of Solids and Structures*, Vol. 6, p. 1069-1086 (1970).
18. McMeeking, R. M. and J. R. Rice: Finite-Element Formulations for Problems of Large Elastic-Plastic Deformation. *International Journal of Solids and Structures*, Vol. 10, p. 321-339 (1974).
19. Prager, W.: *Introduction to Mechanics of Continua*, Ginn and Co., Boston (1961).
20. Nagtegaal, J. C. and J. E. deJong: Some Computational Aspects of Elastic-Plastic Large Strain Analysis. MARC Analysis Research Corporation, Palo Alto, California.
21. Penny, R. K. and D. L. Marriott: *Design for Creep*. McGraw Hill Book Co., New York (1971).
22. Wilkinson, D. S. and M. F. Ashby: Pressure Sintering by Power Law Creep. *Acta Metallurgica*, Vol. 23, 11/75, pp. 1277-1285.
23. Gurson, A. L.: Continuum Theory of Ductile Rupture by Void Nucleation and Growth: Part 1. Yield Criteria and Flow Rules for Porous Ductile Media. ERDA Contract E(11-1)-3084 Technical Report No. 39 (1975).
24. Mullins, M., M. Gadala and M. A. Dokainsh: Effects of Void Separation and Strain Hardening on Porous Material Plasticity in Applications of Computer Methods in Engineering, Vol. 1, University of Southern California Press, p. 455-460 (1977).
25. Kuczynski, G. C.: Fundamentals of Sintering Theory in Powder Metallurgy for High Performance Applications. J. J. Burke and V. Weiss Editors, Syracuse University Press, p. 101-117 (1972).

REFERENCES (Cont'd)

26. Johnson, D. L.: Recent Developments in the Analysis of Sintering Kinetics, Ibid, p. 139-149.
27. Burke, M. A.: Applications of the Finite Element Method to the Study of Plastic Instabilities in Tension. Ph.D. Dissertation, Stamford University (1977).
28. Lubkin, J. L.: Contact Problems. In Handbook of Engineering Mechanics, W. Flugge, editor, McGraw Hill, 1962.
29. Waterhouse, R. B.: Fretting Corrosion. Pergamon 1972.
30. Johnson, K. L.: An Experimental Determination of the Contact Stresses between Plastically Deformed Cylinders and Spheres. In Engineering Plasticity. J. Heyman and F. A. Leckie Editor, Cambridge University Press, p. 341-361, 1968.
31. Francis, H. A.: Phenomenological Analysis of Plastic Spherical Indentation. ASME Journal of Engineering Materials and Technology. p. 272-81, 1976.
32. Anonymous: MARC:CDC Nonlinear Finite Element Computer Program, Vols. 1-3, Control Data Corporation (1977).
33. Rice, J. R., and D. M. Tracey: Computational Fracture Mechanics. In the Proceedings of the Symposium on Numerical and Computer Methods in Structural Mechanics, Urbana, Illinois, 1971, edited by S. J. Fenues, pp. 585-623, Academic Press, New York, 1973.
34. Sokolnikoff, J. S.: Mathematical Theory of Elasticity. McGraw Hill Book Co., New York, 2nd Edition (1956).

APPENDIX A

THE FORM OF THE FINITE ELEMENT STIFFNESS MATRIX FOR PLASTICITY THEORIES WITH NONASSOCIATED FLOWS RULES

It is shown that in contradiction to plasticity theories with associated flow rules, a nonassociated flows rule leads to a nonsymmetric finite element stiffness matrix. The pertinent equations of small strain nonhardening elasto-plastic constitutive theory are:

- (1) the yield function

$$f(\sigma_{ij}) = 0 \quad (A.1)$$

- (2) the consistency rule

$$\dot{f} = \frac{\partial f}{\partial \sigma_{ij}} \dot{\sigma}_{ij} = 0 \quad (A.2)$$

when plastic deformation is occurring

- (3) an additive decomposition of strain rate into elastic and plastic parts:

$$\dot{\epsilon}_{ij} = \dot{\epsilon}_{ij}^e + \dot{\epsilon}_{ij}^p \quad (A.3)$$

where superscripts e and p denote elastic and plastic parts of the strain rate respectively,

- (4) an elastic stress strain law

$$\dot{\sigma}_{ij} = C_{ijkl} \dot{\epsilon}_{kl}^e \quad (A.4)$$

and

- (5) a plastic constitutive assumption

$$\dot{\epsilon}_{ij}^p = \lambda \frac{\partial g}{\partial \sigma_{ij}} \quad (A.5)$$

which assumes the existence of a plastic potential $g(\sigma_{ij})$. When $g = f$ flow rule Eq. (A.5) is called associated and, geometrically, $\dot{\epsilon}_{ij}^p$ is perpendicular to the yield surface. When $g \neq f$ the rule is nonassociated.

From substituting Eqs. (A.3) - (A.5) into Eq. (A.2) and rearranging it follows that

$$\dot{\lambda} = \frac{\partial f / \partial \sigma_{ij} C_{ijkl} \dot{\epsilon}_{kl}}{\partial f / \partial \sigma_{rs} C_{rstu} \partial g / \partial \sigma_{tu}} \quad (A.6)$$

Substituting Eq. (A.6) into the incremental law

$$\dot{\sigma}_{ij} = C_{ijkl} (\dot{\epsilon}_{kl} - \dot{\epsilon}_{kl}^p)$$

we obtain

$$\dot{\sigma}_{ij} = L_{ijkl} \dot{\epsilon}_{kl}$$

where

$$L_{ijkl} = C_{ijkl} - \frac{C_{ijpq} \partial f / \partial \sigma_{mn} C_{mnkl} \partial g / \partial \sigma_{pq}}{\partial f / \partial \sigma_{rs} C_{rstu} \partial g / \partial \sigma_{tu}} \quad (A.7)$$

For L_{ijkl} to possess the symmetry

$$L_{ijkl} = L_{klij} \quad (A.8)$$

we must have

$$C_{ijpq} C_{mnkl} \left(\frac{\partial f}{\partial \sigma_{mn}} \frac{\partial g}{\partial \sigma_{pq}} - \frac{\partial f}{\partial \sigma_{pq}} \frac{\partial g}{\partial \sigma_{mn}} \right) = 0$$

or, since C_{ijpq} and C_{mnkl} are invertible

$$\frac{\partial f}{\partial \sigma_{mn}} \frac{\partial g}{\partial \sigma_{pq}} = \frac{\partial f}{\partial \sigma_{pq}} \frac{\partial g}{\partial \sigma_{mn}} \quad (A.9)$$

If $f \neq g$ then (A.9) is not, in general, true and (A.8) no longer holds. This in turn implies that finite element stiffness materials computed from Eq. (A.7) are no longer symmetric and consequently cannot be incorporated directly into standard finite element codes since the matrix inversion algorithm of such codes assume stiffness matrices to be symmetric.

APPENDIX B

VOLUMETRIC COMPRESSION IN MOHR-COULOMB THEORIES OF PLASTICITY

For Mohr-Coulomb theories of plasticity to model the HIP process a permanent volume shrinkage must be predicted for a state of hydrostatic, compressive stress. The following discussion shows that Mohr-Coulomb theories do not admit irreversible volume shrinkage.

The yield surfaces for linear and parabolic Mohr-Coulomb theories are

$$f_1(\sigma_{ij}) = \beta I_1 + \sqrt{J_2} = \tau_o \quad (B.1)$$

and

$$f_2(\sigma_{ij}) = \beta I_1 \tau_o + J_2 = \tau_o^2 \quad (B.2)$$

respectively, where I_1 is the first stress invariant or three times the mean Cauchy stress, $\sigma_{kk}/3$; J_2 is the second invariant of the deviatoric stress S_{ij} ;

$$J_2 = \frac{1}{2} S_{ij} S_{ij}, \quad S_{ij} = \sigma_{ij} - \frac{\sigma_{kk}}{3} \delta_{ij}, \quad (B.3)$$

τ_o is the yield stress in pure shear and β relates yield stress in pure shear to yield stress in purely hydrostatic stress. In Eqs. (B.1) and (B.2) $\beta > 0$ so that yielding can occur in hydrostatic tension but not compression.

For an associated flow rule

$$\dot{\epsilon}_{ij}^p = \dot{\lambda} \frac{\partial f}{\partial \sigma_{ij}}$$

With f equal f_1 and f_2 in turn we obtain, from Eqs. (B.1) and (B.2)

$$\dot{\epsilon}_{ij}^p = \dot{\lambda} \left(\beta \delta_{ij} + \frac{1}{2\sqrt{J_2}} S_{ij} \right) \quad (B.4)$$

and

$$\dot{\epsilon}_{ij}^p = \dot{\lambda} \left(\beta \tau_o \delta_{ij} + S_{ij} \right) \quad (B.5)$$

for linear and parabolic Mohr-Coulomb theories respectively. Clearly for plastic shear strain to occur in the same direction as shear stress $\dot{\lambda} \geq 0$. The volumetric plastic strain is given by

$$\dot{\epsilon}_{ii}^P = 3\dot{\lambda}\beta \text{ on } \dot{\epsilon}_{ii}^P = 3\dot{\lambda}\beta \tau_o, \quad (\text{B.6})$$

for the two theories. Since $\dot{\lambda}\beta$ and τ_o are not negative, no plastic volume shrinkage is possible.

APPENDIX C

PLASTIC VOLUMETRIC STRAIN UNDER PURE SHEAR STRESS

It is shown that unlike the Mohr-Coulomb theories of plasticity, the yield functions to be considered in the program do not predict volumetric plastic strains for states of pure shear. Consider the following yield surfaces:

$$f_1(\sigma_{ij}) = \beta I_1 + \sqrt{J_2} - \tau_0 = 0, \quad (C.1)$$

$$f_2(\sigma_{ij}) = \beta \tau_0 I_1 + J_2 - \tau_0^2 = 0, \quad (C.2)$$

$$f_3(\sigma_{ij}) = \beta \left(\frac{I_1}{3} \right)^2 + J_2 - \tau_0^2 = 0, \quad (C.3)$$

where the nomenclature is as in Appendix B. Equations (C.1) and (C.2) correspond to the linear and parabolic Mohr-Coulomb theories respectively, while Eq. (C.2) is Eq. (3.23) presented in Section 3.1. When an associated flow rule is assumed, plastic strain increments for these theories are given by

$$\dot{\epsilon}_{ij}^p = \dot{\lambda} \frac{\partial f}{\partial \sigma_{ij}} \quad (C.4)$$

where f is f_1 , f_2 or f_3 . Since

$$\frac{\partial I_1}{\partial \sigma_{ij}} = \delta_{ij} \quad \text{and} \quad \frac{\partial J_2}{\partial \sigma_{ij}} = S_{ij}$$

where δ_{ij} is the usual Kronecker delta function and S_{ij} is the deviatoric stress:

$$S_{ij} = \sigma_{ij} - \frac{1}{3} \sigma_{kk} \delta_{ij}.$$

Thus, the flow rules corresponding to Eqs. (C.1), (C.2) and (C.3) are

$$\dot{\epsilon}_{ij}^p = \dot{\lambda}_1 \left(\beta \delta_{ij} + \frac{1}{2} \frac{S_{ij}}{\sqrt{J_2}} \right) \quad (C.5)$$

$$2\dot{\epsilon}_{ij}^P = \dot{\lambda}_2 (\beta \tau_o \delta_{ij} + S_{ij}) \quad (C.6)$$

$$3\dot{\epsilon}_{ij}^P = \dot{\lambda}_3 \left(\frac{2\beta}{9} I_1 \delta_{ij} + S_{ij} \right) \quad (C.7)$$

where the $\dot{\lambda}$'s are different in each equation. The plastic volumetric strains corresponding to each flow rule are

$$\dot{\epsilon}_{kk}^P = 3\dot{\lambda}_1 \beta, \quad 2\dot{\epsilon}_{kk}^P = 3\beta \dot{\lambda}_2 \tau_o, \quad 3\dot{\epsilon}_{kk}^P = \frac{2}{3} \beta \dot{\lambda}_3 I_1.$$

In a state of pure shear stress $I_1=0$ so $3\dot{\epsilon}_{kk}^P = 0$ while, when the shear stress is high enough to cause yield, $\dot{\lambda}_1$ and $\dot{\lambda}_2$ and hence, $1\dot{\epsilon}_{kk}^P$ and $2\dot{\epsilon}_{kk}^P$ are nonzero.

Equation (C.3) is a special case of yield surfaces of the form

$$f(I_1, J_2) = 0, \quad (C.8)$$

$$f(I_1, J_2) = f(-I_1, J_2) \quad (C.9)$$

For an associated flow rule Eq. (C.8) implies

$$\dot{\epsilon}_{ij}^P = \dot{\lambda} \left(\frac{\partial f}{\partial I_1} \delta_{ij} + \frac{\partial f}{\partial J_2} S_{ij} \right). \quad (C.10)$$

From Eq. (C. 3) it follows that

$$\frac{\partial f}{\partial I_1} (I_1, J_2) = - \frac{\partial f}{\partial I_1} (-I_1, J_2)$$

so

$$\frac{\partial f}{\partial I_1} (0, J_2) = 0. \quad (C.11)$$

Consequently, for materials whose yield surface satisfies Eqs. (C.8) and (C.9) the plastic strain corresponding to pure shear stress is given by Eqs. (C.10) and (C.11):

$$\dot{\epsilon}_{ij}^P = \dot{\lambda} \frac{\partial f}{\partial J_2} S_{ij} \quad (C.12)$$

which implies that no plastic volumetric strain occurs.

APPENDIX D

YIELD SURFACE CONSIDERATIONS

A large strain theory of plasticity with several hardening parameters based on Eq. (8), can be developed by decomposing the symmetric part of the velocity gradient tensor, D_{ij} , into elastic and plastic parts, or

$$D_{ij} = D_{ij}^e + D_{ij}^p \quad (D.1)$$

where

$$D_{ij} = 1/2 (V_{i,j} + V_{j,i})$$

V_i are the velocity components, and

$$(\)_{,j} = \partial(\)/\partial x_j$$

Parallel to classical plasticity, a yield function $f(\sigma_{ij}, h_\alpha)$ is assumed to exist where σ_{ij} , $i, j = 1, 2, 3$ is the usual Cauchy stress tensor and h_α , $\alpha = 1, 2, \dots, n$, is a set of deformation dependent material parameters. When

$$f(\sigma_{ij}, h_\alpha) < 0 \quad (D.2)$$

only elastic deformation occurs and when

$$f(\sigma_{ij}, h_\alpha) = 0 \quad (D.3)$$

both elastic and plastic deformations are possible

Parameters h_α , are assumed to be functions of a set of deformation measures η_β , $\beta = 1, 2, \dots, n$, or

$$h_\alpha = h_\alpha(\eta_\beta) \quad (D.4)$$

and the deformation measures are assumed to be defined in terms the non-recoverable strain history.

Equation (D.3) holds during plastic deformation and therefore:

$$\dot{f} = (\partial f / \partial \sigma_{ij}) \dot{\sigma}_{ij} + (\partial f / \partial h_\alpha) \dot{h}_\alpha = 0 \quad (D.5)$$

In Eq. (D.5) and all subsequent equations, the usual summation convention is used with repeated lower case Latin subscripts being summed over the range 1, 2, 3 and Greek subscripts having the range 1, 2, \dots, n .

The plastic deformation rate D_{ij}^p is assumed to be given by an associated flow rule

$$D_{ij}^p = \dot{\lambda} \partial f / \partial \sigma_{ij} \quad (D.6)$$

where $\dot{\lambda}$ is a positive, plastic strain history dependent, scalar. From Eq. (D.4)

$$\dot{h}_\alpha = (\partial h_\alpha / \partial \eta_\beta) \dot{\eta}_\beta \quad (D.7)$$

Assuming that $\dot{\eta}_\beta$, $\beta = 1, 2, \dots, n$ satisfies

$$\dot{\eta}_\beta (m \dot{D}_{ij}^P) = m \dot{\eta}_\beta (\dot{D}_{ij}^P) \quad (D.8)$$

for all positive scalars m , it follows that

$$\dot{\eta}_\beta = \dot{\lambda} k_\beta (\sigma_{ij}) \quad (D.9)$$

From Eqs. (D.7), (D.9) and Eq. (D.5)

$$\dot{\lambda} = - [\dot{\sigma}_{ij} \partial f / \partial \sigma_{ij}] / [k_\beta (\partial f / \partial h_\alpha) (\partial h_\alpha / \partial \eta_\beta)]$$

whence, from Eq. (D-6)

$$\dot{D}_{ij}^P = - \{ [\dot{\sigma}_{pq} \partial f / \partial \sigma_{pq}] / [k_\beta (\partial f / \partial h_\alpha) (\partial h_\alpha / \partial \eta_\beta)] \} \partial f / \partial \sigma_{ij} \quad (D.10)$$

which is desired flow rule.

The foregoing formalism includes classical small strain, isotropic hardening plasticity as will now be shown. For small strains the symmetric part of the velocity gradient tensor is simply the strain rate, or

$$D_{ij} = \dot{\epsilon}_{ij} \quad (D.11)$$

Equation (D.3) becomes

where

$$J_2 = \sigma_o^3 / 3$$

$$2J_2 = S_{ij} S_{ij}, \quad S_{ij} = \sigma_{ij} - (\sigma_{kk}/3) \delta_{ij} \quad (D.12)$$

In Eqs. (D.12) S_{ij} is the deviatoric part of the Cauchy stress and σ_o is the material yield stress in simple tension. In the notation of Eqs. (2.10) and (D.4), only one material parameter and one effective plastic strain are employed:

$$h_1 \equiv \sigma_o = h_1(\eta_1), \quad \eta_1 \equiv \bar{\epsilon} = \int_0^t \sqrt{\frac{2}{3} \epsilon_{Dij}^P \epsilon_{Dij}^P} dt \quad (D.13)$$

where $\bar{\epsilon}^P$ is the effective plastic shear strain and

$$\dot{\epsilon}_{Dij}^P = \dot{\epsilon}_{ij}^P - (\dot{\epsilon}_{kk}^P / 3) \delta_{ij} \quad (D.14)$$

From Eqs. (D.12), (D.13) and (D.14)

$$\left. \begin{aligned} \partial h_1 / \partial \eta_1 &= \partial \sigma_o / \partial \bar{\epsilon}^P, \quad \partial f / \partial h_1 = -2\sigma_o / 3, \quad \partial f / \partial \sigma_{ij} = S_{ij} \\ \dot{\eta}_1 &= (2 \dot{\epsilon}_{Dij}^P \dot{\epsilon}_{DIJ}^P / 3)^{1/2} \end{aligned} \right\} \quad (D.15)$$

and from Eqs. (D.9), (D.15), (D.6) and (D.12)

$$k_1 = (2 S_{ij} S_{ij} / 3)^{1/2} = 2\sigma_o / 3 \quad (D.16)$$

Finally from Eqs. (D.15), (D.16) and (D.10)

$$\dot{\epsilon}_{ij}^P = - \left\{ (9 \dot{S}_{pq} S_{pq}) / [4 \sigma_o^2 d\sigma_o / d\bar{\epsilon}^P] \right\} S_{ij} \quad (D.17)$$

which is the flow rule of classical small strain isotropic hardening plasticity. To complete the theory the function h_1 in Eq. (2.20) is taken to be the function governing uniaxial stress σ and elongational plastic strain ϵ^P in a simple tension test, i.e.,

$$\sigma = h_1(\epsilon^P) \quad (D.18)$$

It is standard practice in the HIP of turbine disks to preheat the metal powder to 2000 deg F over a period of twelve hours before HIP. Thus, some sintering of particles will occur, endowing the powder aggregate with mechanical strength. Additionally, during partial HIP the powder is held at a temperature between 2000 and 2250 deg F in a partially compacted state for up to three hours. Thus, a partially dense HIP powder has both compressive and tensile strength.

Since hydrostatic compression increases interparticle contact area, a specimen of partial HIP powder (1) is stiffer in hydrostatic compression than tension, (2) has an increasing stiffness in hydrostatic compression and a fixed stiffness in hydrostatic tension, assuming no interparticle bonds are fractured. Consequently, it cannot be assumed that a partially dense HIP specimen has, like metals, the same initial yield stress in tension as in compression; this must be established by experiment.

Assume for the moment that a partially dense HIP powder has the same response in tension as in compression, and that the yield surface has no sharp corners. A simple yield function satisfying the foregoing assumptions is

$$\beta \left(\frac{I_1^2}{3} + J_2 \right) = \frac{\sigma_o^2}{3} \quad (D.19)$$

which is an ellipse in $I_1, \sqrt{J_2}$ space, (Fig. 5), with process dependent parameters β and σ_o . The surface is also plotted in principal stress space with σ_3 zero in Fig. 6. Note that as β approaches zero, the Mises yield condition is recovered. In Fig. 3 yield surface Eq. (2.23) has been plotted with the linear and parabolic Mohr-Coulomb yield surfaces for the case of β equal to one. It will be noted that Eq. (2.23) predicts a closed yield surface which is smooth where it intersects the hydrostatic axis. Also, assuming small strains and an associated flow rule, Eq. (2.23) implies that, unlike the Mohr-Coulomb theories pure shear stress induces no plastic volumetric strain (Appendix C).

A yield surface of the form Eq. (D.19) has previously been proposed by Green (Ref. 9), and Shima and Oyane (Ref. 12). Kuhn and Downey (Ref. 13) proposed a yield function of the form

$$3 J_2 - (1-2\nu_p) J_2^1 = \bar{\sigma}^2 \quad (D.20)$$

where $\bar{\sigma}$ is the uniaxial yield stress, ν_p is a plastic Poisson's Ratio which approaches 0.5 with full densification and

$$J_2^1 = 3J_2 - I_1^2.$$

Clearly in $I_1, \sqrt{J_2}$ space this also has the form of an ellipse.

If a partially dense HIP powder has differing yield stresses in tension and compression Eq. (D.19) is no longer valid. However, it can be easily modified to model this effect by having β differ in tension and compression. Alternatively, a yield function of the form

$$\beta \left(\frac{I_1}{3} - \alpha \right)^2 + J_2 = \frac{\sigma_o^2}{3} \quad (D.21)$$

can be postulated. Unlike Eq. (D.19), with β differing in tension and compression Eq. (D.21) predicts volumetric plastic strain in a state of pure shear stress; this stems from the term $-2\beta\alpha I_1/3$ in Eq. (D.21).

In this research program a yield surface must be developed to characterize the irreversible deformations that occur during the HIP process. If partially dense HIP powders have the same response in compression and tension, a yield surface of the form Eq. (D.19) or some generalization thereof should be considered. If this is not the case, then either Eq. (D.19) will be generalized or an equation of the form of Eq. (D.21) can be used. The choice of yield surface will be determined from the results of both partially dense HIP tests and mechanical tests.

In the remainder of this report Eq. (D.19) will be assumed to hold since it is the simplest representation possible for the yield surface.

Consider the two material parameters in Eq. (D.19)

$$h_1 = \beta = h_1(\eta_\beta) \quad (D.22)$$

and

$$h_2 = \tau_o = \frac{\sigma_o}{3} = h_2(\eta_\beta) \quad (D.23)$$

the yield surface is given by

$$f(\sigma_{ij}, h_\alpha) = \beta^2 \left(\frac{I_1}{3}\right)^2 + J_2 - \frac{\sigma_o^2}{3} = 0 \quad (D.24)$$

Where $I_1 = \sigma_{kk}$

$$J = 1/2 \delta_{ij} \delta_{ij}$$

$$S_{ij} = \sigma_{ij} - 1/3 \sigma_{kk} \delta_{ij}$$

σ_{ij} = Cauchy Stress

$$\beta = \beta(\eta_1, \eta_2)$$

$$\sigma_o = \sigma_o(\eta_1, \eta_2), \text{ and}$$

η_α are parameters that depend on the loading history.

Assume normality of the plastic flow in the form

$$D_{ij}^p = \dot{\lambda} \frac{\partial f}{\partial \sigma_{ij}} \quad (D.25)$$

The consistency condition requires that during plastic flow

$$\dot{f} = 0 \quad (D.26)$$

or

$$\frac{2}{9} \beta \frac{\partial \beta}{\partial \eta_\alpha} \dot{\eta}_\alpha I_1^2 + \frac{2}{9} \beta^2 I_1 \dot{I}_1 - \frac{2}{3} \sigma_o \frac{\partial \sigma_o}{\partial \eta_\alpha} \dot{\eta}_\alpha + \dot{J}_2 = 0 \quad (D.27)$$

We assume that the rates $\dot{\eta}_\alpha$ are homogeneous in D_{ij} and therefore proportional to $\dot{\lambda}$, or

$$\dot{\eta}_\alpha (D_{ij}^p) = \dot{\lambda} \dot{\eta}_\alpha \left(\frac{\partial f}{\partial \sigma_{ij}} \right) = \dot{\lambda} k_\alpha(\sigma_{ij}) \quad (D.28)$$

$$\dot{\lambda} = - \frac{\frac{2}{9} \beta^2 I_1 \dot{I}_1 + J_2}{\frac{2}{9} \beta I_1^2 \frac{\partial \beta}{\partial \eta_\alpha} k_\alpha - \frac{2\sigma_0}{3} \frac{\partial \sigma}{\partial \eta_\alpha} k_\alpha} \quad (\text{D.29})$$

APPENDIX E

HARDENING PARAMETERS AND FLOW RULE

Take as the two deformation parameters the void volume fraction and the plastic work, or

$$\eta_1 = v \quad (E.1)$$

and

$$\eta_2 = W^P = \int_0^t \sigma_{ij} D_{ij}^P dt \quad (E.2)$$

In classical volume preserving plasticity theory using either the plastic work or the effective plastic strain produces exactly the same result. The plastic work, or equivalently the inelastic energy dissipation has been used previously to describe nonlinear material response, for example, in Refs. 14 and 15.

The quantities k_α , Eq. (14) must now be determined from η_α , Parks, in Ref. 16 has shown that the void volume fraction rate from Eq. (14), can be described by considering a mass of powder m , occupying volume, V where

$$V = V_{\text{void}} + V_{\text{solid}} \quad (E.3)$$

Then the void volume fraction, v , is given by

$$v = \frac{V_{\text{void}}}{V} \quad (E.4)$$

The mass can be expressed as

$$m = \rho_v V = \rho_{\text{solid}} V_{\text{solid}} \quad (E.5)$$

Where ρ_v is the apparent density

ρ_{solid} is the density of a powder particle

Then the relative density (i.e., the bulk density to fully consolidated density ratio) is simply

$$\rho = \frac{\rho_v}{\rho_{\text{solid}}} \quad (E.6)$$

From Eqs. (E.4) and (E.5)

$$m = \rho_{\text{solid}} V(1-v) \quad (E.7)$$

Since

$$\dot{m} = 0$$

then in Eq. (E.5)

$$\dot{\rho} = -\rho D_{kk} \quad (E.8)$$

Also

$$D_{kk} = \frac{\dot{V}}{V} \quad (E.9)$$

Taking the derivative of Eq. (E.7) and using Eq. (E.8)

$$\dot{v} = (1-v) \left[D_{kk} + \frac{\dot{\rho}_{solid}}{\rho_{solid}} \right] \quad (E.10)$$

Note that

$$\frac{\dot{\rho}_{solid}}{\rho_{solid}} = -D_{kk}^{solid} \quad (E.11)$$

and assume that

$$D_{kk} = D_{kk}^p + D_{kk}^e \quad (E.12)$$

Then substituting Eqs. (E.11) and (E.12) into Eq. (E.10)

$$v = (1-v) [D_{kk}^p + (D_{kk}^e - D_{kk}^{solid})] \quad (E.13)$$

It can be demonstrated that

$$|D_{kk} - D_{kk}^{solid}| \ll |D_{kk}^p| \quad (E.14)$$

by considering a sphere of outer radius b , containing a central void of radius a . The outward elastic displacement of the outer radius of the sphere when subjected to an external hydrostatic pressure, P , and no internal pressure is given by

$$u = - \frac{(1-2\nu)Pb}{E} \left[1 + \frac{(1+\nu)\nu}{2(1-2\nu)} \right] \quad (E.15)$$

where $v = \left(\frac{a}{b}\right)^3$ is the void volume fraction

ν = Poisson's Ratio of the solid material

E = Young's Modulus of the solid material

The apparent elastic volume change per unit volume is then given by

$$\frac{\Delta V}{V} = \frac{4\pi b^2 u}{\frac{4}{3}\pi b^3} = \frac{-3(1-2\nu)P}{E} \left[1 + \frac{\nu}{2} \left(\frac{1+\nu}{1-2\nu} \right) \right] \approx D_{kk}^e \Delta t \quad (E.16)$$

The volume change of the solid particles per unit volume is

$$\frac{\Delta V}{V} = - \frac{3(1-2\nu)P}{E} \approx D_{kk}^{\text{solid}} \Delta t \quad (E.17)$$

then

$$D_{kk}^e - D_{kk}^{\text{solid}} = \left[\frac{1 - D_{kk}^{\text{solid}} \Delta t}{D_{kk}^e \Delta t} \right] D_{kk}^e \quad (E.18)$$

Substituting Eqs. (E.16) and (E.17) into Eq. (E.18)

$$D_{kk}^e - D_{kk}^{\text{solid}} = \left[\frac{\left(1 - 2\nu + \frac{1+\nu}{2} \right) \nu}{1 - 2\nu + \left(\frac{1+\nu}{2} \right) \nu} \right] D_{kk}^e \quad (E.19)$$

The term in the brackets is proportional to the void volume fraction and varies between zero and one. Therefore, for porous metal subjected to a hydrostatic pressure

$$\int_0^t (D_{kk}^e - D_{kk}^{\text{solid}}) dt \approx \frac{\nu P}{K} \quad (E.20)$$

where $K = \frac{E}{3(1-2\nu)}$ is the bulk modulus

The plastic part is

$$\int_0^t D_{kk}^p \approx \nu \quad (E.21)$$

For a pressure of 15 ksi, and a bulk modulus of 25×10^6 ksi. The ratio of the integrals in Eqs. (E.20) and (E.21) is about 0.0006 and therefore the error introduced by neglecting $D_{kk}^e - D_{kk}^s$ with respect to D_{kk}^p should be less than one-tenth of one percent.

Therefore assuming that

$$D_{kk}^e \approx D_{kk}^{\text{solid}} \quad (\text{E.22})$$

Eq. (E.13) becomes

$$\dot{\eta}_1 = \dot{v} = (1-\nu) D_{kk} = \dot{\lambda} k_1 \quad (\text{E.23})$$

Applying the normality condition, Eq. (14)

$$\dot{\eta}_1 = \dot{v} = \dot{\lambda} (1-\nu) \frac{2}{3} \beta^2 I_1 \quad (\text{E.24})$$

and therefore

$$k_1 = \frac{2}{3} (1-\nu) \beta^2 I_1 \quad (\text{E.25})$$

The second deformation measure, plastic work rate, \dot{W}^p , is simply given by

$$\dot{\eta}_2 = \dot{W}^p = \sigma_{ij} D_{ij}^p = \dot{\lambda} k \quad (\text{E.26})$$

and from Eq. (14) $\dot{\eta}_2 = \dot{W}^p = \dot{\lambda} \left(\frac{2}{3} \sigma_o^2 \right)$

$$k_2 = \frac{2}{3} \sigma_o^2 \quad (\text{E.27})$$

Substituting Eq. (E.26) and Eq. (E.27) into Eq. (15) will give the plastic part of the velocity gradient tensor from Eq. (11) as

$$D_{ij}^p = - \left(\frac{\frac{2}{9} \beta^2 \dot{I}_1 + \dot{J}_2}{H} \right) \left(\frac{2}{9} \beta^2 I_1 \delta_{ij} + s_{ij} \right) \quad (\text{E.28})$$

Where

$$H = \frac{2}{9} \beta I_1^2 \left[\frac{2}{3} (1-\nu) \beta^2 I_1 \frac{\partial \beta}{\partial \nu} + \frac{2}{3} \sigma_o^2 \frac{\partial \beta}{\partial W^p} \right] - \frac{2}{3} \sigma_o \left[\frac{2}{3} (1-\nu) \beta^2 I_1 \frac{\partial \sigma_o}{\partial \nu} + \frac{2}{3} \sigma_o^2 \frac{\partial \sigma_o}{\partial W^p} \right] \quad (E.29)$$

Equation (E.28) can be written equivalently as

$$D_{ij}^p = - \frac{ \left(\frac{2}{9} \beta^2 \sigma_{kk} \delta_{ij} + s_{ij} \right) \left(\frac{2}{9} \beta^2 \delta_{kl} + s_{kl} \right) \dot{\sigma}_{kl}}{H} \quad (E.30)$$

For an isotropic material the elastic part of the velocity gradient tensor is given by

$$D_{ij}^e = \frac{1}{E} [(1+\nu) \dot{\sigma}_{ij} - \nu \dot{\sigma}_{kk} \delta_{ij}] \quad (E.31)$$

or

$$D_{ij}^e = \frac{1}{E} \left[\frac{(1+\nu)}{2} (\delta_{ik} \delta_{jl} + \delta_{il} \delta_{jk}) - \nu \delta_{ij} \delta_{kl} \right] \dot{\sigma}_{kl} \quad (E.32)$$

Combining Eqs. (E.29) and (E.30) gives the elastic plastic constitutive law for small deformations as

$$D_{ij} = C_{ijkl}^{e-p} \dot{\sigma}_{kl} \quad (E.33)$$

where

$$C_{ijkl}^{e-p} = \frac{1}{E} \left[\frac{(1+\nu)}{2} (\delta_{ik} \delta_{jl} + \delta_{il} \delta_{jk}) - \nu \delta_{ij} \delta_{kl} \right] - \frac{1}{H} \left[\frac{2}{9} \beta^2 \sigma_{kk} \delta_{ij} + s_{ij} \right] \left[\frac{2}{9} \beta^2 \delta_{kl} + s_{kl} \right] \quad (E.34)$$

APPENDIX F

ELASTIC-PLASTIC SMALL STRAIN MODULI FOR VOLUME PRESERVING PLASTICITY WITH ISOTROPIC HARDENING

In nonlinear stress analysis it is desirable to develop a constitutive relation describing stress increments in terms of strain increments or

$$\Delta \sigma_{ij} = L_{ijkl}^{e-p} \Delta \epsilon_{kl} \quad (F.1)$$

where L_{ijkl}^{e-p} are the small strain elastic-plastic moduli.

Consider a yield surface given by

$$f(\sigma_{ij}, h_\alpha) = J_2 - \frac{\sigma_o^2}{3} = 0 \quad (F.2)$$

where

$$\begin{aligned} J_2 &= \frac{1}{2} S_{ij} S_{ij} \\ S_{ij} &= \sigma_{ij} - \frac{1}{3} \delta_{ij} \sigma_{kk}, \\ h_i &= \sigma_o(\bar{\epsilon}^p), \text{ and} \\ \bar{\epsilon}^p &= \sqrt{\frac{2}{3} \dot{\epsilon}_{ij}^p \dot{\epsilon}_{ij}^p} \text{ is the effective plastic strain} \end{aligned} \quad (F.3)$$

Decomposing the strain rates into elastic and plastic parts

$$\dot{\epsilon}_{ij} = \dot{\epsilon}_{ij}^e + \dot{\epsilon}_{ij}^p \quad (F.4)$$

and applying an associated flow rule

$$\dot{\epsilon}_{ij}^p = \dot{\lambda} \frac{\partial f}{\partial \sigma_{ij}} = \dot{\lambda} S_{ij} \quad (F.5)$$

The elastic part of the strain is simply given by Hookes law or

$$\dot{\epsilon}_{ij}^e = \frac{1+\nu}{E} \sigma_{ij} - \frac{\nu}{E} \sigma_{kk} \delta_{ij} \quad (F.6)$$

Substituting Eqs. (F.5) and (F.6) into Eq. (F.4)

$$\dot{\epsilon}_{ij} = \frac{1+\nu}{E} \dot{\sigma}_{ij} - \frac{\nu}{E} \sigma_{kk} \delta_{ij} + \dot{\lambda} S_{ij} \quad (F.7)$$

We require for consistency that

$$f = 0$$

or

$$S_{ij} \dot{\sigma}_{ij} - \frac{2}{3} \sigma_o \frac{d\sigma_o}{d\bar{\epsilon}^p} \bar{\epsilon}^p = 0 \quad (F.8)$$

Using the associated flow rule, Eq. (F.5) in Eq. (F.8)

$$S_{ij} \dot{\sigma}_{ij} - \left(\frac{2}{3}\right)^2 \sigma_o^2 \frac{d\sigma_o}{d\bar{\epsilon}^p} \dot{\lambda} = 0 \quad (F.9)$$

Constraining Eq. (D.7) by premultiplying by S_{ij} and taking note of Eq. (F.9)

$$\dot{\lambda} = \frac{3 S_{ij} \dot{\sigma}_{ij}}{2 \sigma_o^2 \left[1 + \frac{2(1+\nu)}{3E} \frac{d\sigma_o}{d\bar{\epsilon}^p} \right]} \quad (F.10)$$

Substituting Eq. (F.10) into Eq. (F.7)

$$\left[\delta_{ij} \delta_{jl} - \frac{3 S_{ij} S_{kl}}{2 \sigma_o^2 \left(1 + \frac{2(1+\nu)}{3E} \frac{d\sigma_o}{d\bar{\epsilon}^p} \right)} \right] \dot{\epsilon}_{kl} = \frac{1+\nu}{E} \dot{\sigma}_{ij} - \frac{\nu}{E} \sigma_{kk} \delta_{ij}$$

which can be shown to result in

$$\dot{\sigma}_{ij} = \frac{E}{1+\nu} \left[\delta_{ik} \delta_{jl} + \frac{\nu}{1-2\nu} \delta_{ij} \delta_{kl} - \frac{3 S_{ij} S_{kl}}{2 \sigma_o^2 \left(1 + \frac{2(1+\nu)}{3E} \frac{d\sigma_o}{d\bar{\epsilon}^p} \right)} \right] \epsilon_{kl} \quad (F.11)$$

Comparing Eq. (F.1) and (F.11)

$$L_{ijk1}^{e-p} = \frac{E}{1+\nu} \left[\delta_{ik} \delta_{jl} + \frac{\nu}{1-2\nu} \delta_{ij} \delta_{kl} - \frac{3 S_{ij} S_{kl}}{2 \sigma_o^2 \left(1 + \frac{2(1+\nu)}{3E} \frac{d\sigma_o}{d\bar{\epsilon}^p} \right)} \right] \quad (F.12)$$

APPENDIX G

RIGID SPHERICAL INCLUSIONS

Consider the validation experiment consisting of a rigid spherical inclusion in a powder metal of infinite extent. The final density after a partial HIP, at each radial location in the powder metal, will be determined by the stress history at each point in the powder metal. Assume that the powder metal is an isotropic homogeneous elastic material. The stress distribution can be found by applying the classical equations of elasticity.

In spherical coordinates for spherically symmetric problems (Ref. 34), the strain displacement relations, for small strain elasticity, are:

$$e_r = \frac{du}{dr} \quad (G.1)$$

$$e_\theta = e_\phi = \frac{u}{r} \quad (G.2)$$

where u is the radial displacement.

The remaining equilibrium equation is:

$$\frac{1}{r^2} \frac{d}{dr} (r^2 \sigma_r) - \frac{\sigma_\theta + \sigma_\phi}{r} = 0 \quad (G.3)$$

where $\sigma_\theta = \sigma_\phi$, and no body forces are present.

For an isotropic, homogeneous, elastic solid only two material parameters are required which are constants throughout the body. Under this condition the stresses as a function of the radial displacement are given by:

$$\sigma_r = \frac{E}{(1+\nu)(1-2\nu)} \left[(1-\nu) \frac{du}{dr} + 2\nu \frac{u}{r} \right], \text{ and} \quad (G.4)$$

$$\sigma_\theta = \sigma_\phi = \frac{E}{(1+\nu)(1-2\nu)} \left[\nu \frac{du}{dr} + \frac{u}{r} \right], \quad (G.5)$$

where E is Young's modulus, and ν is Poisson's ratio.

Substituting Eqs. (G.4) and (G.5) into the equilibrium equation results in

$$\frac{d^2 u}{dr^2} + \frac{2}{r} \frac{du}{dr} - \frac{2}{r^2} u = 0. \quad (G.6)$$

The solution to Eq. (G.6) is:

$$u = C_1 r + C_2 / r^2, \quad (G.7)$$

where C_1 and C_2 are arbitrary constants. The boundary conditions are:

$$u = 0 \text{ at } r = a, \text{ and} \quad (G.8)$$

$$\sigma_r \rightarrow -P \text{ as } r \rightarrow \infty, \quad (G.9)$$

where a is the outer radius of the inclusion, and p is the external applied pressure. Substituting conditions (G.8) and (G.9) into Eq. (G.7) specifies the two arbitrary constants and results in

$$\sigma_r = -P \left[1 + 2(1-2\nu) \left(\frac{a}{r} \right)^3 \right] \quad (G.10)$$

$$\sigma_\theta = \sigma_\phi = -P \left[1 - (1-2\nu) \left(\frac{a}{r} \right)^3 \right] \quad (G.11)$$

The first invariant of the stress is a constant and is given by

$$I_1 = -3P \quad (G.12)$$

and the second invariant of the deviatoric stress tensor is

$$\sqrt{J_2} = \sqrt{3} (1-2\nu) P \left(\frac{a}{r} \right)^3 \quad (G.13)$$

APPENDIX H

RIGID CYLINDRICAL INCLUSIONS

Consider the validation experiment consisting of a rigid cylindrical inclusion in a powder metal of infinite extent. The final density after a partial HIP, at each radial location in the powder metal will be determined by the stress history at each point in the powder metal. Assume that the powder metal is an isotropic, homogeneous elastic material, sufficiently far from the ends, near the inclusion a plane strain situation will result. The stress distribution can be found by applying the classical equations of elasticity.

In cylindrical coordinates for plane strain axisymmetric problems

$$w = v = 0$$

where w is the axial or z displacement, and v is the circumferential or θ displacement. The strain displacement equations, from Ref. 35, are:

$$e_{\theta} = \frac{u}{r} \quad (H.1)$$

$$e_r = \frac{du}{dr} \quad (H.2)$$

where u is the radial displacement. The remaining equilibrium equation is

$$\frac{1}{r} \frac{d}{dr} (r \sigma_r) - \frac{\sigma_{\theta}}{r} = 0 \quad (H.3)$$

For an isotropic, homogeneous, elastic solid only two material parameters are required which are constants throughout the body. Under this condition the stress as a function of the radial displacement is given by:

$$\sigma_r = \frac{E}{(1+\nu)(1-2\nu)} \left[(1-\nu) \frac{du}{dr} + \nu \frac{u}{r} \right], \quad (H.4)$$

$$\sigma_{\theta} = \frac{E}{(1+\nu)(1-2\nu)} \left[\nu \frac{du}{dr} + (1-\nu) \frac{u}{r} \right], \text{ and} \quad (H.5)$$

$$\sigma_z = \nu(\sigma_r + \sigma_{\theta}) \quad (H.6)$$

where E is Young's modulus, and ν is Poisson's ratio. Substituting Eqs. (H.4) and (H.5) into the equilibrium equation results in

$$\frac{d^2 u}{dr^2} + \frac{1}{r} \frac{du}{dr} - \frac{1}{r^2} u = 0. \quad (\text{H.7})$$

The solution to Eq. (H.7) is

$$u = C_1 r + \frac{C_2}{r} \quad (\text{H.8})$$

where C_1 and C_2 are arbitrary constants. The boundary conditions are:

$$u = 0 \text{ at } r = a, \text{ and} \quad (\text{H.9})$$

$$\sigma_r = -P \text{ as } r \rightarrow \infty, \quad (\text{H.10})$$

where a is the outer radius of the inclusion, and P is the external applied pressure. Substituting conditions (H.9) and (H.10) into Eq. (H.8) specifies the two arbitrary constants and results in

$$\sigma_r = -P \left[1 + \frac{(1-2\nu)a^2}{r^2} \right] \quad (\text{H.11})$$

$$\sigma_\theta = -P \left[1 - \frac{(1-2\nu)a^2}{r^2} \right] \quad (\text{H.12})$$

$$\sigma_z = -2\nu P \quad (\text{H.13})$$

The first invariant of the stress tensor is given by

$$I_1 = -2(1+\nu)P \quad (\text{H.14})$$

and the second invariant of the deviatoric stress tensor is

$$\sqrt{J_2} = (1-2\nu)P \sqrt{\frac{1}{3} + \left(\frac{a}{r}\right)^4} \quad (\text{H.15})$$

APPENDIX I

THERMAL CONDUCTIVITY EFFECTS

Consider a long cylinder filled with powder metal. It is desirable to know the temperature distribution in the powder metal in order to estimate the variation in mechanical properties due to their temperature dependence. The heat transfer due to thermal conductivity will be governed by the well known Fourier heat conduction equation below:

$$K \nabla^2 T = \rho c \frac{\partial T}{\partial t}, \quad (I.1)$$

where T is the temperature,
 K is the thermal conductivity,
 ρ is the density,
 c is the specific heat,
 t is time, and

$\nabla^2 T = \frac{1}{r} \frac{\partial}{\partial r} \left(r \frac{\partial T}{\partial r} \right)$ for axisymmetric conditions. Assume that at the outer surface (i.e., at $r=a$) the temperature is rising linearly with respect to time, or

$$T = \dot{T}_0 t \quad (I.2)$$

where T_0 is a constant. Equations (I.5) and (I.2) imply, that for a constantly rising condition

$$T = R(r) + \dot{T}_0 t \quad (I.3)$$

Substituting Eq. (I.3) into Eq. (I.1) and (I.2) results in

$$\frac{K}{r} \frac{d}{dr} \left(r \frac{dR}{dr} \right) = \rho c \dot{T}_0 \quad (I.4)$$

and

$$\begin{aligned} R &= 0 \text{ at} \\ r &= a \end{aligned} \quad (I.5)$$

The solution to Eq. (I.4) is

$$R = C_1 + C_2 \ln(r) + \rho \frac{c \dot{T}_0 r^2}{4K} \quad (I.6)$$

The temperature is finite at the center (i.e., at r equals 0) and therefore C_2 is zero. Equation (I.5) specifies C_1 , giving for the steady temperature

$$T(r,t) = \dot{T}_o t - \rho \frac{c \dot{T}_o a^2}{4K} \left[1 - \left(\frac{r}{a} \right)^2 \right] \quad (I.7)$$

The steady temperature difference between the outer surface and center of the cylinder

$$\Delta T = T(a,t) - T(0,t) = \rho \frac{c \dot{T}_o a^2}{4K} \quad (I.8)$$

As an application of Eq. (I.8) consider a metal whose properties are

$$\rho = 0.287 \text{ lb/in.}^3,$$

$$c = 0.14 \text{ Btu/lb/F, and}$$

$$K = 195 \text{ Btu-in./ft}^2/\text{F}.$$

For a powder of this metal with a 30 percent volume void fraction the thermal conductivity is reduced by the small contact area of the particles. Assuming the reduction in contact area and the radiation transfer across the voids combine to reduce the thermal conductivity to 1/20 of the above value, the steady temperature difference is approximately 50 F for an outer radius of 1.5 in. and the outer temperature rising at 200 F/hr.

For the fully densified powder metal the temperature decrease would be approximately 3 F. The actual temperature difference would lie between these two extremes during the HIP process, with the temperature difference decreasing as the powder metal compacts.

TABLE 1

TASKS AND SUBTASKS FOR MODELING THE HOT ISOSTATIC
PRESSING PROCESS

Task 1:	Constitutive Model Development
1.1	Yield Surface Determination
1.2	Deformation and Time Hardening
1.3	Flow Rule Development
1.4	Creep Effects

Task 2:	Code Modifications
2.1	Code Familiarization
2.2	Numerical Strategy Definition
2.3	Code Modifications
2.4	Code Modification Verification

Task 3:	Material Properties Determination
3.1	Partial HIP Experiments
3.2	Mechanical Tests
3.2.1	Elevated Temperature Compression Testing
3.2.2	Elevated Temperature Tension Testing
3.2.3	Creep Testing

Task 4:	Constitutive Theory Verification
4.1	Verification Design and Analysis
4.2	Verification Experiment
4.3	Correlation

Task 5:	HIP Process Sensitivity Study
Annual Report	
Final Report	

TABLE 2

VALUES OF $f(x)$, Eq. (63)

x	$f(x)$
0.00	0.000
0.50	0.051
0.10	0.103
0.15	0.156
0.20	0.211
0.25	0.268
0.30	0.326
0.35	0.387
0.40	0.449
0.45	0.514
0.50	0.582

x	$f(x)$
0.50	0.582
0.55	0.653
0.60	0.728
0.65	0.806
0.70	0.889
0.75	0.979
0.80	1.075
0.85	1.181
0.90	1.300
0.95	1.441
1.00	1.645

TABLE 3

POTENTIAL STRUCTURAL ANALYSIS CODES

Code Name	Author	Analysis Capabilities					
		Static	Plastic	Creep	Axisymmetric Continuum	Axisymmetric Shell	Large Strain Updated Lagrangian
ADINA	Bathe	Yes	Yes	Yes	Yes	Yes	No
HONDO	Key	No	Yes	Yes	Yes	No	Yes
FIPAX	Osias	Yes	Yes	No	Yes	No	Yes
PLANS	Armen	Yes	Yes	Yes	Yes	No	No
MARC	MARC Corporation	Yes	Yes	Yes	Yes	Yes	Yes
ANSYS	Swanson Analysis Systems, Inc.	Yes	Yes	Yes	Yes	Yes	No
NON-NISA	Engineering Mechanics Research Corporation	Yes	Yes	No	Yes	No	*
NEPSAP	Lockheed	Yes	Yes	Yes	Yes	Yes	*

*Total Lagrangian Formulation

TABLE 4
Test Conditions for
Partial HIP Experiments

All specimens preheated for 12 hrs at 2000 F and 1 atm

Exp. No.	Specimen No.	Conditions			Final Relative Density
		Temp., F	Time, min.	Pressure, ksi	
1	-	2135	20	5	1.000
2	-	2135	10	2.5	0.994
3	-	2135	10	1	1.000
4	-	1800	10	1	0.746
5	-	1600	10	15	0.706
6	-	1600	10	1	0.719
7	1002,03	1800	10	4	0.794,0.798
8	1004,05	2000	10	15	0.990,0.984
9	1006,07	1800	10	8	0.891,0.822
10	1008,09	1800	10	6	0.809,0.861
11	1010,11	1800	10	10	0.902,0.909
12	1012,NG	2000	10	4	0.984,leaked
13	1017,18	1800	10	15	0.863,0.922
14	1019,20	2000	10	2	0.852,0.934
15	1021,NG	2000	10	4	0.955,leaked
16	1031,32	2000	10	3	0.819,0.949
17	1043,44	1900	10	4	0.894,0.905
18	1059,60	1800	60	4	0.887,0.933
19	1061,62	1600	10	10	0.758,0.743
20	1067,68	1600	10	8	0.756,0.756
21	1068,70	1900	10	2	0.767,0.832
22	1071,72	1800	30	8	0.912,0.817
23	1073,74	1800	30	4	0.881,0.883
24	1089,90	1600	60	10	0.806,0.812
25	1091,92	1600	60	8	0.800,0.763
26	1098,99	1800	120	4	0.900,leaked
27	1100,01	1600	120	8	0.765,0.811
28	1102,0	1800	240	4	0.881,0.963
29	1106,07	2000	30	2	1.000,0.936
30	1108,09	2000	60	2	1.000,1.000
-	NG,NG	1600	10	15	both leaked
-	NG,NG	1600	10	15	both leaked
-	NG,NG	1600	120	8	both leaked
-	Sintered Only	-	-	-	0.707,0.686, 0.705

TABLE 5

RESULTS OF COMPRESSION TESTS

Specimen No.	HIP Conditions			Geometry			
	Maximum Pressure, ksi	Temp., F	Time at Max., Min.	Initial		Final	
				Height, in.	Dia., in.	Height, in.	Dia., in.
1002	4	1800	10	0.503	0.202	0.438	0.215, 0.210
1004	15	2000	10	0.502	0.204	0.475	0.212
1006	8	1800	10	0.5025	0.204	0.475	0.208
1009	6	1800	10	0.503	0.204	0.477	0.210
1011	10	1800	10	0.502	0.2045	0.478	0.209
1018	15	1800	10	0.503	0.2045	0.4595	0.212
1020	2	2000	10	0.503	0.2025	0.466	0.210
1021	4	2000	10	0.5025	0.204	0.469	0.212
1032	3	2000	10	0.503	0.203	-	-
1044	4	1800	10	0.503	0.2025	0.473	0.208
1060	4	1800	60	0.502	0.203	0.454	0.214
1061	10	1600	10	0.503	0.200	0.475	0.205
1067	8	1600	10	0.503	0.199	0.485	0.203
1071	8	1800	30	0.502	0.203	0.475	0.210
1074	4	1800	30	0.502	0.203	0.478	0.209
							0.986, 0.941
							1.021
							0.982
							1.005
							0.995
							0.984
							0.996
							1.008
							-
							0.992
							1.005
							0.992
							1.003
							1.012
							1.009

AD-A078 162

UNITED TECHNOLOGIES RESEARCH CENTER EAST HARTFORD CONN
MODELING OF THE HOT ISOSTATIC PRESSING PROCESS.(U)
SEP 79 B N CASSENTI , K J CHEVERTON

F/6 13/8

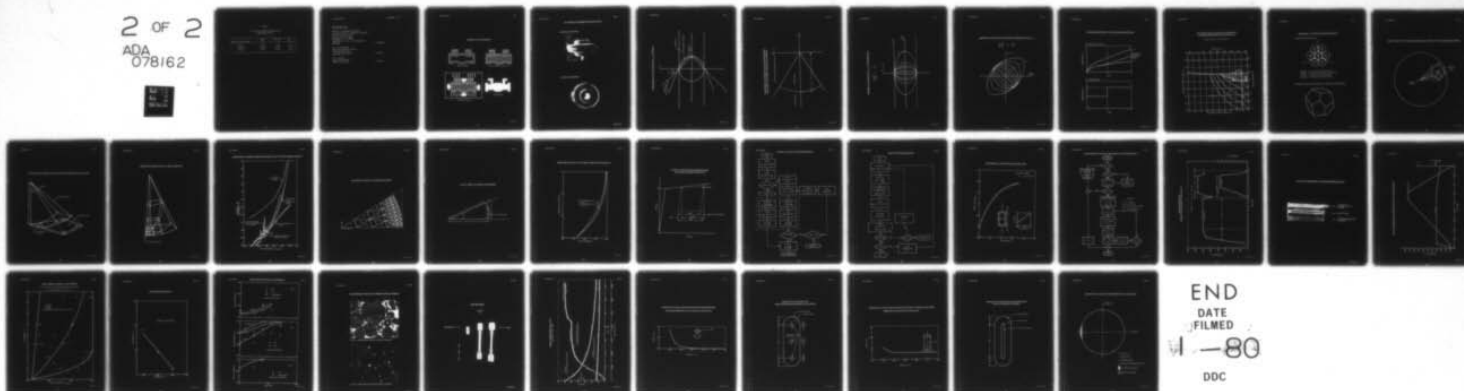
F49620-78-C-0090

UNCLASSIFIED

AFOSR-TR-79-1236

NL

2 OF 2
ADA
078162



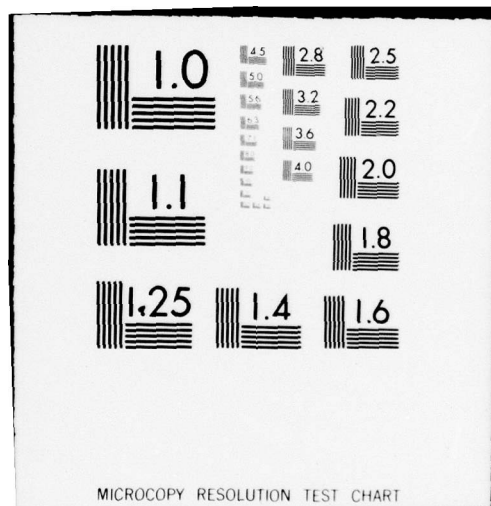


TABLE 6

STATISTICAL GEOMETRY CHANGES FOR
COMPRESSION TESTS

Ratio, Final/Initial	Mean m	Std. Dev. s	$\frac{m-1}{s}$
Height	0.9345	0.029	-2.25
Diameter	1.0330	0.010	3.31
Volume	0.9975	0.015	-0.17

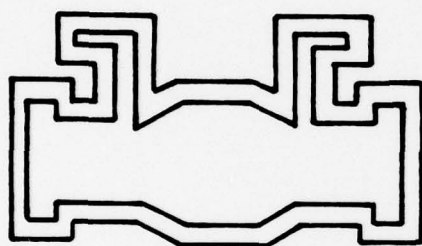
DISTRIBUTION LIST

Director of Aerospace Sciences
Air Force Office of Scientific Research
United States Air Force
Bolling Air Force Base
Washington, D. C. 20332
Attention: Lt. Co. J. D. Morgan III
AFOSR/NA (6 copies)

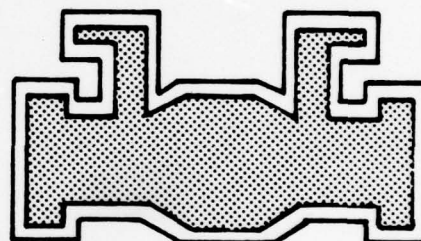
Dr. R. Dreschfield
NASA Lewis Research Center
2100 Brookpark Road
Cleveland, Ohio 44135 (1 copy)

Dr. H. Gegel
Mail Stop AFML/LLM
WLPafb, Ohio 45433 (1 copy)

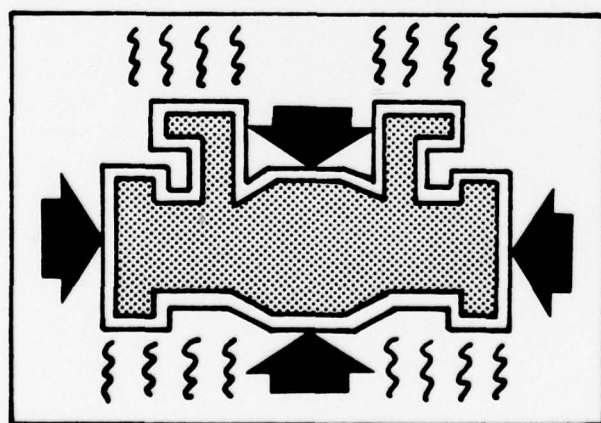
SCHEMATIC OF HIP PROCESS



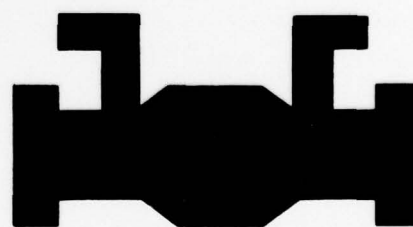
FABRICATED MOLD



FILL WITH POWDER, EVACUATE



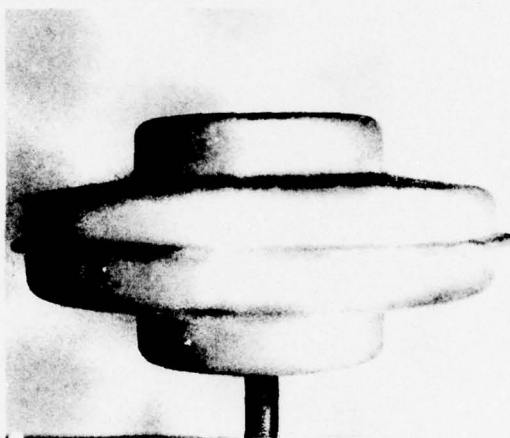
HOT ISOSTATIC PRESS



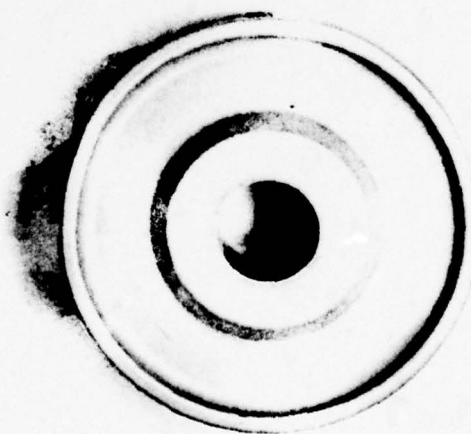
FINISHED PART

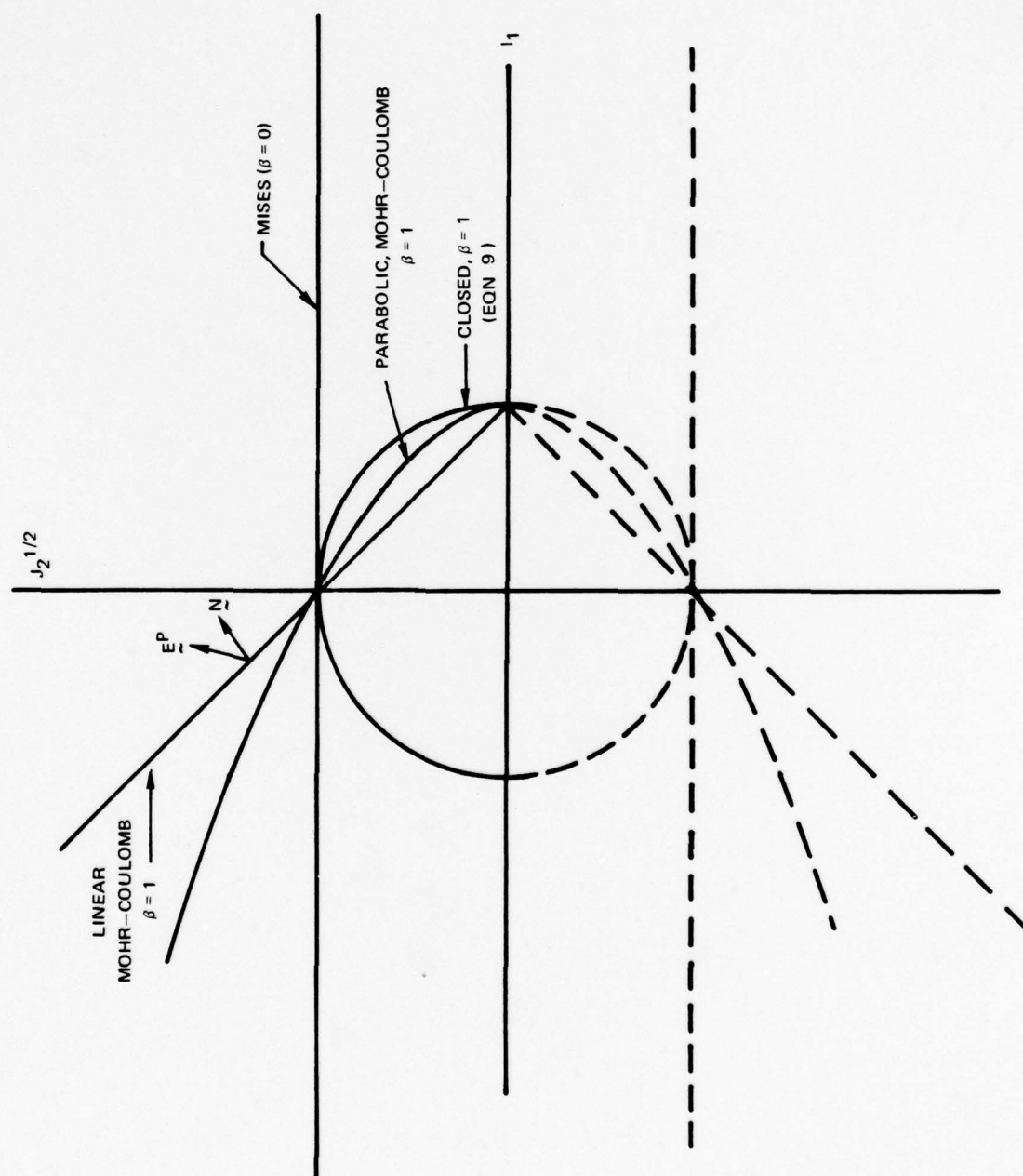
HOT ISOSTATIC PRESSING CONFIGURATIONS

(a) SAMPLE HIP CONTAINER

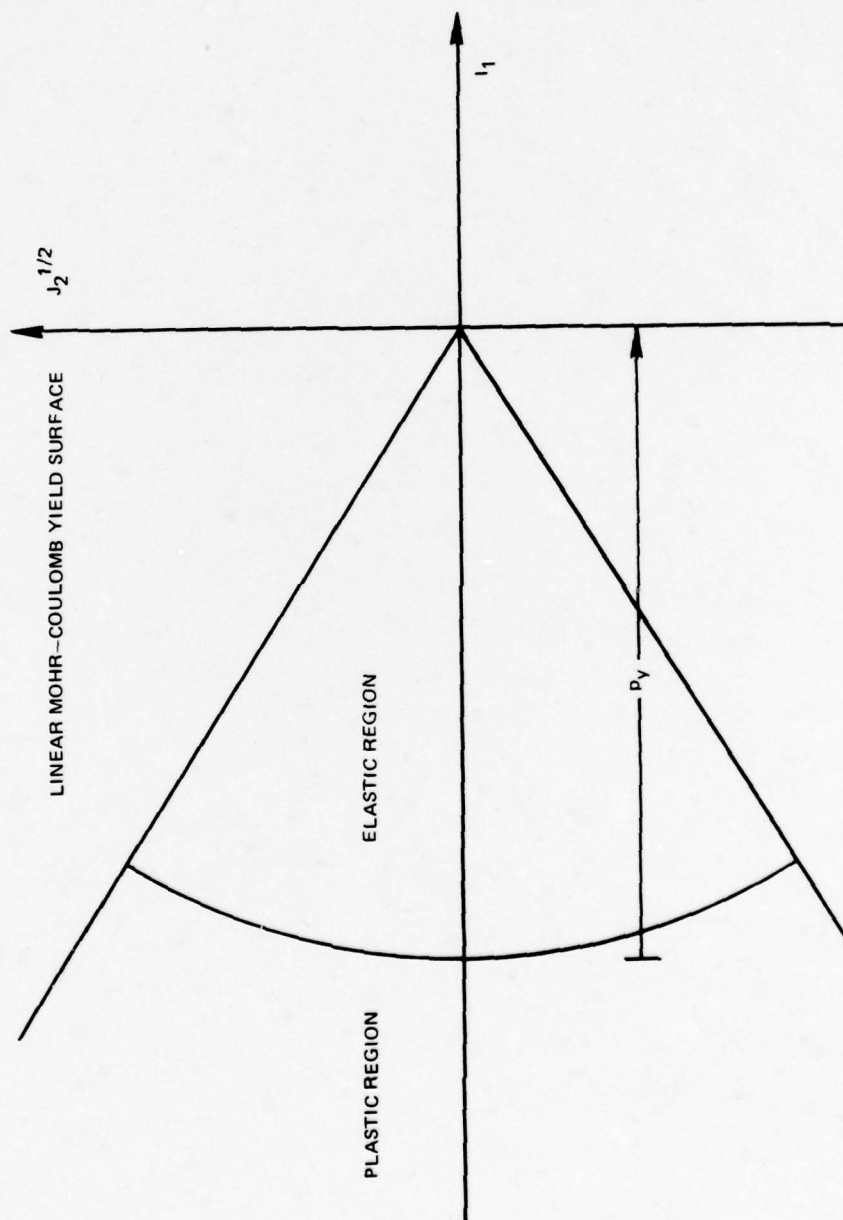


(b) RESULTING GEOMETRY



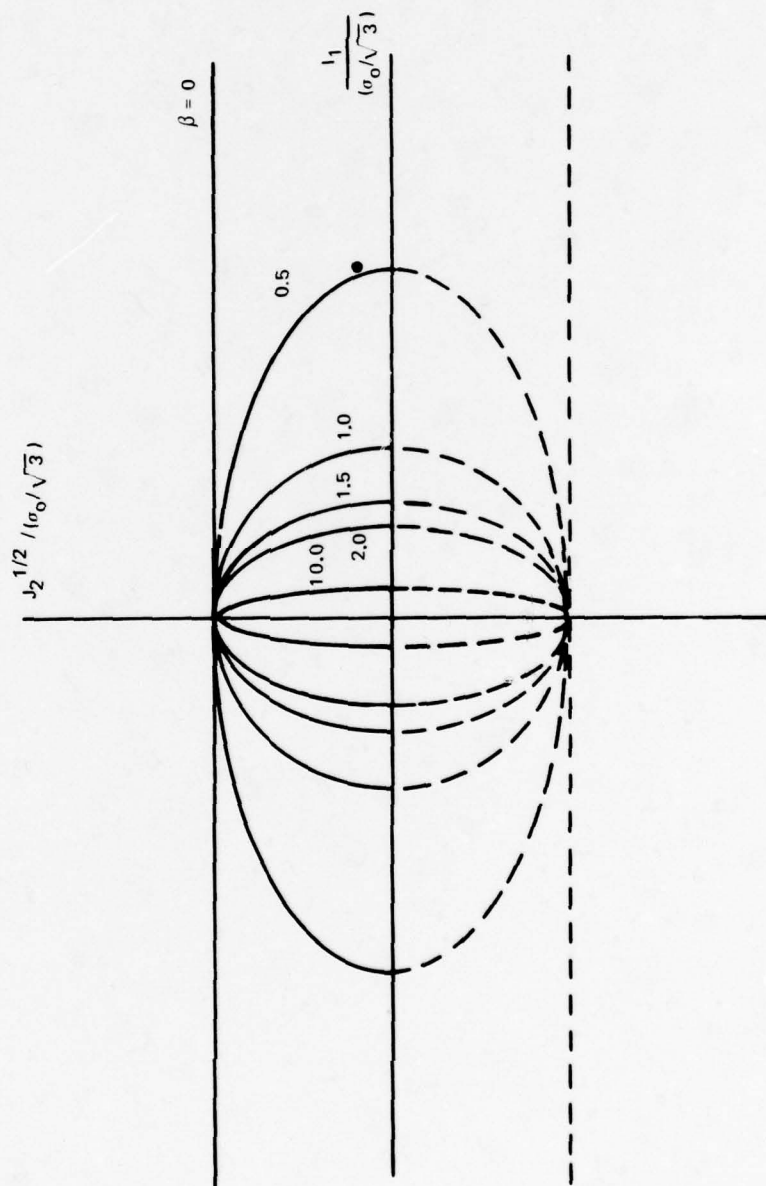
COMPARISON OF YIELD SURFACES IN $I_1, J_2^{1/2}$ SPACE

LINEAR MOHR-COULOMB YIELD ENVELOPE MODIFIED
TO INCLUDE YIELD UNDER HYDROSTATIC PRESSURE



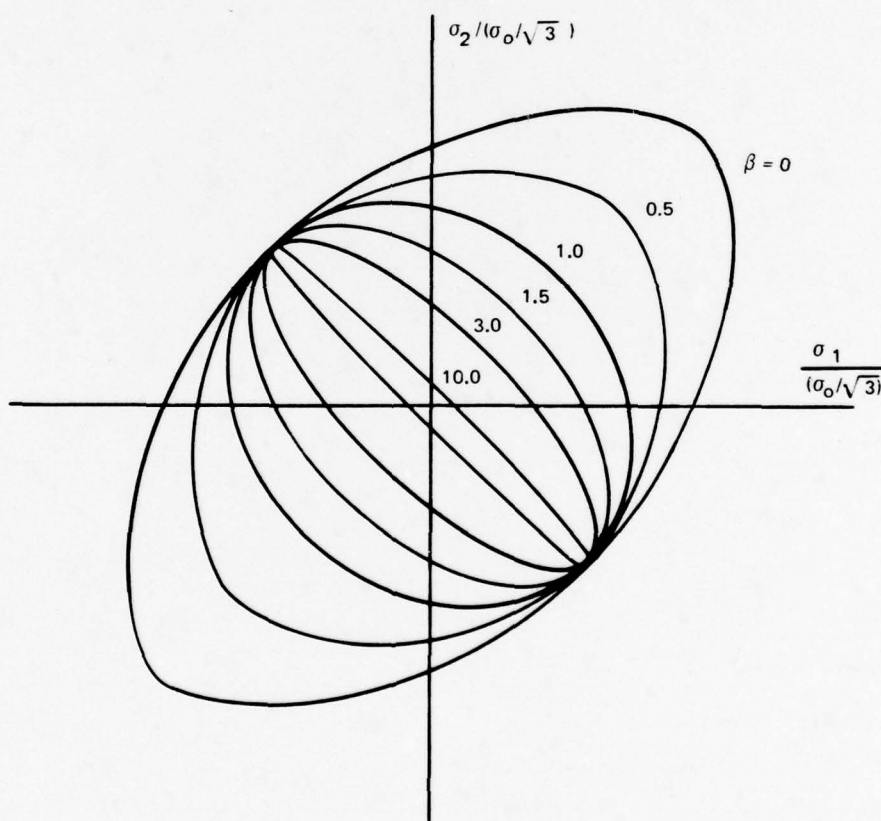
ASSUMED YIELD SURFACE IN $I_1, J_2^{1/2}$ STRESS SPACE

$$\beta \left(\frac{I_1}{3} \right)^2 + J_2 = \frac{\sigma_0^2}{3}$$

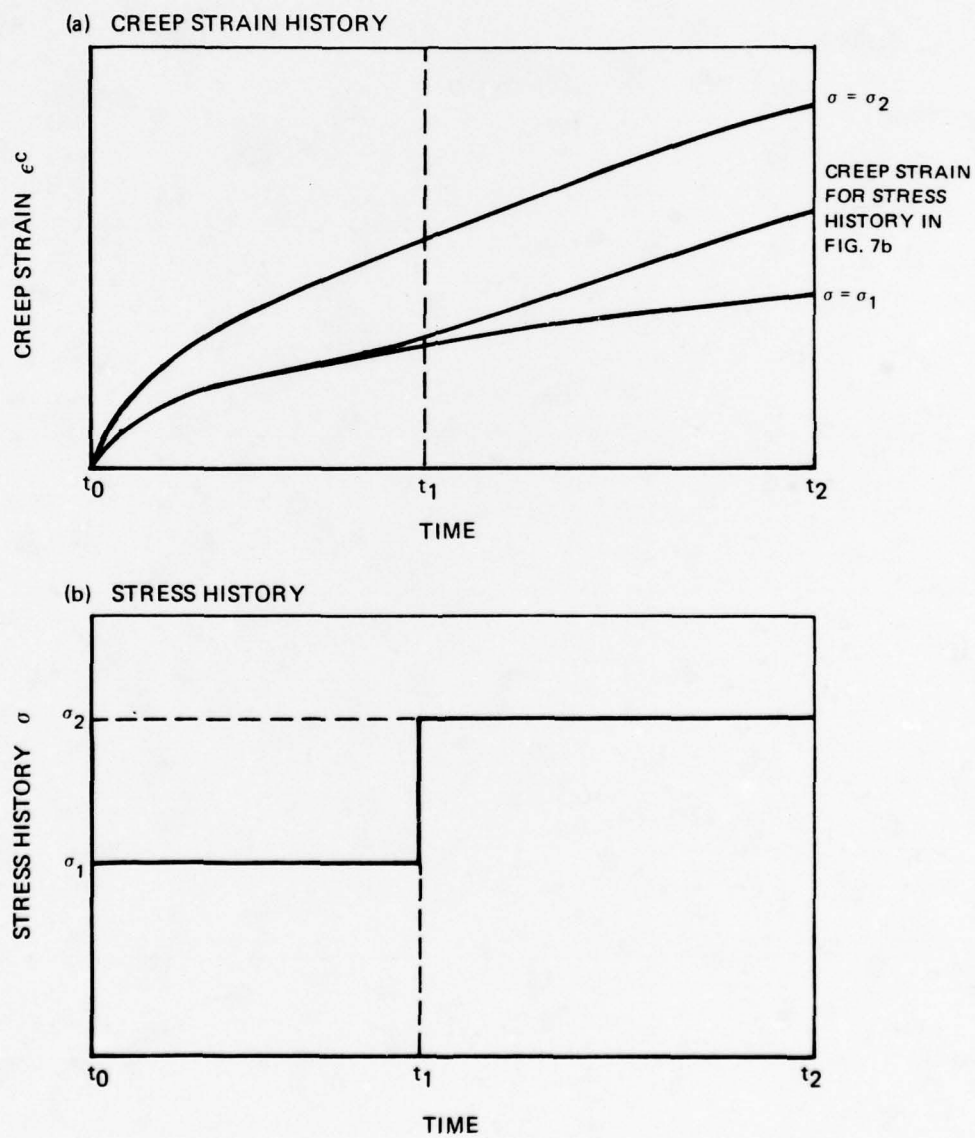


ASSUMED YIELD SURFACE IN PRINCIPAL STRESS SPACE FOR $\sigma_3 = 0$

$$\beta \left(\frac{I_1}{3} \right)^2 + J_2 = \frac{\sigma_o^2}{3}$$

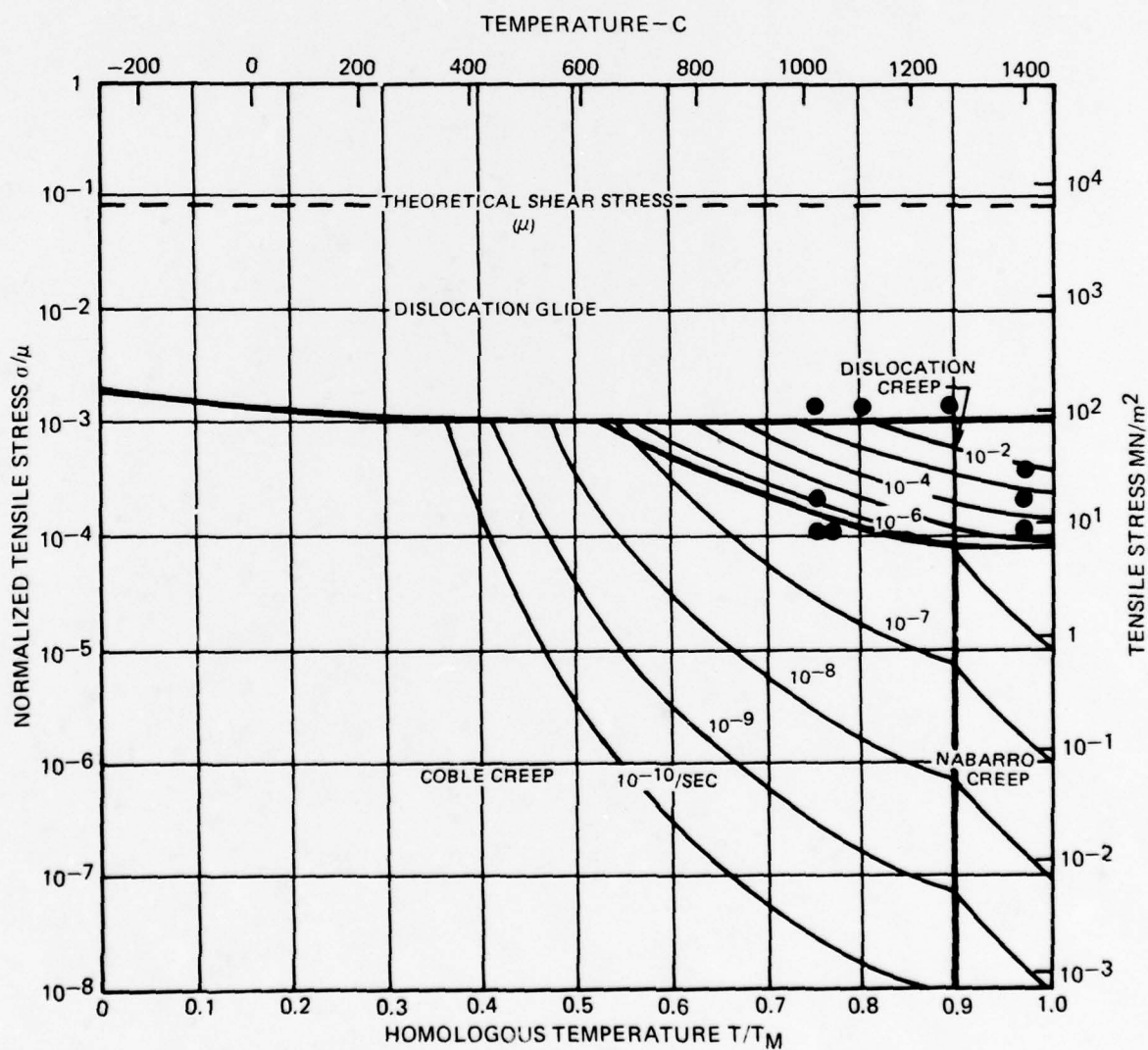


TIME HARDENING MODEL OF CREEP STRAIN PREDICTION



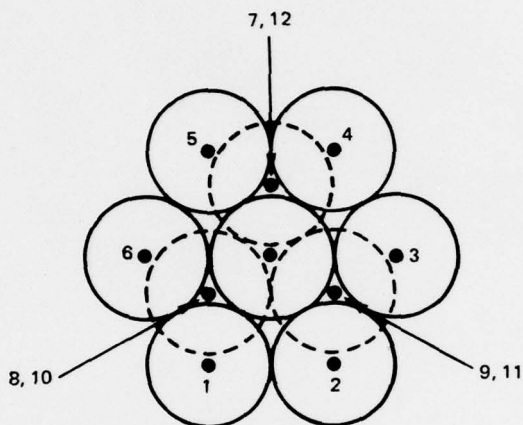
LOCATION OF MERL 76 PARTIAL HIP CONDITIONS ON CREEP DEFORMATION MAP FOR NICKEL

● MERL 76 PARTIAL HIP EXPERIMENTS



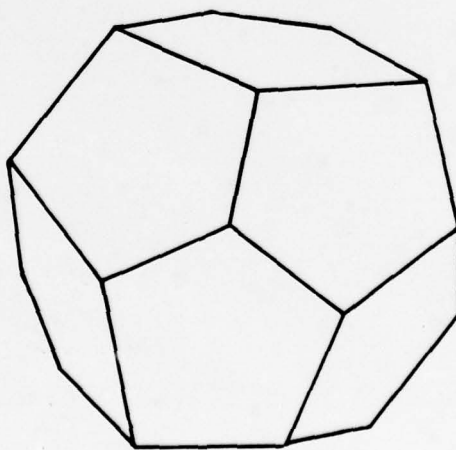
HEXAGONALLY CLOSE PACKED SPHERES MODEL

(a) GEOMETRIC CONFIGURATION

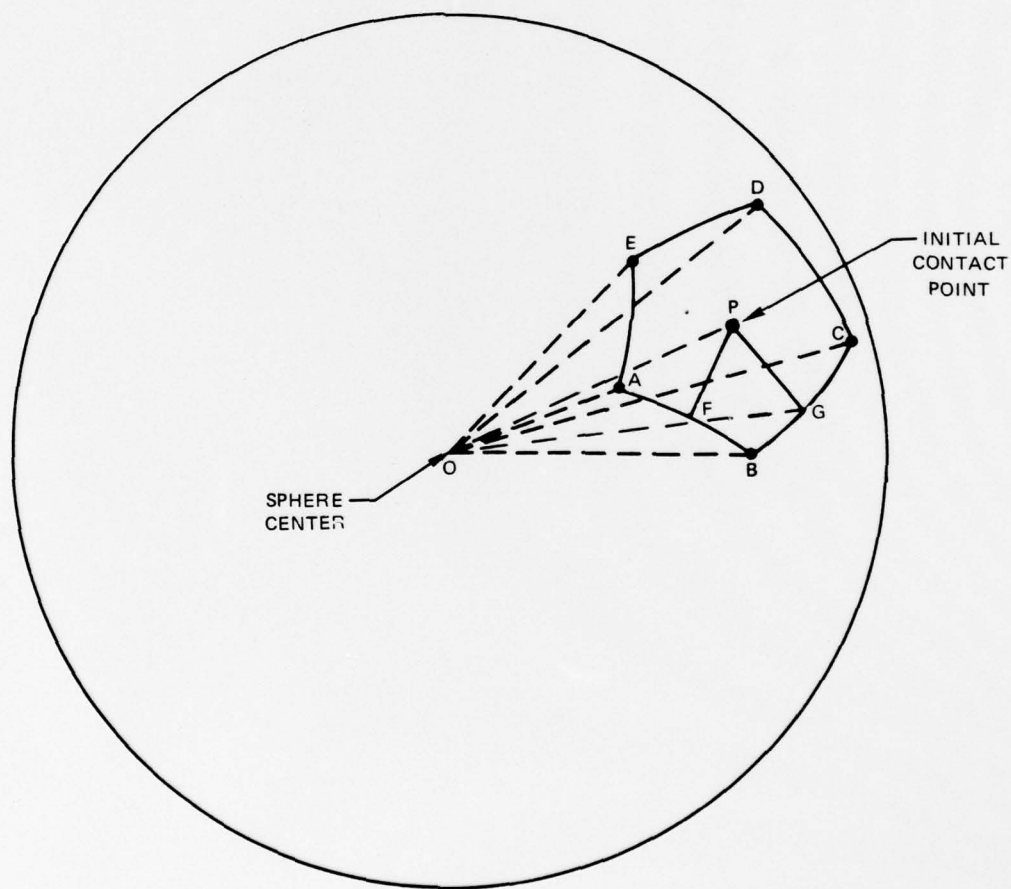


SPHERES 1 - 12 ALL CONTACT THE CENTRAL SPHERE
SPHERES 1 - 6 LIE IN THE PLANE OF THE CENTRAL SPHERE
SPHERES 7 - 9 ARE BELOW THE CENTRAL SPHERE
SPHERES 10 - 12 ARE ABOVE THE CENTRAL SPHERE

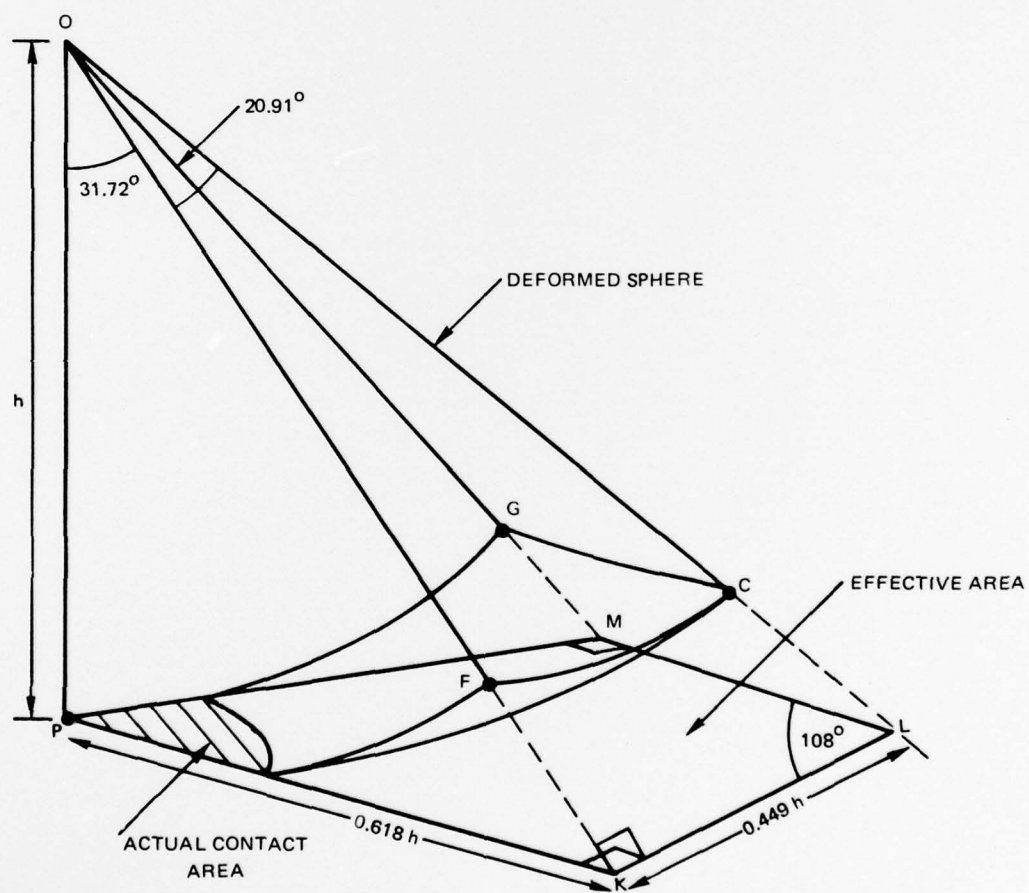
(b) SPHERICAL PARTICLE DEFORMED INTO A REGULAR DODECAHEDRON



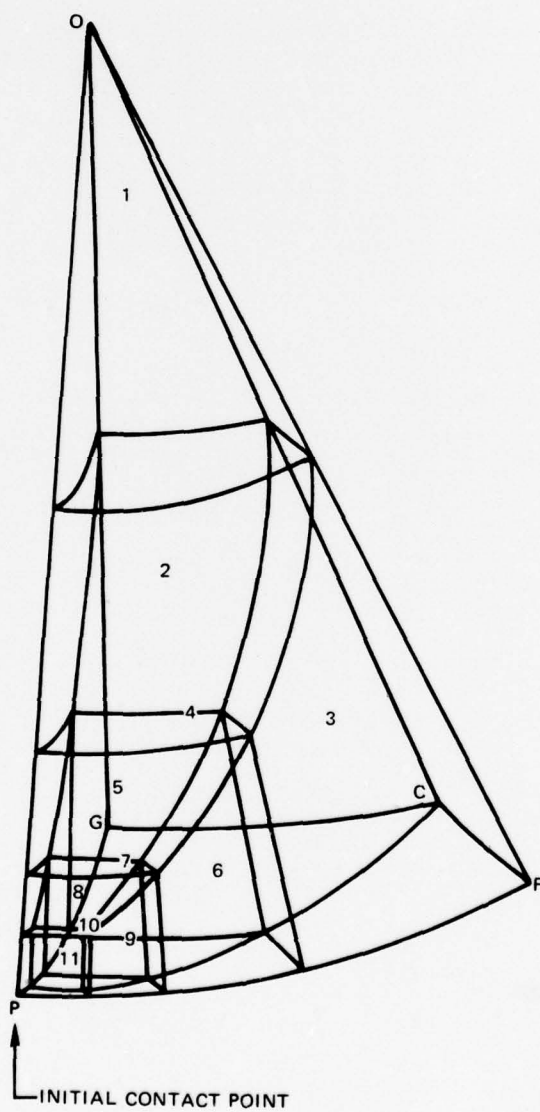
ONE OF TWELVE FIVE-SIDED PYRAMIDS WHICH CONSTITUTE THE UNDEFORMED SPHERE



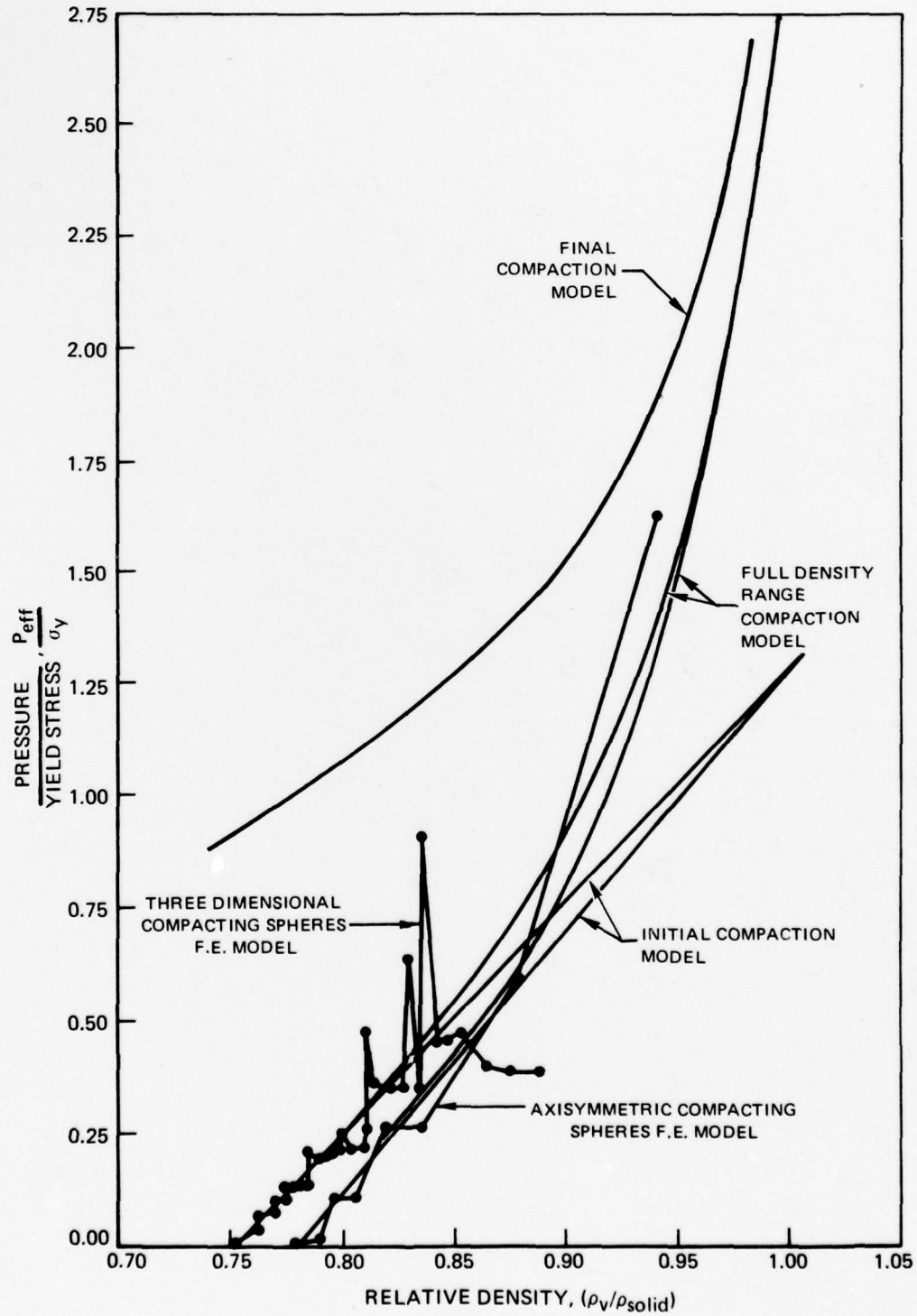
EFFECTIVE AREA USED IN EFFECTIVE APPLIED PRESSURE CALCULATION



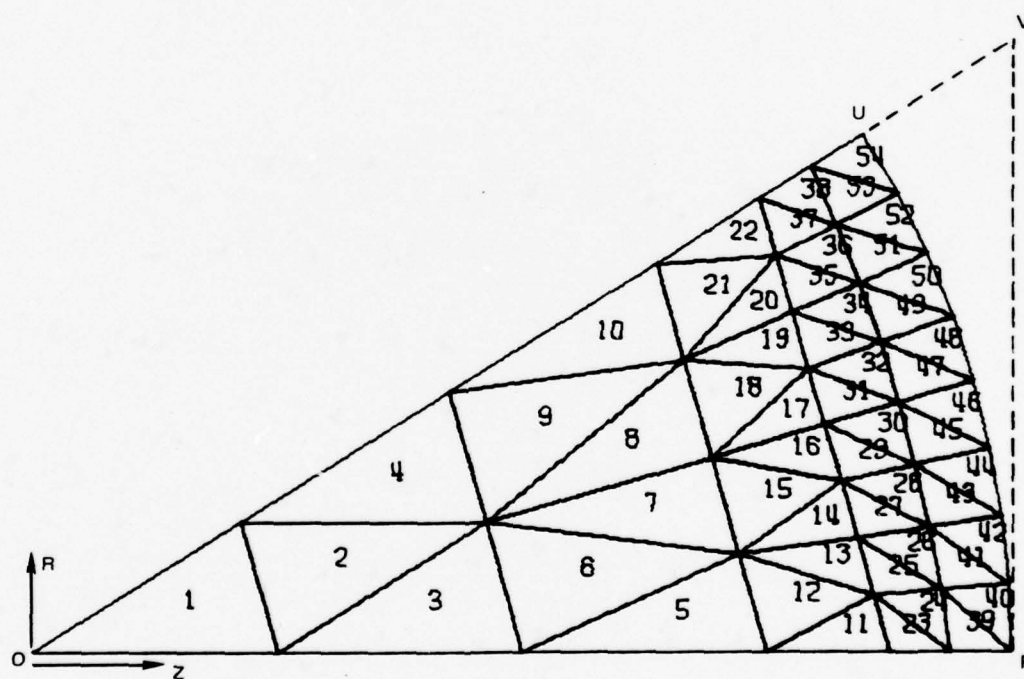
COMPACTING SPHERES FINITE ELEMENT BREAKUP



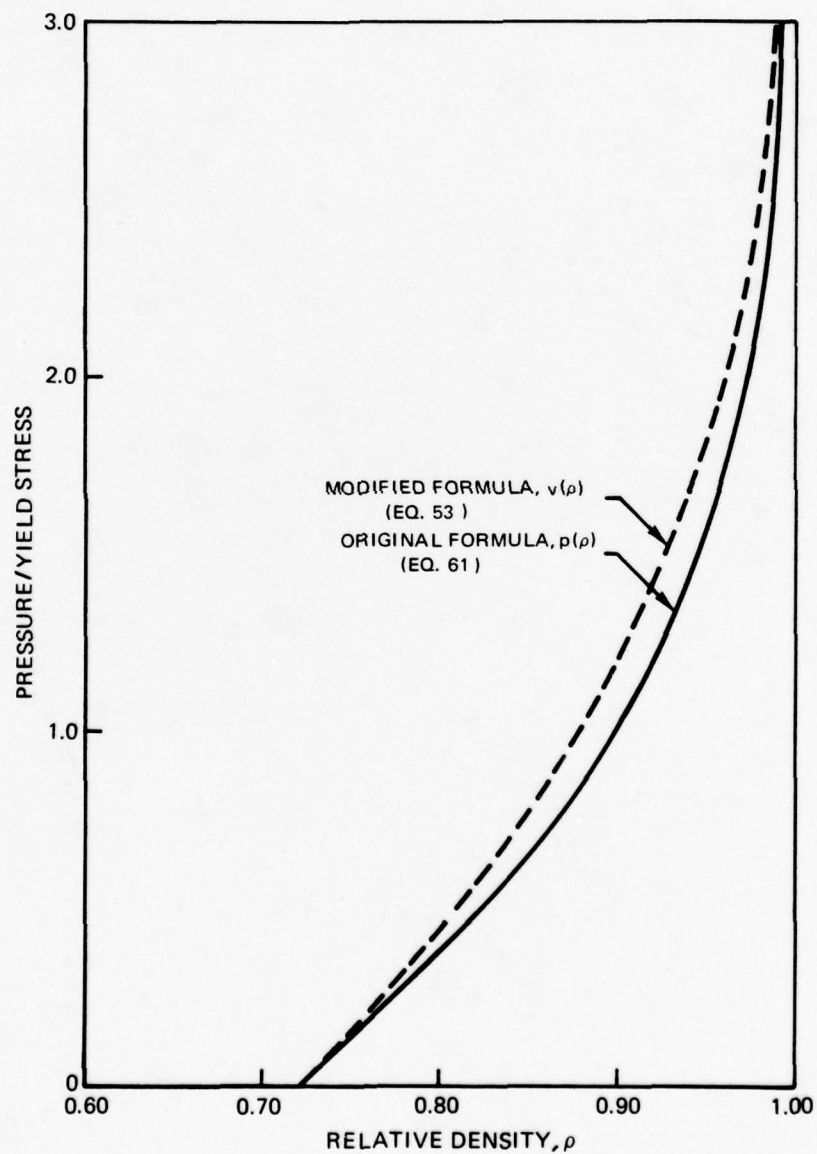
COMPARISON OF POWDER COMPACTION FORMULAE WITH FINITE ELEMENT RESULTS



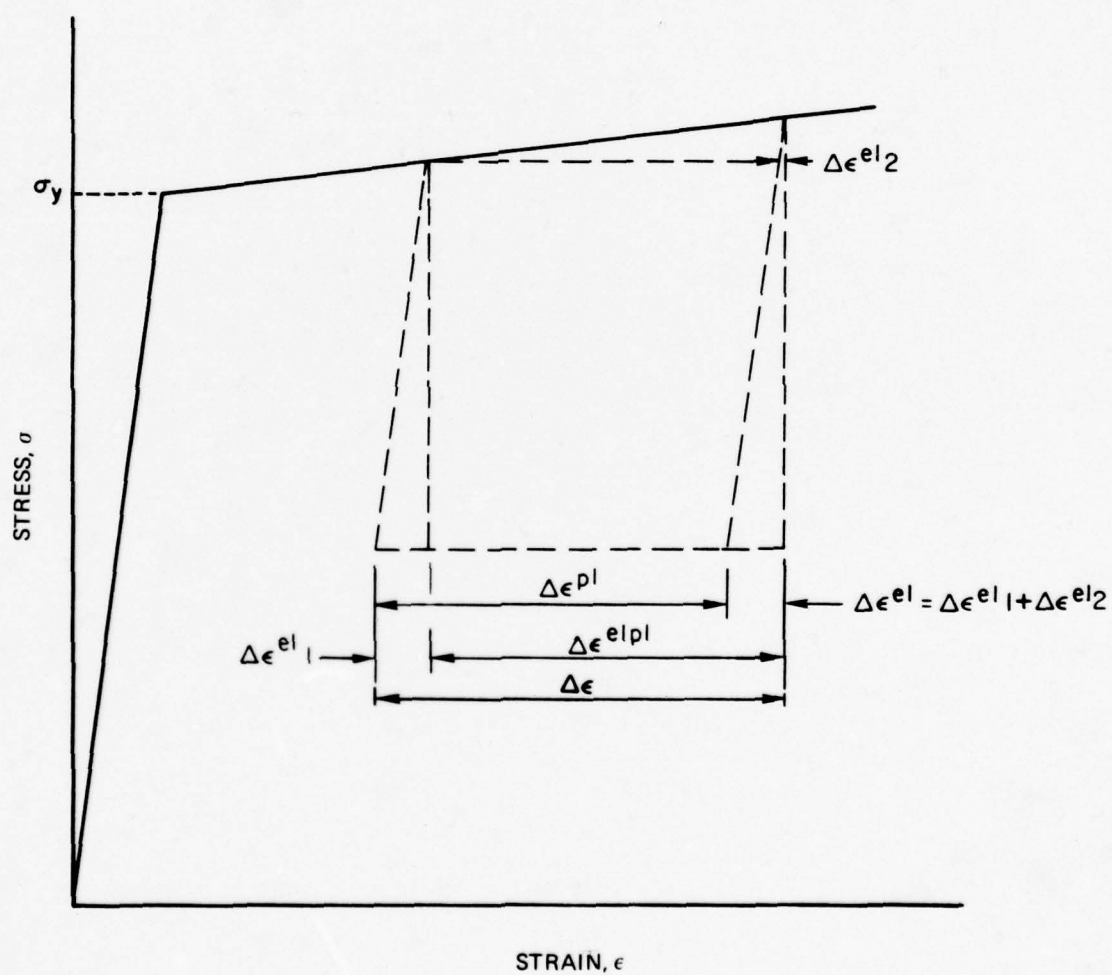
AXISYMMETRIC MODEL OF COMPACTING SPHERE



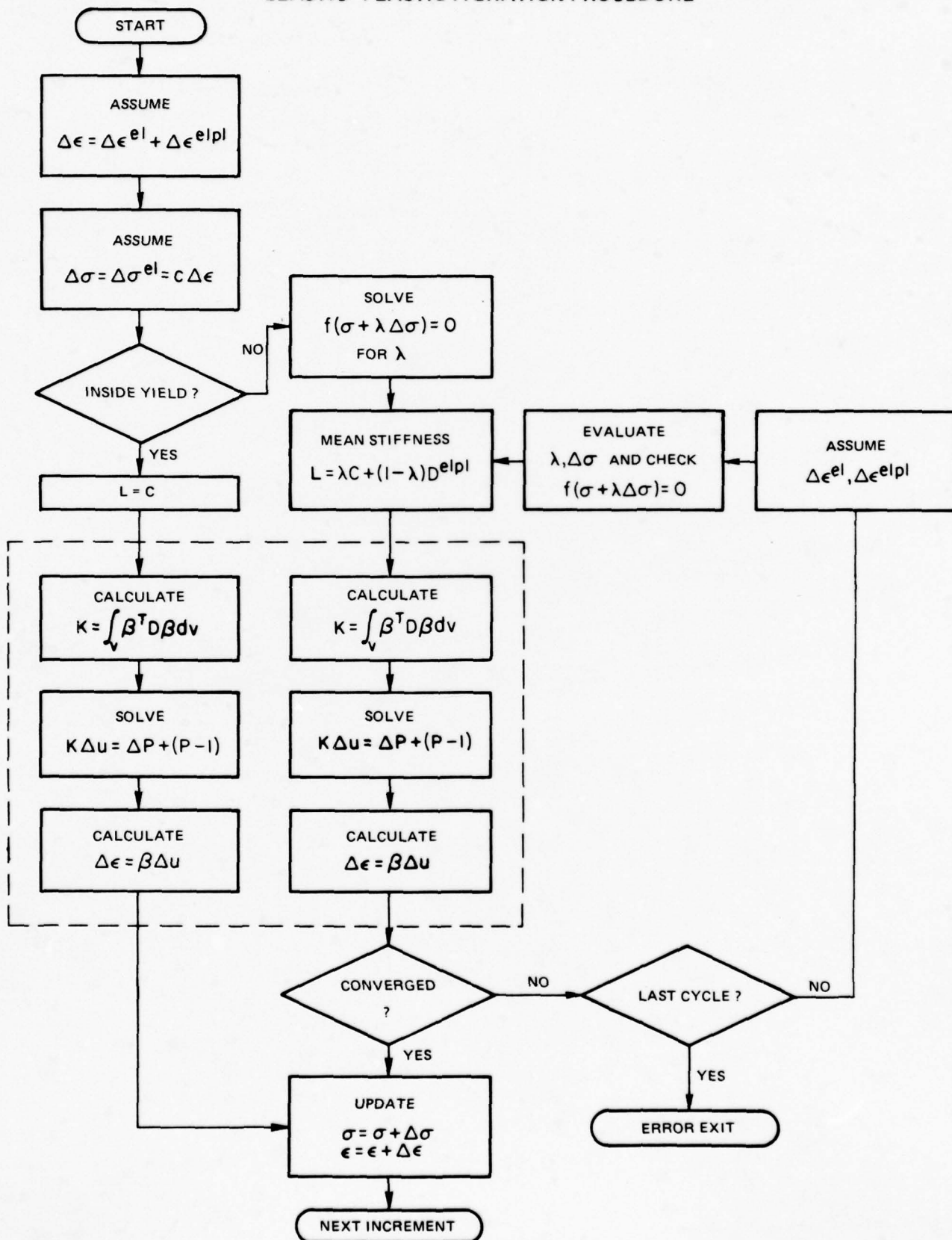
COMPARISON OF RESULTS OF POWDER COMPACTION FORMULAE



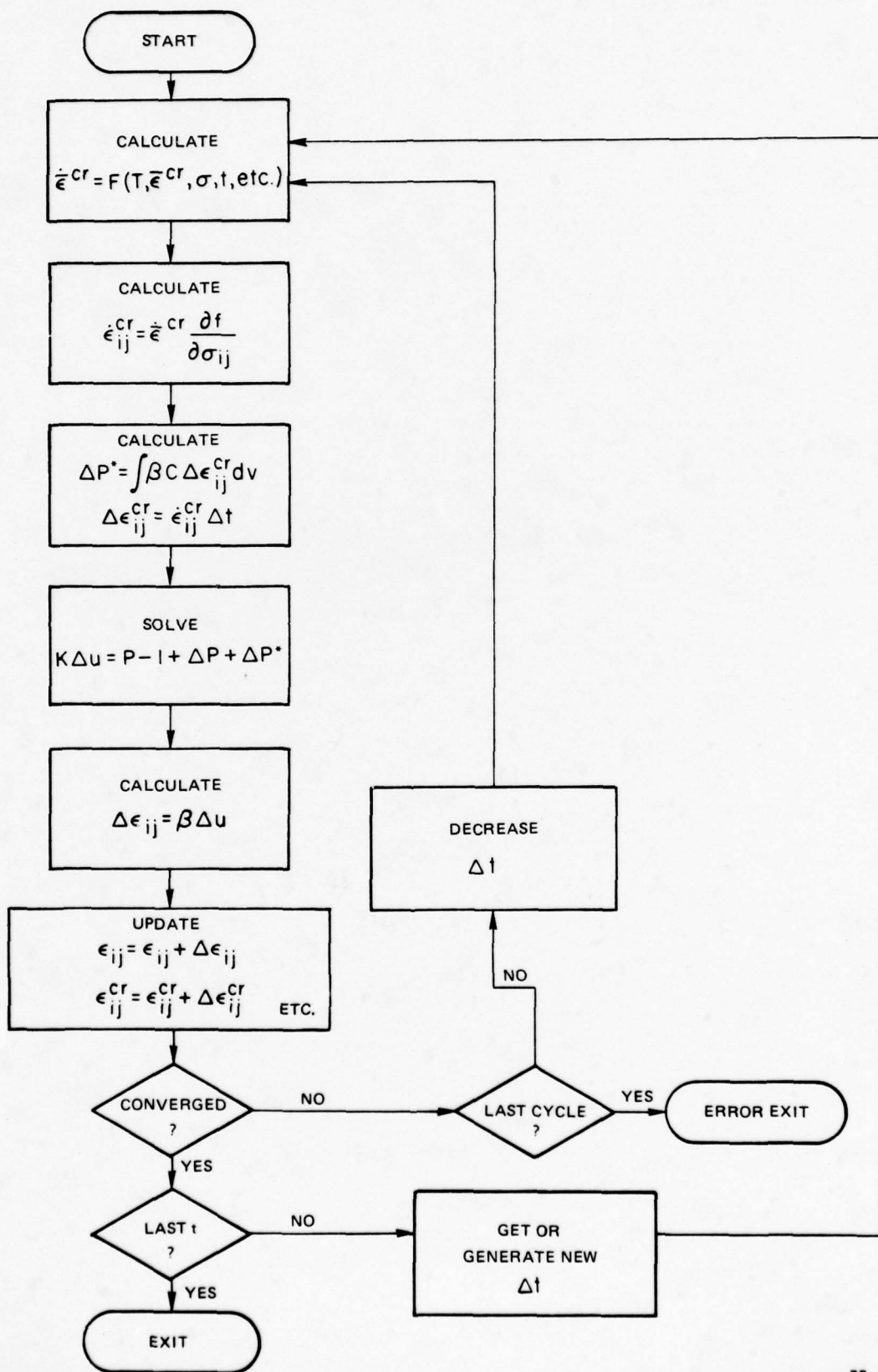
ELASTIC-PLASTIC STRAIN DECOMPOSITIONS
FOR BILINEAR STRESS-STRAIN LAW



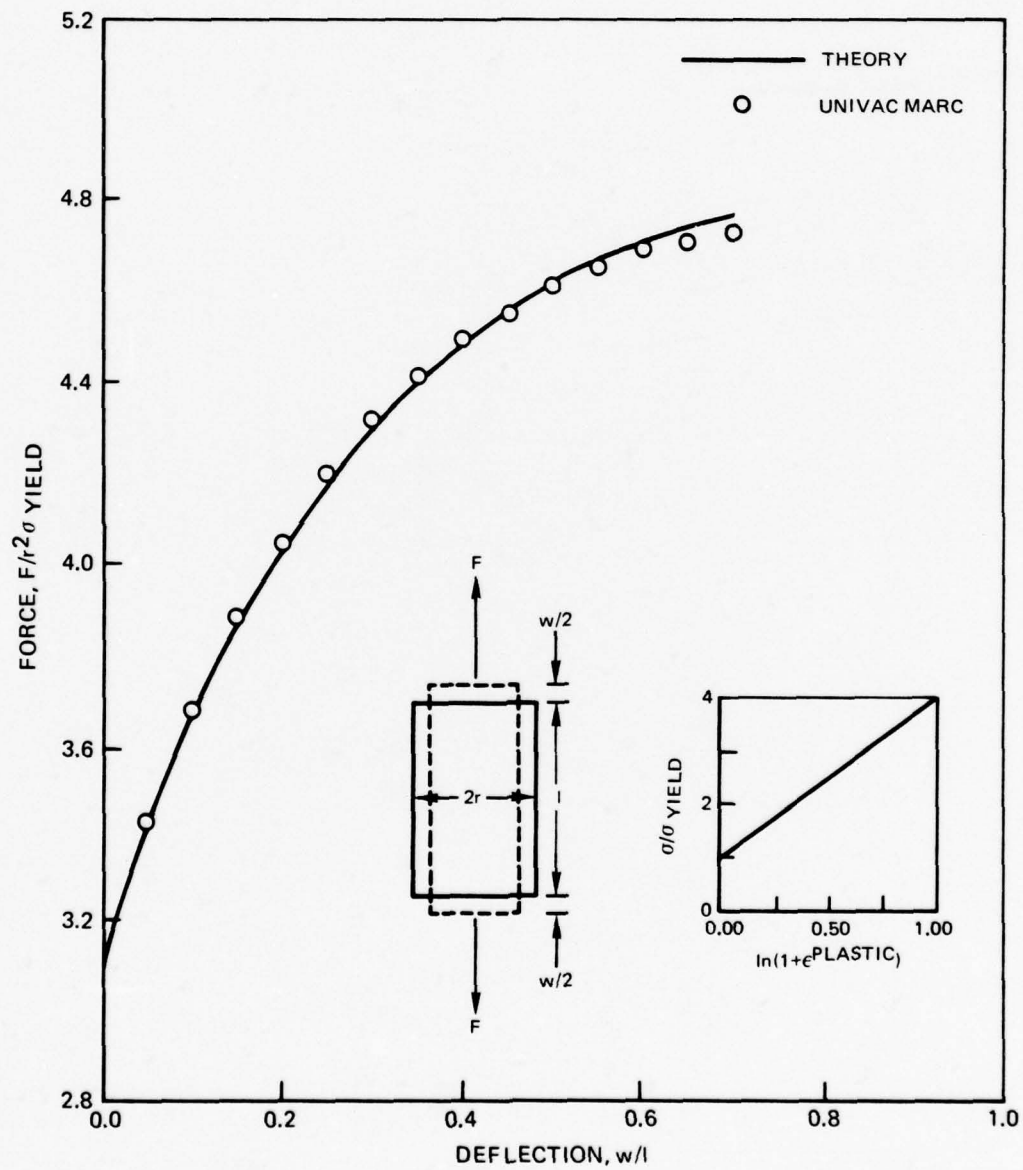
ELASTIC-PLASTIC ITERATION PROCEDURE



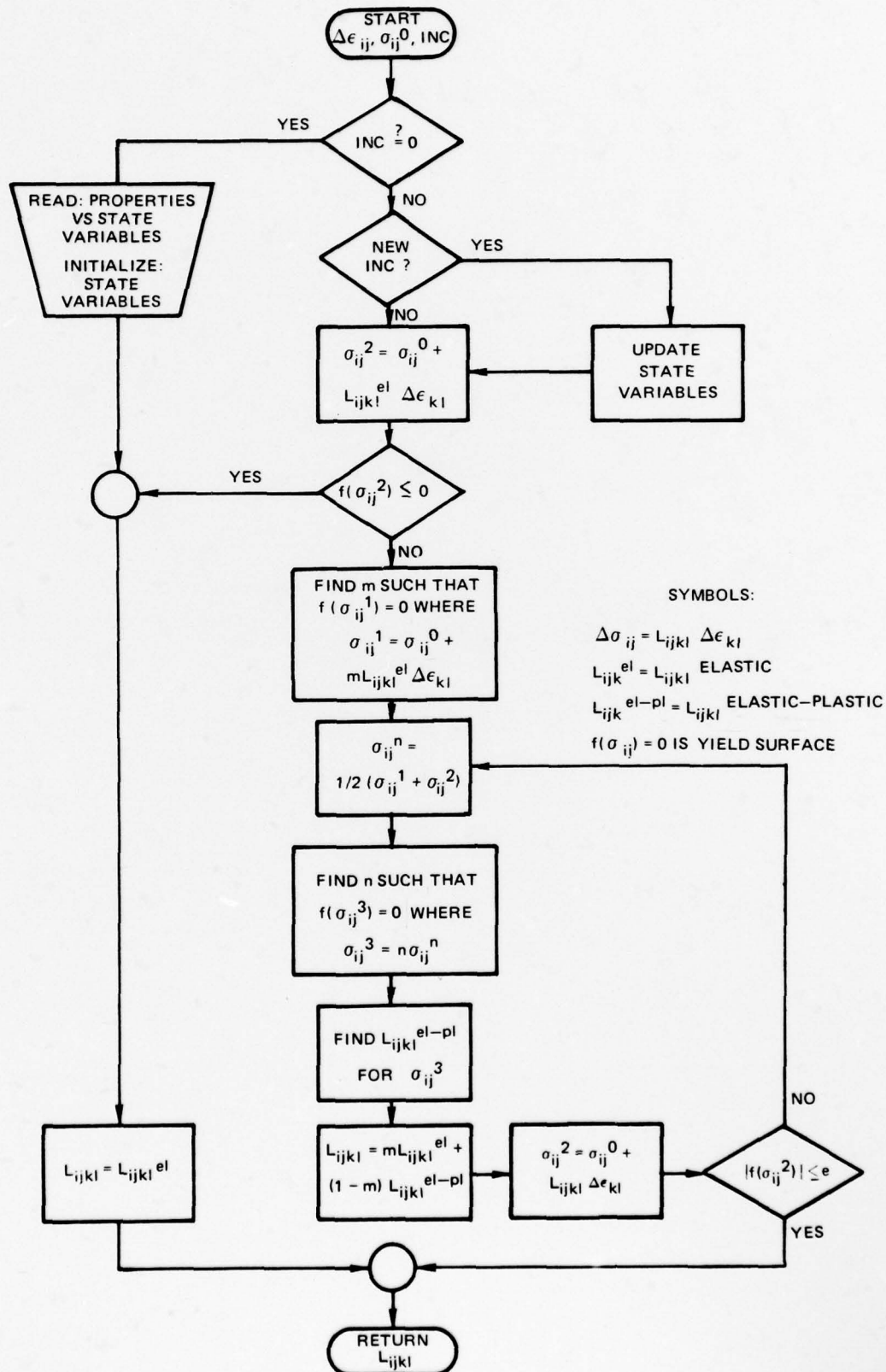
CREEP ITERATION PROCEDURE

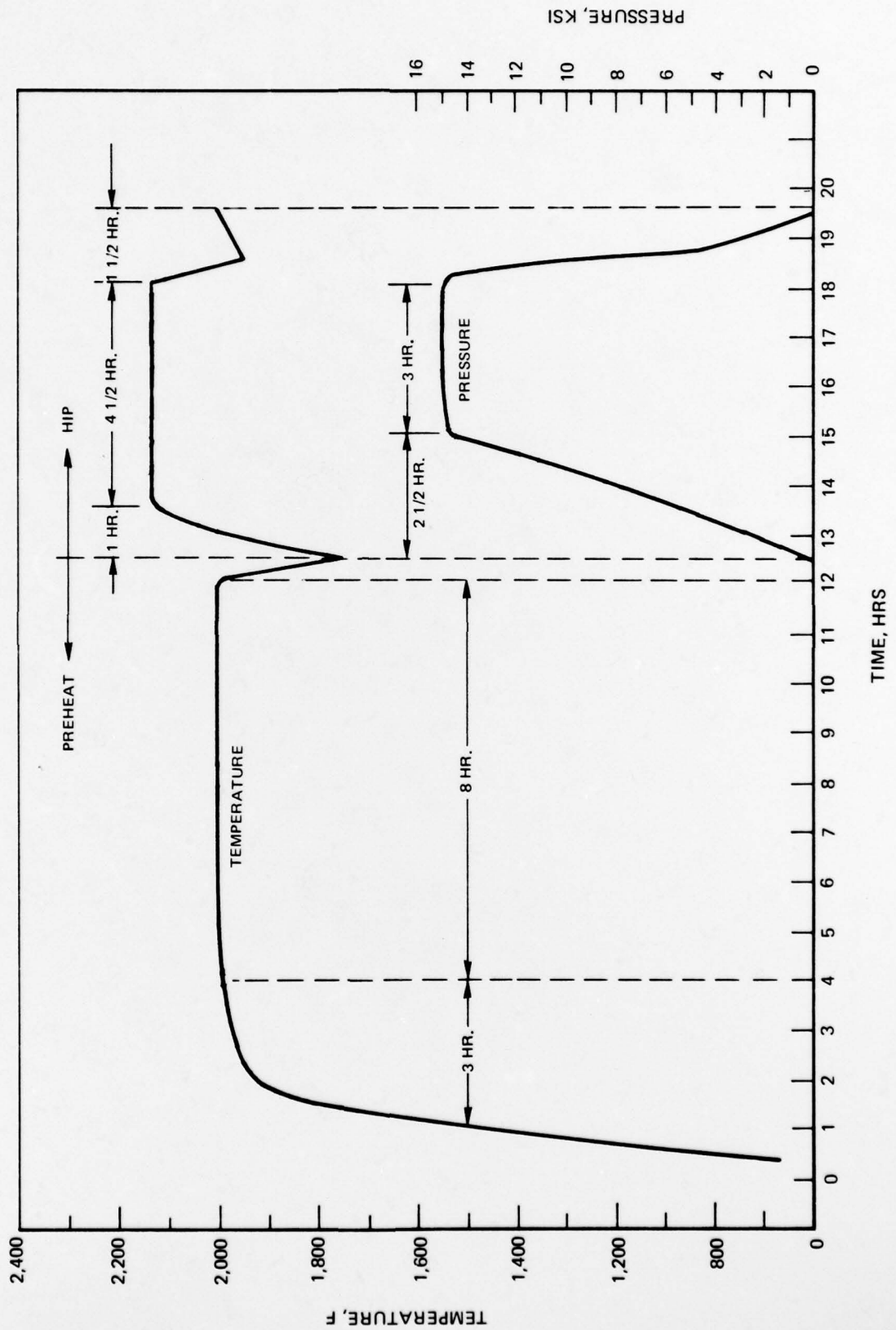


AXISYMMETRIC LARGE STRAIN MARC TEST CASE

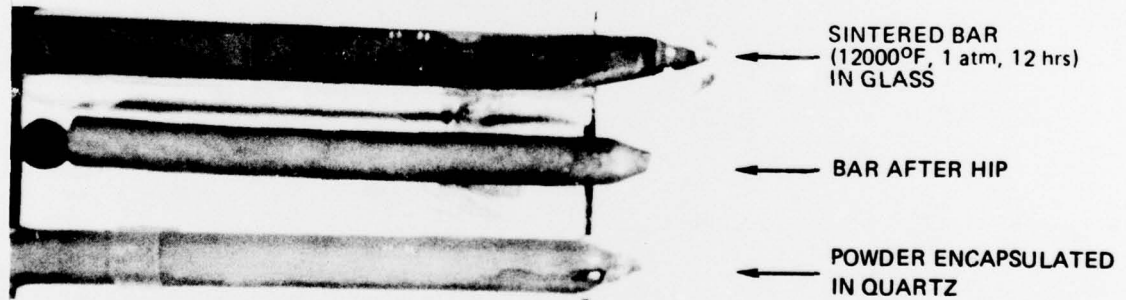


FLOW CHART FOR CALCULATING MATERIAL STIFFNESS MATRIX

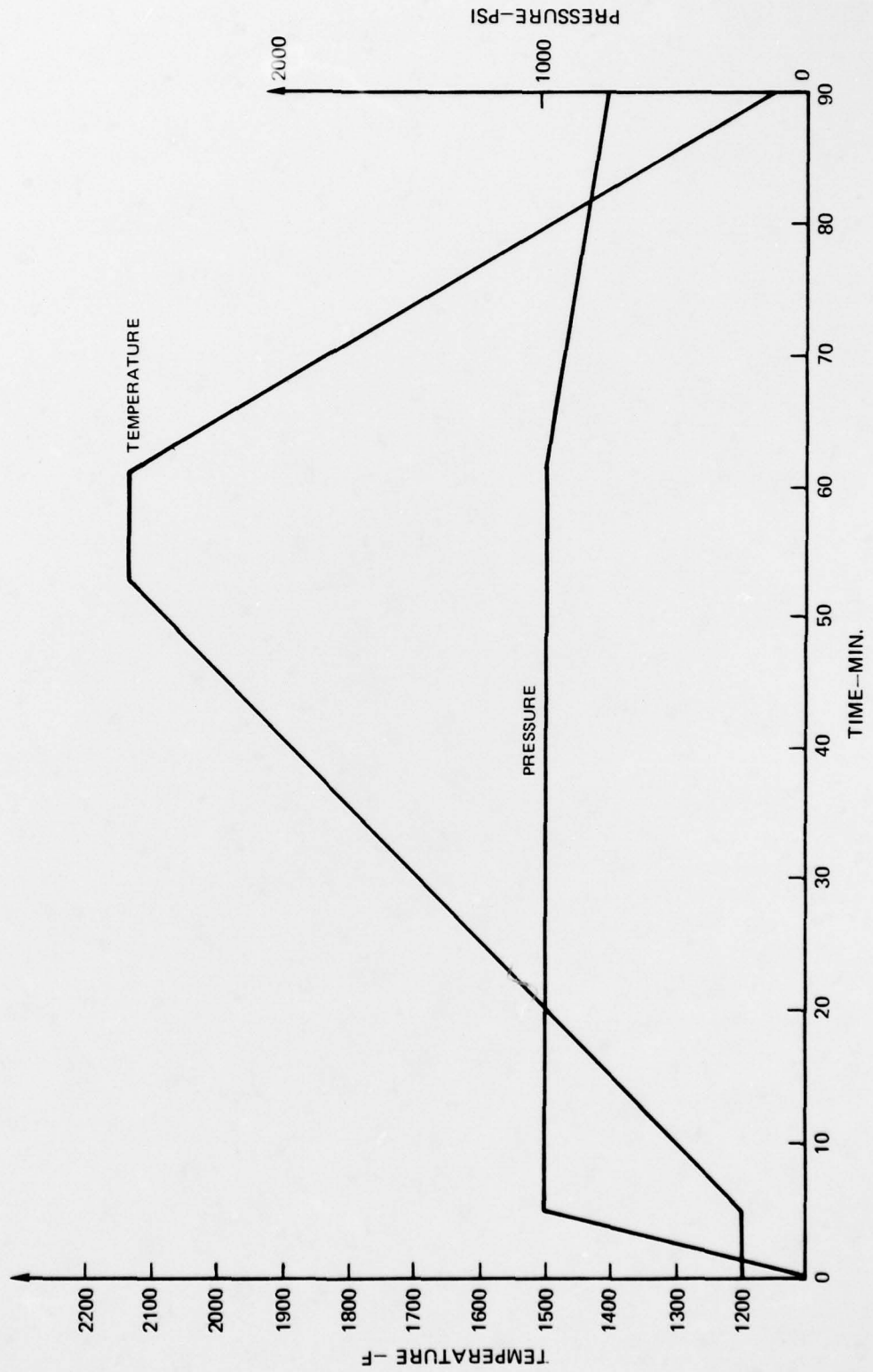


TYPICAL HIP PROCESS
TEMPERATURE-PRESSURE-TIME PROFILE

PARTIAL HIP SPECIMENS AT VARIOUS PROCESSING STAGES



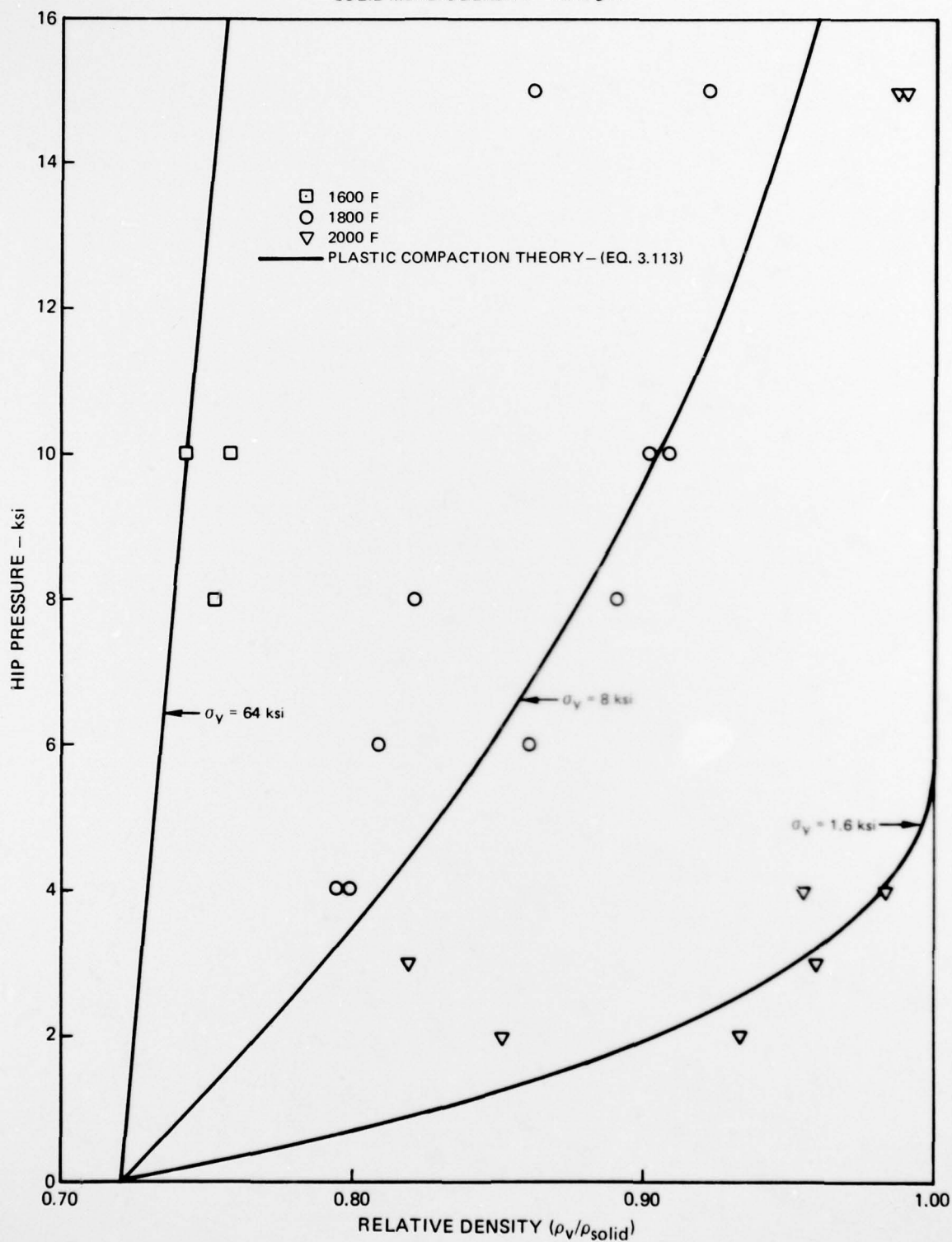
HIP UNIT PRESSURE AND TEMPERATURE CYCLE FOR SPECIMEN 3



FINAL DENSITY OF PARTIAL HIP SAMPLES

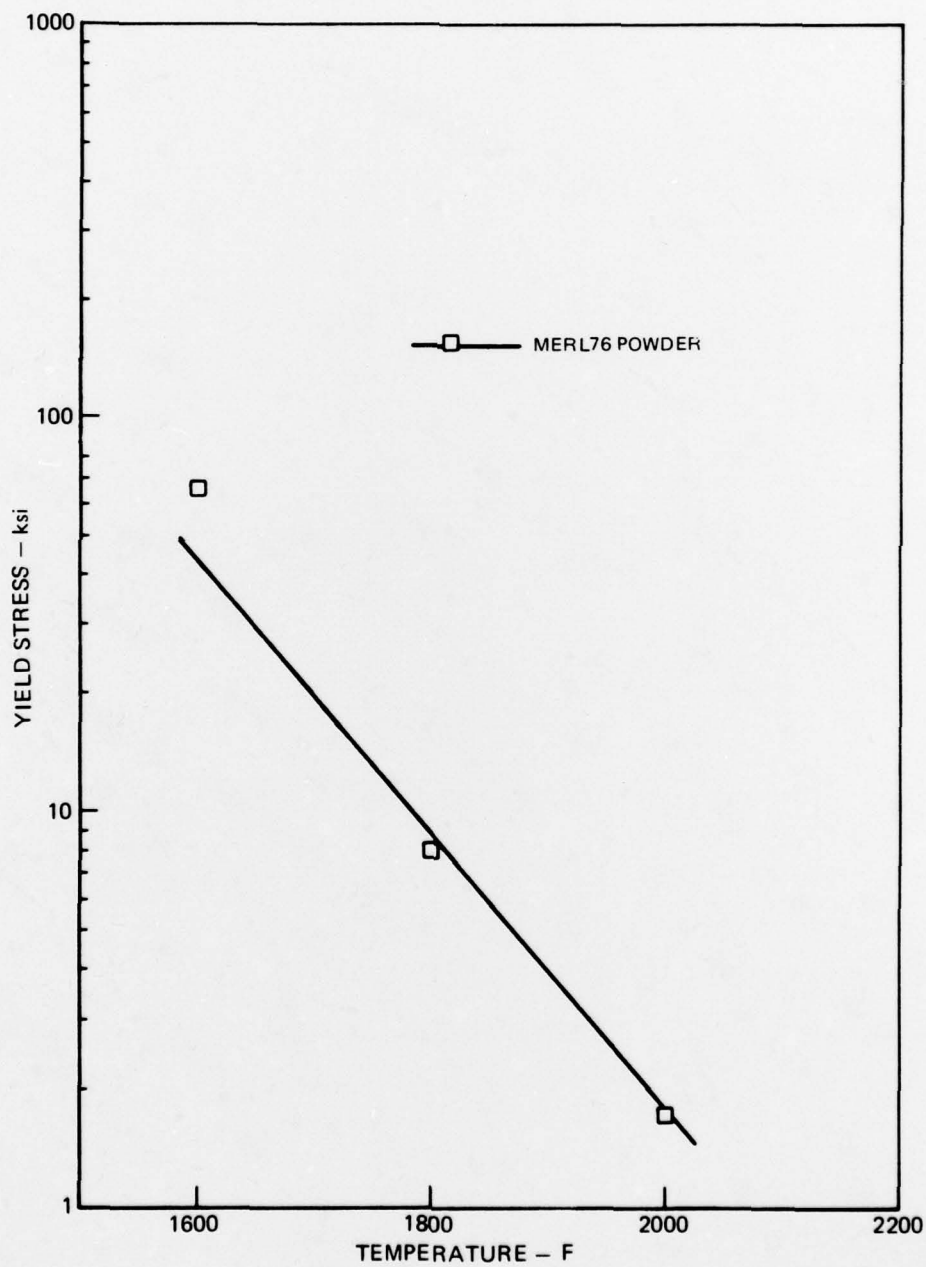
ALL POINTS 10MIN AT MAXIMUM TEMPERATURE AND PRESSURE

SOLID MERL76 DENSITY = 7.945 g/cc

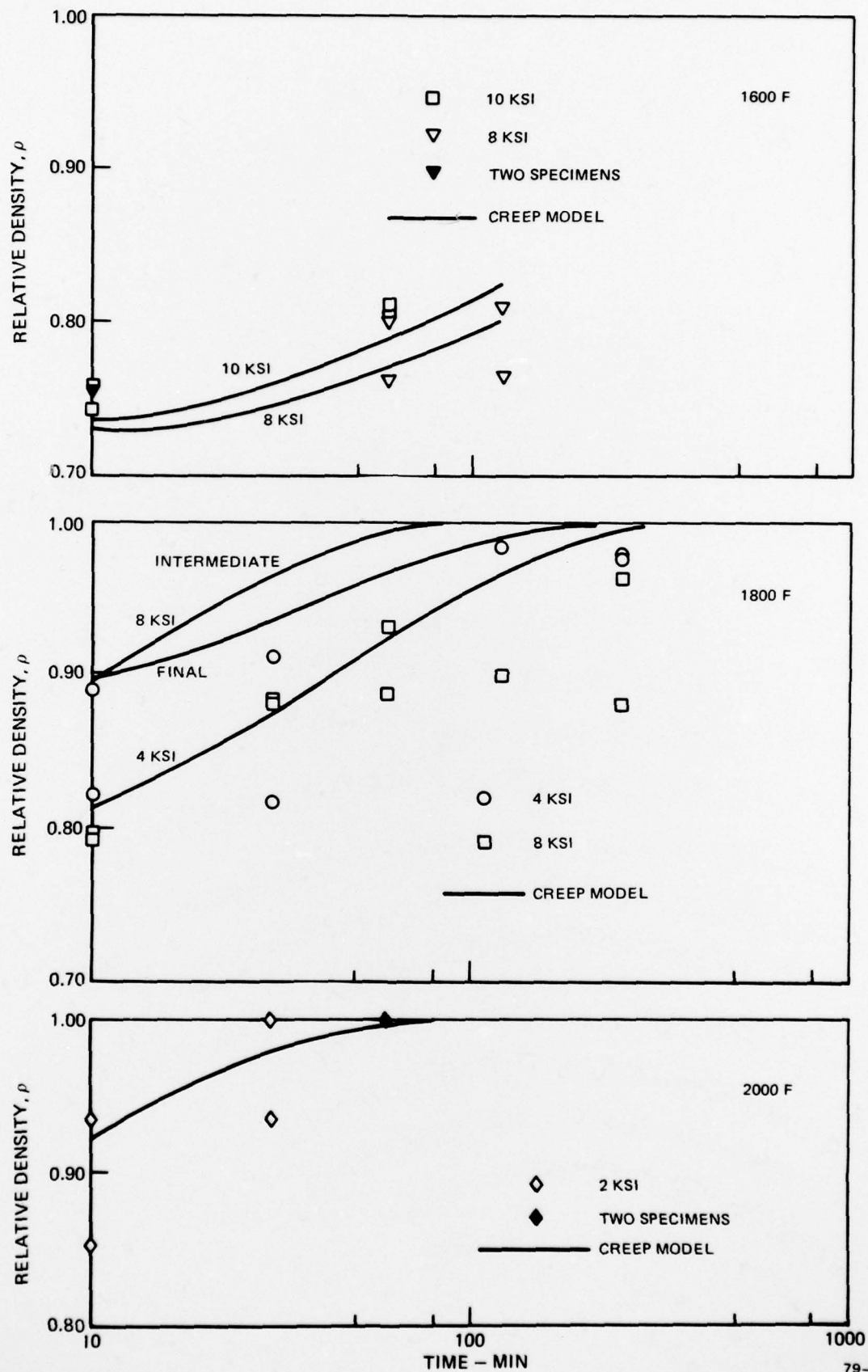


79-05-79-2

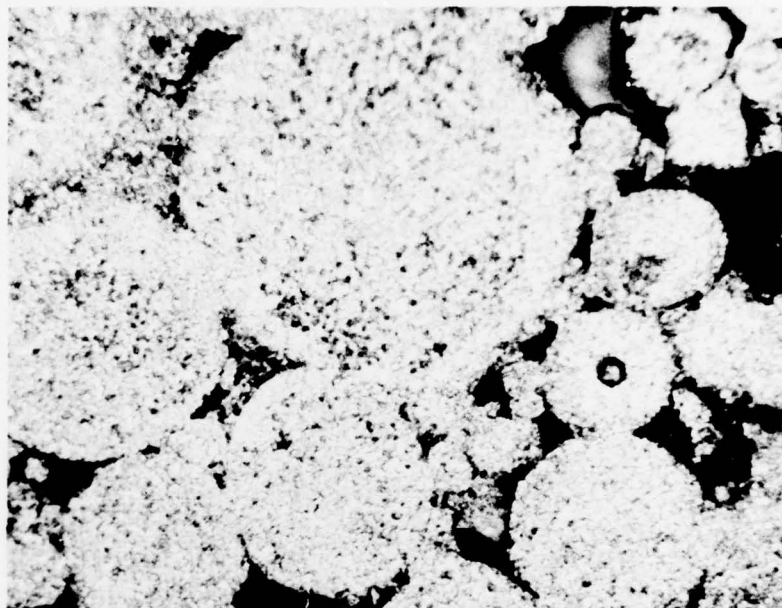
YIELD STRESS FOR MERL76



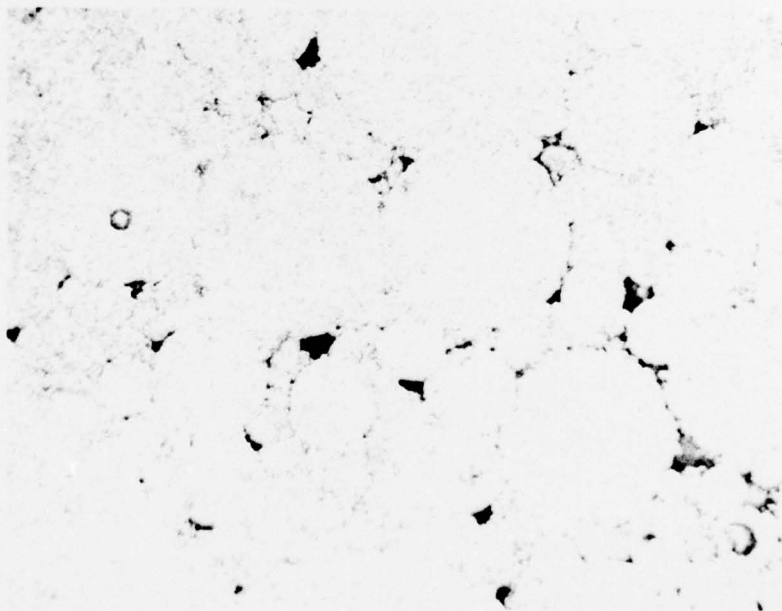
FINAL DENSITY OF PARTIAL HIP SAMPLES



MICROGRAMS OF PARTIALLY COMPACTED MERL76 POWDER

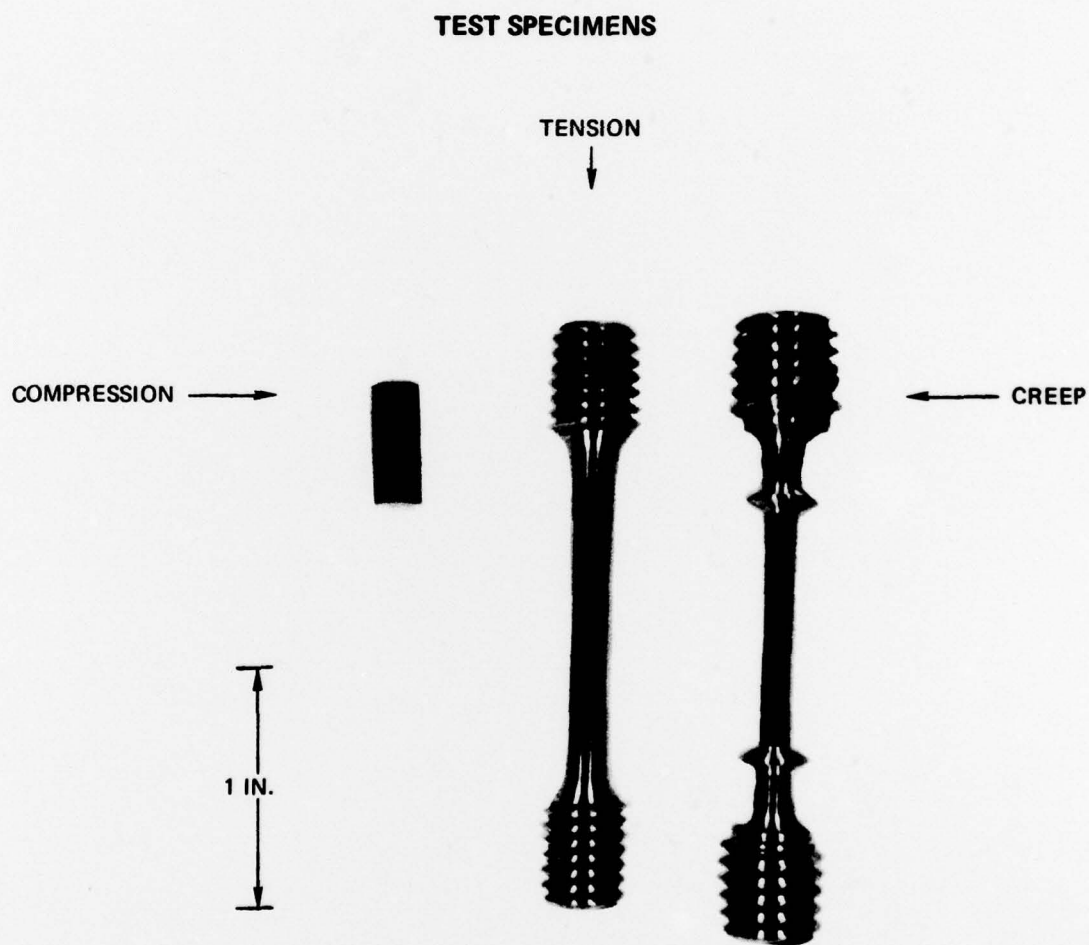


10 MIN. AT 1800°F AND 4 ksi; RELATIVE DENSITY 0.80, 500X



10 MIN. AT 1800°F AND 8 ksi; RELATIVE DENSITY 0.89, 500X

FIG. 29



SAMPLE COMPRESSION TEST DATA
SPECIMEN NO. 1006, 1800 F

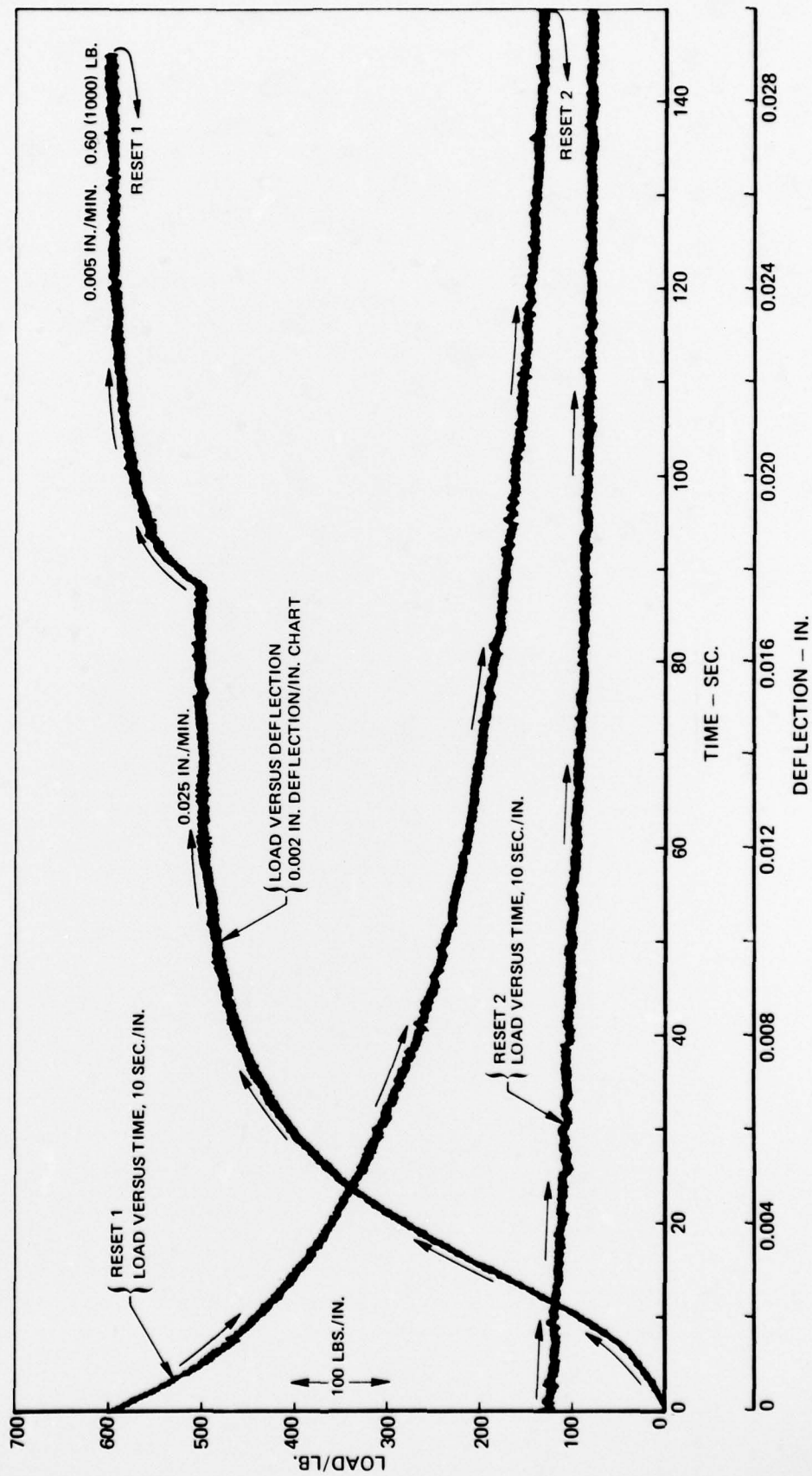
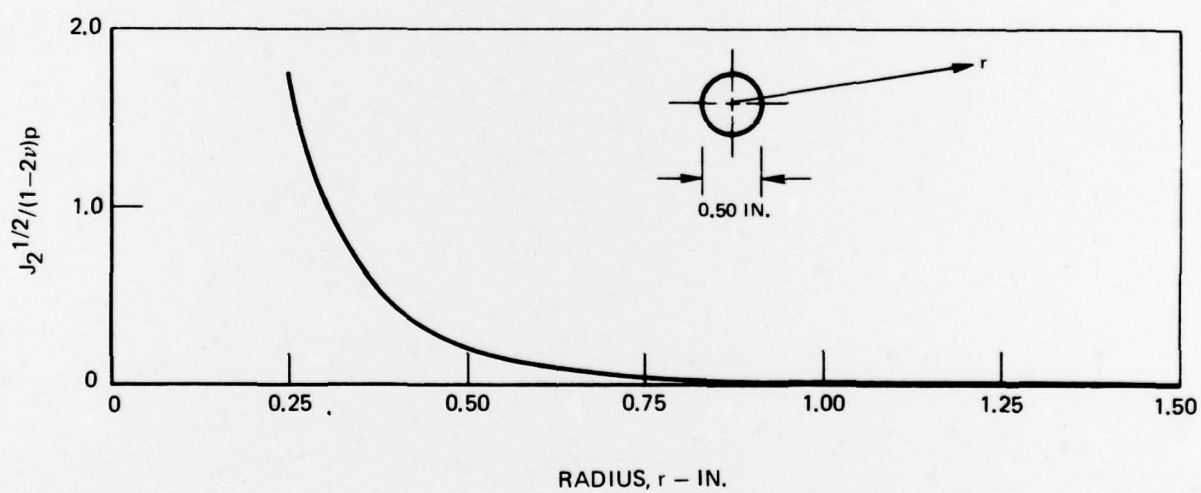
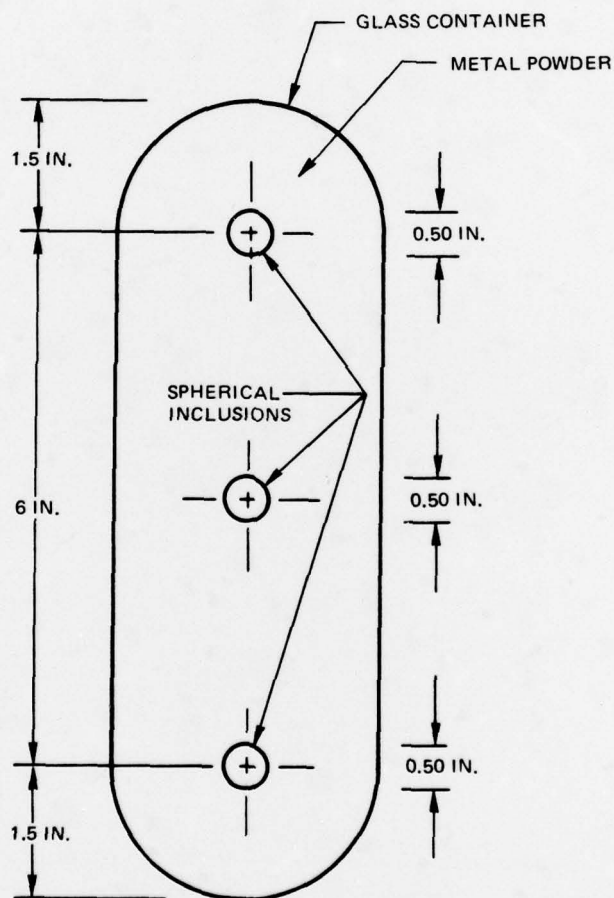


FIG. 30

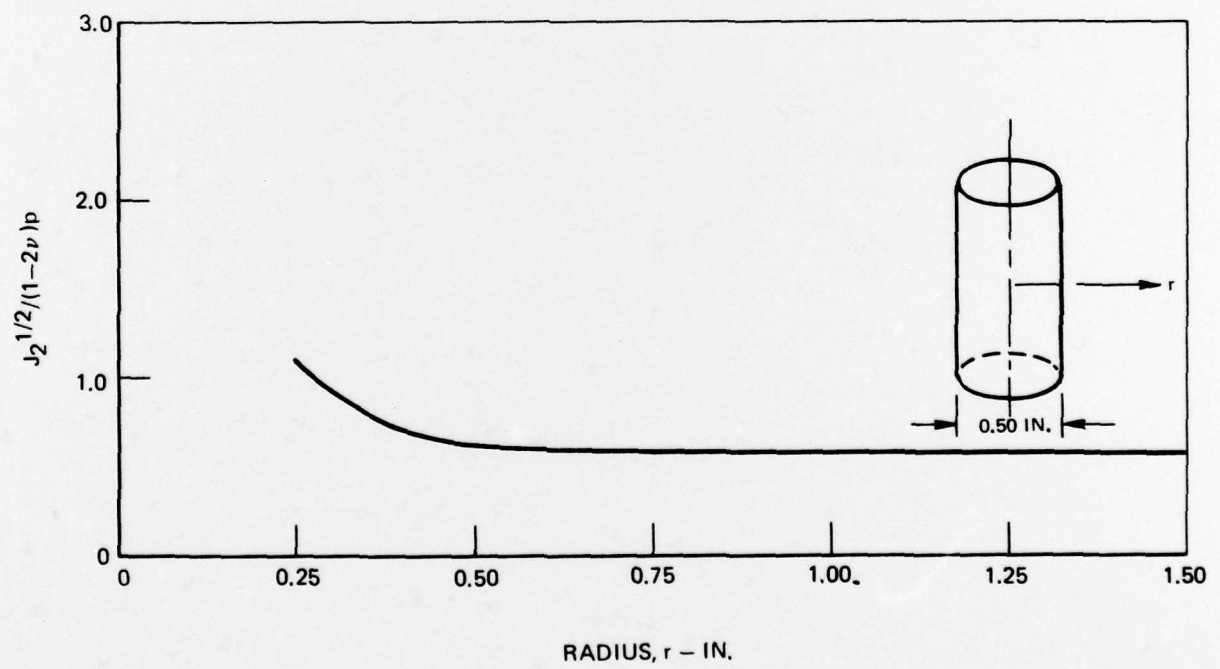
SECOND DEVIATORIC STRESS INVARIANT FOR RIGID SPHERICAL
INCLUSION EMBEDDED IN AN INFINITE ELASTIC SOLID



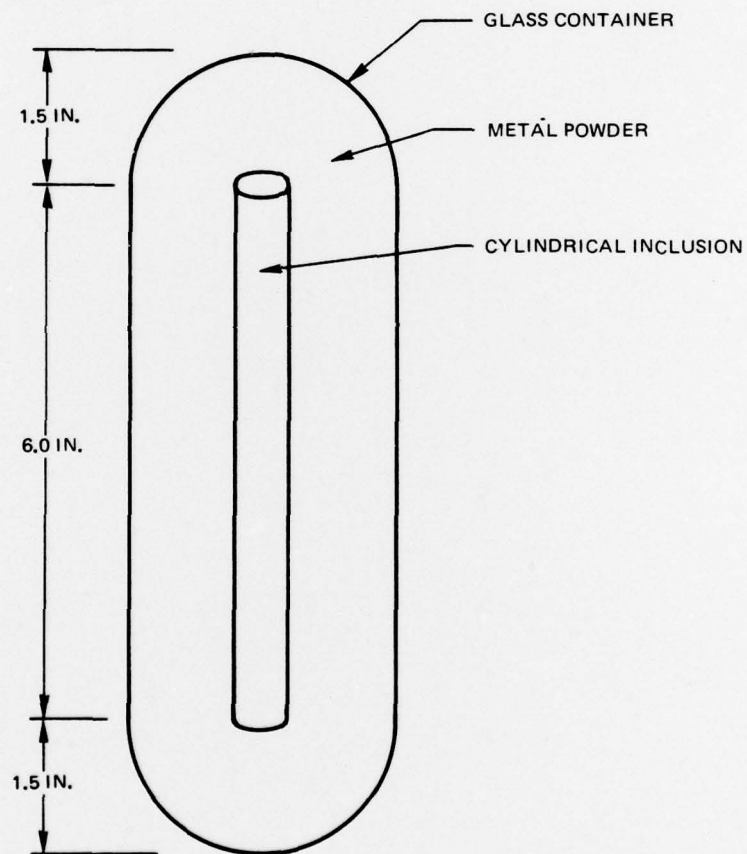
CANDIDATE VALIDATION TEST
CONFIGURATION USING SPHERICAL INCLUSIONS



SECOND DEVIATORIC STRESS INVARIANT FOR RIGID CYLINDRICAL INCLUSION
EMBEDDED IN AN INFINITE ELASTIC SOLID



CANDIDATE VALIDATION TEST CONFIGURATION
USING CYLINDRICAL INCLUSION



LOCATION OF VALIDATION EXPERIMENTS ON YIELD SURFACE

